PRODUCTION OF NANO CaCO₃ IN BENCH SCALE BY SMALL PENETRATION THEORY

A Thesis Submitted to
the Graduate School of Engineering and Sciences of
İzmir Institute of Technology
in Partial Fulfillment of the Requirements for the Degree of

MASTER OF SCIENCE

in Chemical Engineering

by
Görkem TOPRAK

July 2013
İZMİR

We approve the thesis of **Görkem TOPRAK**

Examining Committee Members:

_____
Assoc. Prof.Dr. Ekrem ÖZDEMİR
Department of Chemical Engineering, İzmir Institute of Technology

_____
Prof.Dr. Fehime ÖZKAN
Department of Chemical Engineering, İzmir Institute of Technology

_____
Prof.Dr. Hürriyet POLAT
Department of Chemistry, İzmir Institute of Technology

1 July 2013

_____
Assoc. Prof.Dr. Ekrem ÖZDEMİR
Supervisor, Department of Chemical Engineering, İzmir Institute of Technology

_____   _____
Prof.Dr. Fehime ÖZKAN   **Prof.Dr. R. Tuğrul SENGER**
Head of the Department of   Dean of the Graduate School of
Chemical Engineering   Engineering and Sciences

ACKNOWLEDGMENTS

.

ABSTRACT

PRODUCTION OF NANO CaCO$_3$ IN BENCH SCALE BY SMALL PENETRATION THEORY

Calcium carbonate (CaCO$_3$) has been used as filling material in various industries such as paint, paper, and polymeric materials. Using filling materials will enhance some of the physical properties of the composite material and decrease the product costs. Especially, the physical properties of the composite materials were enhanced significantly when the CaCO$_3$ is used in nano sizes. CaCO$_3$ can be produced from natural sources by crushing, grinding, and sieving processes, however, calcite obtained from the natural sources are usually in micron sizes and they are not in the desired quality and purity. Here, it was proposed that the dissolution rate of CO$_2$ is the limiting step in CaCO$_3$ crystallization and a small penetration method was developed for the limited dissolution of CO$_2$ in the Ca(OH)$_2$ solution. When Ca(OH)$_2$ was added into the 10 mM CaCO$_3$, zeta potential values of CaCO$_3$ particles were increased from negative to positive value indicating that CaCO$_3$ particles were stabilized in the presence of Ca(OH)$_2$ solution. Rice-like CaCO$_3$ particles were synthesized at the very early stage of crystallization. When crystallization progresses, the high energetic end sites started to dissolve, and the dissolution was progressed through the inside of the particles resulting in hollow calcite particles. BET surface area of hollow calcite particles was found to be 14.75 m^2/g. Different parameters such as Ca(OH)$_2$ flow rate, CO$_2$ flow rate, Ca(OH)$_2$ concentration, pipe diameter etc. were studied. Calcite particles in nano sizes, homogeneous size distribution, hollow shapes, and different morphologies were achieved to be produced.

ÖZET

KISA PENETRASYON YÖNTEMİYLE KÜÇÜK ÖLÇEKTE NANO CaCO$_3$ ÜRETİMİ

Kalsiyum karbonat (CaCO$_3$), boya, kağıt ve polimerik malzemeler gibi çeşitli sanayi dallarında dolgu malzemesi olarak kullanılmaktadır. Dolgu malzemesinin kullanması, kompozit malzemenin bazı fiziksel özelliklerini iyileştirmekte ve ürün maliyetini düşürmektedir. Bilhassa, CaCO$_3$ nano boyutlarda kullanıldığında kompozit malzemelerin fiziksel özellikleri önemli ölçüde iyileştirmektedir. CaCO$_3$ doğal kaynaklardan kırma, öğütme ve eleme yöntemi ile elde edilebilir, fakat, doğal kaynaklardan elde edilen CaCO$_3$ genellikle mikron boyutlarda ve istenilen kalite ve saflıkta değildir. Burada, CO$_2$ çözünme oranının CaCO$_3$ kristalizasyonunda sınırlayıcı basamak olduğu ve Ca(OH)$_2$ çözeltisinde CO$_2$'in sınırlı oranda çözünmesi için kısa penetrasyon yöntemi geliştirilmiştir. Ca(OH)$_2$, 10 mM CaCO$_3$ içerisine ilave edildiğinde CaCO$_3$ parçacıklarının zeta potansiyel değeri negatiften pozitif değerlere yükselmiştir. Buradan CaCO$_3$ parçacıklarının Ca(OH)$_2$ içerisinde stabil oldukları anlaşılmaktadır. Kristalizasyonun ilk aşamasında pirinç tanesi şeklinde CaCO$_3$ parçacıkları sentezlenmiştir. Kristalleşme ilerlediğinde, taneciklerin yüksek enerjili uç kısımları çözünmeye başlamış ve çözünme, taneciklerin içine doğru işleyerek içi boş kalsit tanecikleri üretilmiştir. İçi boş kalsit taneciklerin BET yüzey alanı 14.75 m^2/g olarak bulunmuştur. Ca(OH)$_2$ çözeltisi akış hızı, CO$_2$ gaz akış hızı, Ca(OH)$_2$ konsantrasyonu, boru çapı gibi farklı parametreler çalışılmıştır. Nano boyutlarda, homojen boyut dağılımında, içi boş yapıda, farklı morfolojilerde kalsit taneciklerinin üretimi başarılmıştır.

TABLE OF CONTENTS

LIST OF FIGURES

LIST OF TABLES

CHAPTER 1

INTRODUCTION

Calcium carbonate ($CaCO_3$) is an inorganic compound that has been widely used as filling material in plastics, paint, textile, electronics, optics, ceramics, metallurgy, paper, pharmaceutics, ink and so on. (Campos, Ribeiro, & Cardoso, 2007; Carmona, Morales, Sainz, & Clemente, 2003c; Jung, Kang, Kim, & Choi, 2000; Lam, Hoang, Quang, & Kim, 2009; Matahwa, Ramiah, & Sanderson, 2008; Sheng et al., 2006a; Sondi, Škapin, & Salopek-Sondi, 2008; Ukrainczyk, Kontrec, Babic-Ivancic, Brecevic, & Kralj, 2007). More than 80% of the fillers used in thermoplastics are $CaCO_3$ (Sahebian, Zebarjad, Khaki, & Sajjadi, 2009). Using filling materials significantly reduce the product cost and, in most cases, improve some of the physical properties of the composite materials.

The annual production for $CaCO_3$ was reported as 56 million tons in 2004 and it expanded to 72 million tons in 2007 with an average annual growth rate of nearly 9%. World demand for $CaCO_3$ was predicted to reach up to 128.6 million tons in 2017 with an annual growth rate of 4% (Roskill Information Services, 2008). Chine is the leading country for the production of $CaCO_3$. Production of $CaCO_3$ in China has grown from 5.2 million tons in 2002 to 11.9 million tons in 2007 (Roskill Information Services, 2008). Turkey has 40% of world's $CaCO_3$ reserves. It was reported that, the total reserves are about 5 billion m^3. Afyon, Bilecik, Burdur, Denizli, Elazığ, Muğla, Balıkesir, Diyarbakır and Eskişehir have the major reserves for $CaCO_3$ (Uyanık, 2010). Although Turkey has significant amount of world $CaCO_3$ reserves, the production capacity for specialized $CaCO_3$ in Turkey is very limited.

$CaCO_3$ has polymorphs such as hydrated and anhydrous. The hydrate polymorphs are $CaCO_3$ monohydrate, $CaCO_3$ hexahydrate, amorphous $CaCO_3$ (Carmona, Morales, & Clemente, 2003a; Gunasekaran & Anbalagan, 2008; Jung et al., 2000; Montes-Hernandez, Fernández-Martínez, Charlet, Tisserand, & Renard, 2008; Ukrainczyk et al., 2007; Xu, Ma, & Colfen, 2007). The anhydrous polymorphs are calcite vaterite, and aragonite (Carmona et al., 2003c; Domingo, Loste, Gómez-Morales, García-Carmona, & Fraile, 2006; Y. S. Han, Hadiko, Fuji, & Takahashi,

2006a; Kabasci, Althaus, & Weinspach, 1996; Montes-Hernandez et al., 2008; Ogino, Suzuki, & Sawada, 1987, 1990; Osman, Atallah, & Suter, 2004; Spanos & Koutsoukos, 1998). Calcite is the most thermodynamically stable form of $CaCO_3$ under standard conditions (Stepkowska, Perez-Rodriguez, Sayagues, & Martinez-Blanes, 2003). Aragonite and vaterite are metastable polymorphs, but they can transform into the stable calcite (Montes-Hernandez et al., 2008). In addition, calcite appears in variety of morphologies such as rhombohedral, scalenohedral, spheroidal, etc. In industry, calcite is the mostly used polymorph. For example, rhombohedral calcite having high specific surface area is used in plastic and sealants industry and scalenohedral calcite is employed in paper and paints industry (Ukrainczyk et al., 2007).

Calcite has been used as filling material in polymeric composite materials. Using calcite as filling material may modify some of the physical and mechanical properties of the composite material and reduce the product cost. For instance, as shown in Figure 1.1, the tensile yield strength of polypropylene (PP)/$CaCO_3$ composite material was decreased as the particle volume fraction was increased (Fu, Feng, Lauke, & Mai, 2008).

The particle sizes varied from 0.01 to 58.0 μm. Since smaller particles have a higher total surface for a given particle loading, it could clearly be stated that the decrease in the tensile yield strength was lower for the smaller particle. Such effect was more pronounced when the particle size was smaller. The strength increased through a more efficient stress transfer mechanism as the surface area of the filler particles was increased. Especially, the decrease in the tensile yield strength was none or slightly increases for 10 nm calcite particles (Pukanszky & Fekete, 1998). Therefore, our objectives are to synthesize $CaCO_3$ in nano sizes, homogeneous size distribution, and different morphologies.
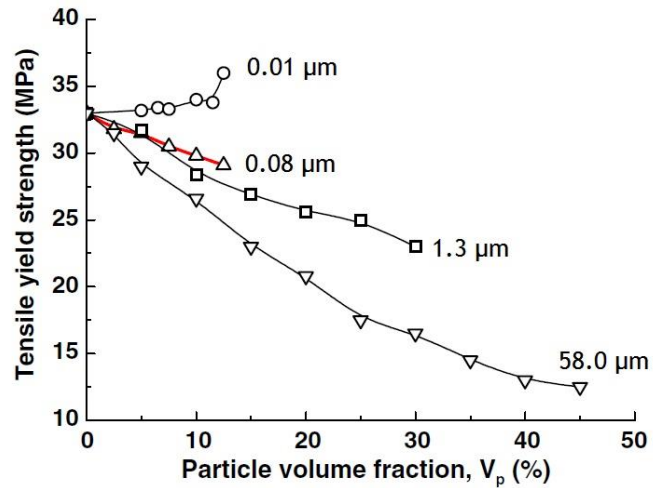
Figure 1.1. Effect of CaCO$_3$ particle size on the tensile yield strength of polypropylene - CaCO$_3$ composite material (Source: Pukanszky & Fekete, 1998).

CaCO$_3$ used in industry was usually produced from natural CaCO$_3$ minerals by crushing, grinding and sieving processes. CaCO$_3$ is available in nature in considerable amounts for the production of CaCO$_3$ from natural sources; however, the costs for crushing, grinding and sieving processes are high. Moreover, as shown in Figure 1.2, CaCO$_3$ produced from natural sources is in micron sizes and they are not in homogenous size distribution and desired purity (Sant'Anna, de Souza, de Araujo, Carvalho, & Yoshida, 2008). Therefore, nano calcite needs to be produced by recrystallization in desired properties.
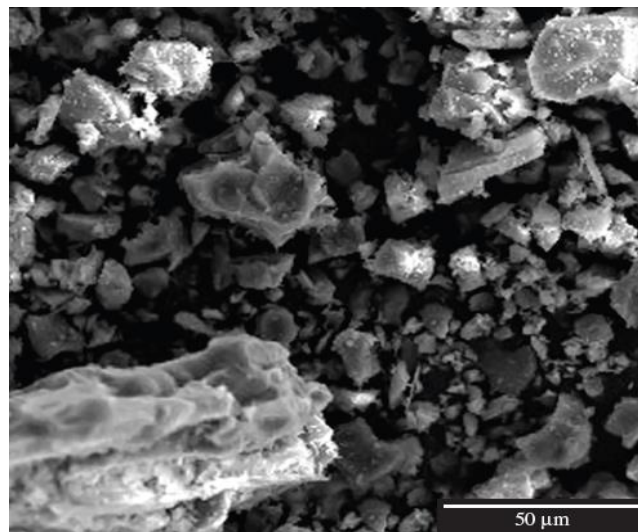
Figure 1.2. SEM images of commercial CaCO$_3$
(Source: Sant'Anna et al., 2008).

.

There are mainly two methods on the synthesis of $CaCO_3$: chemical method and carbonation method. In Kraft pulping method, $Ca(OH)_2$ is used as calcium ion source and Na_2CO_3 is utilized as carbonate ion source. Another chemical method is the mixing of solutions method. In mixing of solution method, $CaCl_2$ is utilized as calcium ion source and Na_2CO_3 as carbonate ion source. The production of $CaCO_3$ in chemical method have been performed in bench scale to investigate different parameters that affect the crystallization of $CaCO_3$ such as temperature, pH, organic and inorganic additives, supersaturation, stirring rate and the addition rate of feedings (Cölfen & Qi, 2001; Dalas & Koutsoukos, 1990; Giannimaras & Koutsoukos, 1987; Gomez-Morales, Torrent-Burgues, & Rodriguez-Clemente, 1996; Hari et al., 2006; Jung et al., 2000; Juvekar & Sharma, 1973; Kralj, Brečević, & Kontrec, 1997; Lerner, Azoury, & Sarig, 1989; Lopez-Macipe, Gomez-Morales, & Rodriguez-Clemente, 1996; Mann, 1988; Spanos & Koutsoukos, 1998; Vucak, Peric, Zmikic, & Pons, 2002; C. Y. Wang et al., 2006). $CaCO_3$ particles produced by chemical method are generally bigger than 3 micron (μm) and interesting structure such as flower-like, tulip-like and sculpture-like were obtained. Moreover, large scale production of nano $CaCO_3$ by chemical method is very difficult in industry. Therefore, nano calcite can only be possible to produce by using carbonation method in industrial scale. $CaCO_3$ production by the carbonation method which was usually produced in the industrial processes involves the following step: calcination of limestone, slaking and carbonation processes. Natural $CaCO_3$ rocks are calcinated to produce CaO and CO_2 (Eq.(1.1)). Then, quicklime (CaO) is transformed to slaked lime slurry by controlled addition of H_2O (Eq.(1.2)). Finally, as can be seen Eq.(1.3), slaked lime slurry is recrystallized by CO_2 (Carmona, Morales, & Clemente, 2003b).

$$CaCO_3\left(rock\right) \rightarrow CaO + CO_2 \tag{1.1}$$

$$CaO + H_2O \rightarrow Ca\left(OH\right)_2 \tag{1.2}$$

$$Ca\left(OH\right)_2 + CO_2 \rightarrow CaCO_3 + H_2O \tag{1.3}$$
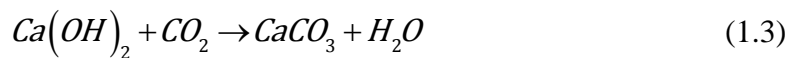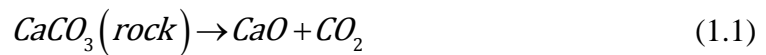
Since raw material is abundant in nature, the production capacity of $CaCO_3$ by recrystallization meets the market demands for desired properties. Although the

carbonation method has been widely studied, a standard procedure for the production of nano $CaCO_3$ could not suggested. Therefore, different approaches need to be defined to produce calcite in nano sizes, homogenous size distribution and desired morphologies.

In order to be able to produce $CaCO_3$ in nano sizes, homogeneous size distribution, and different morphologies, the objective of the present thesis were to investigate the stability of $CaCO_3$ in $Ca(OH)_2$, the progress and CO_2 pulsation in small penetration method, and the effect of different parameters on $CaCO_3$ particle size.

CHAPTER 2

LITERATURE REVIEW

2.1. Polymorphs of CaCO₃

CaCO$_3$ is an inorganic compound that has hydrated and anhydrous forms. Figure 2.1 shows the polymorphs of CaCO$_3$. The hydrated polymorphs are defined as an order of increasing solubility and classified as monohydrate CaCO$_3$ (MCC), hexahydrate CaCO$_3$ (HCC), amorphous CaCO$_3$ (ACC) (Carmona et al., 2003a; Gunasekaran & Anbalagan, 2008; Jung et al., 2000; Montes-Hernandez et al., 2008; Ukrainczyk et al., 2007; Xu et al., 2007). As seen in Figure 2.1, CaCO$_3$ has three different anhydrous forms, which are classified as calcite, vaterite and aragonite.
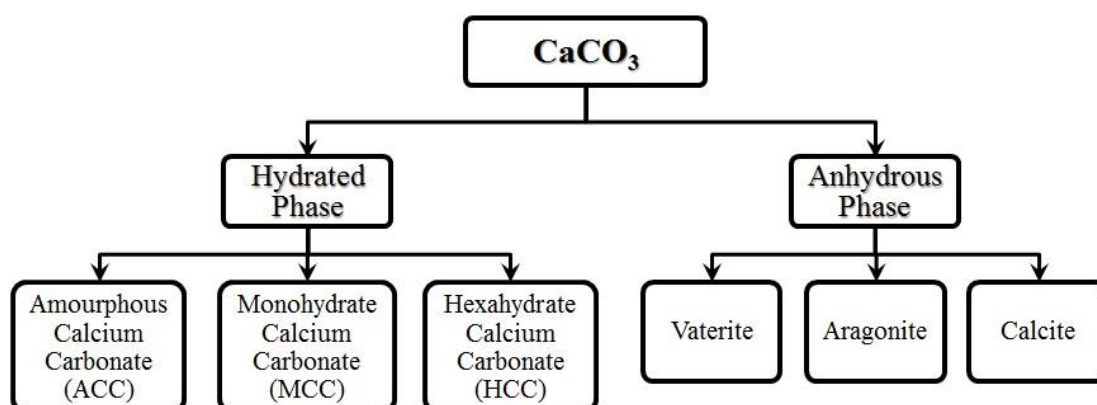
Figure 2.1. Polymorphs of CaCO$_3$.

Calcite is the thermodynamically most stable phase under standard conditions and belongs to trigonal-hexagonal-scalenohedral class (Stepkowska et al., 2003). Aragonite is the metastable polymorphs and belongs to orthorhombic dipyramidal class. Another is vaterite that belongs to hexagonal-dihexagonal dipyramidal class and vaterite is also metastable polymorphs of CaCO$_3$ (Montes-Hernandez et al., 2008; Ukrainczyk et al., 2007). Aragonite and vaterite can transform into the stable calcite (Montes-Hernandez et al., 2008). CaCO$_3$ has a rhombohedral structure that is the most stable morphological form (a punctual group of symmetry -32/m and a = b = 4.990 Å, c =

17.061 Å, $\alpha = \beta = 90^o$ and $\gamma = 120^o$) where the (104) face is the most stable surface (Domingo et al., 2006). Calcite crystals are characterized by some morphologies including scalenohedral bounded by the $(21\bar{1})$ form, the rhombohedral bounded by the (104) form and rhombo-scalenohedral in which crystals are bounded by both the (104) and $(21\bar{1})$ (Carmona et al., 2003b). Aragonite has needle-like morphology and is the high temperature phase and vaterite is the low temperature phase displaying a spherical morphology (Domingo et al., 2006). Figure 2.2 indicates the SEM images of vaterite, aragonite and calcite particles.
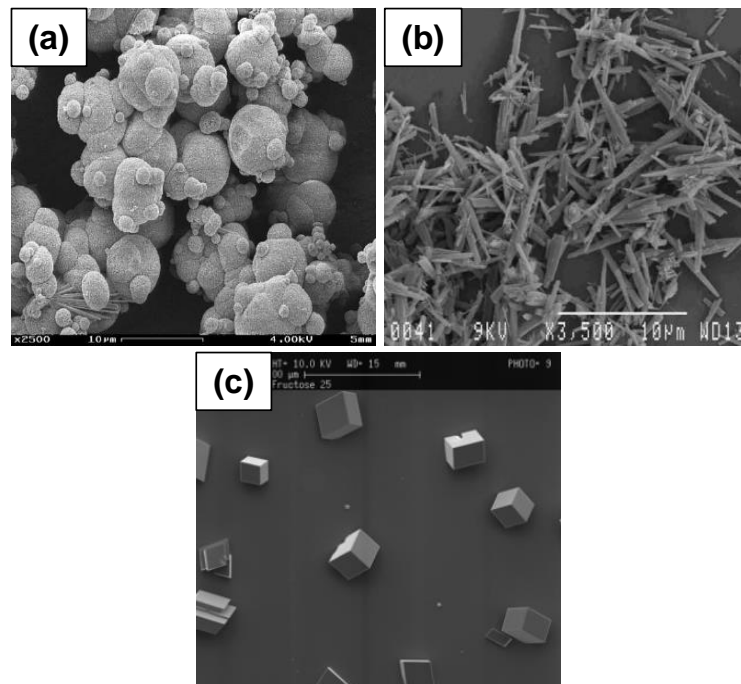
Figure 2.2. SEM images of $CaCO_3$ polymorphs: (a) vaterite (Vucak et al., 2002), (b) aragonite (Konno, Nanri, & Kitamura, 2003), and (c) calcite (Source: Dickinson & McGrath, 2004).

Figure 2.3 shows the established studies for the synthesis of $CaCO_3$ in different polymorphs and/or morphologies. Rhombohedral calcite is generally produced by mixing of solutions method, using low $Ca(OH)_2$ solution in carbonation route. Scalenohedral calcite is usually precipitated by fast Na_2CO_3 addition in Kraft pulping method, using high $Ca(OH)_2$ solution in carbonation route. Needle-like aragonite is generally produced by mixing of solutions method, slow Na_2CO_3 addition in Kraft pulping. Spherical vaterite is only precipitated by mixing of solutions method (Domingo et al., 2006). Moreover, some specific techniques are used for the controlling the $CaCO_3$

shapes. Technique have used to control the shape of $CaCO_3$ such as the use of high pressure (Mathur, 2001), addition of macromolecular additives (Cheng, Lei, Yu, & Zhao, 2004; Cölfen, 2003), applying magnetic field (E. Chibowski, Hołysz, Szcześ, & Chibowski, 2003b) or microwave irradiation (Rodriguez-Clemente & Gomez-Morales, 1996).

```
              ╭─────────────────────────────────────╮
              │  Established precipitation methods   │
              ╰─────────────────────────────────────╯
```

KRAFT PULPING METHOD $Ca(OH)_2 + Na_2CO_3 \leftrightarrow CaCO_3 + 2NaOH$	**MIXING OF SOLUTIONS** $CaCl_2 + Na_2CO_3 + NaOH \leftrightarrow CaCO_3 + 2NaCl + H_2O$

Batch: fast Na_2CO_3 addition	Batch: slow Na_2CO_3 addition	Continuous: liquid - liquid	Continuous: liquid - solid
Scalenohedral calcite favored	**Needle-like calcite** favored		

Spheroidal vaterite (favored at low temperature and low pH), **needle-like aragonite** (favorite at high temperature and high pH) **and scalenohedral/rombohedral calcite**

CARBONATION ROUTE
$Ca(OH)_2 + CO_2 \leftrightarrow CaCO_3 + H_2O$

Low $Ca(OH)_2$: liquid-gas system $Ca(OH)_2$ obtained by mixing $CaCl_2$ & NaOH Technical studies for industrial process	High $Ca(OH)_2$: liquid-solid-gas system $Ca(OH)_2$ obtained by hydrating CaO Industrial process
Rombohedral calcite favored	**Scalenohedral calcite** favored

Figure 2.3. Established procedures for the controlled precipitation of $CaCO_3$ (Source: Domingo et al., 2006).

2.2. Usage of $CaCO_3$ as Filling Material

$CaCO_3$ has been used as filling materials in various industries (Campos et al., 2007; Carmona et al., 2003c; Jung et al., 2000; Lam et al., 2009; Matahwa et al., 2008; Sheng et al., 2006a; Sondi et al., 2008; Ukrainczyk et al., 2007). Calcite as one of the most important polymorph of $CaCO_3$ has been widely used for the production of

composite material. Figure 2.4 indicates pure polypropylene, nano $CaCO_3$ particles, and polypropylene-$CaCO_3$ nano composite polymeric material where a 9.2 % of 44 nm-size $CaCO_3$ particles were mixed with polypropylene. In this case, the Izod impact strength of polymeric composite material was increased about 2.5 times (Chan, Wu, Li, & Cheung, 2002).
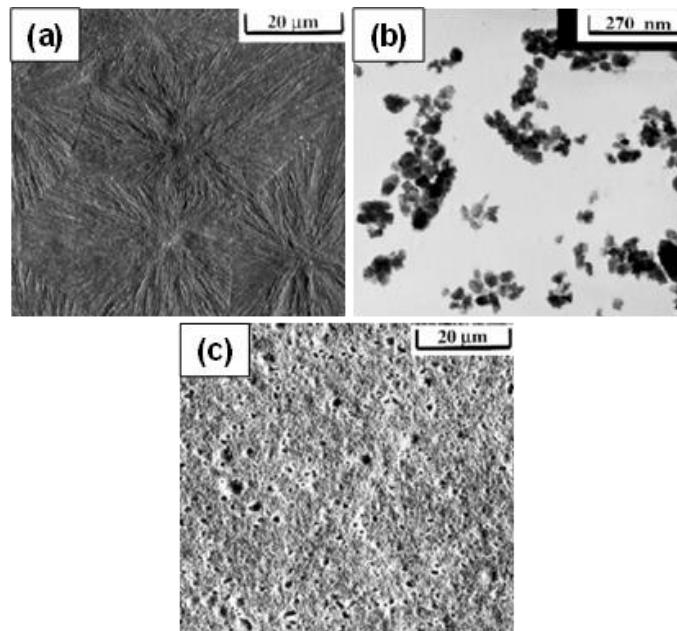
Figure 2.4. SEM and TEM images of (a) pure Polypropylene, (b) the $CaCO_3$ nanoparticles, and (c) nanocomposites with 9.2 vol% filler (Source: Chan et al., 2002).

Figure 2.5a shows the polypropylene-$CaCO_3$ composites material where a 20% of 70 nm-size $CaCO_3$ crystals were added into the polypropylene. Figure 2.5b the shows Izod impact strength of polypropylene-$CaCO_3$ polymeric composites material with different annealing conditions. The Izod impact strength of the 150 ^{o}C-annealed polymeric nanocomposite was 3.5 times higher than the neat polypropylene. As shown in Figure 2.5b, the izod impact strength of the 155 ^{o}C-annealed nanocomposite was increased 5 times with respect to the neat polypropylene (Lin, Chen, Chan, & Wu, 2008).
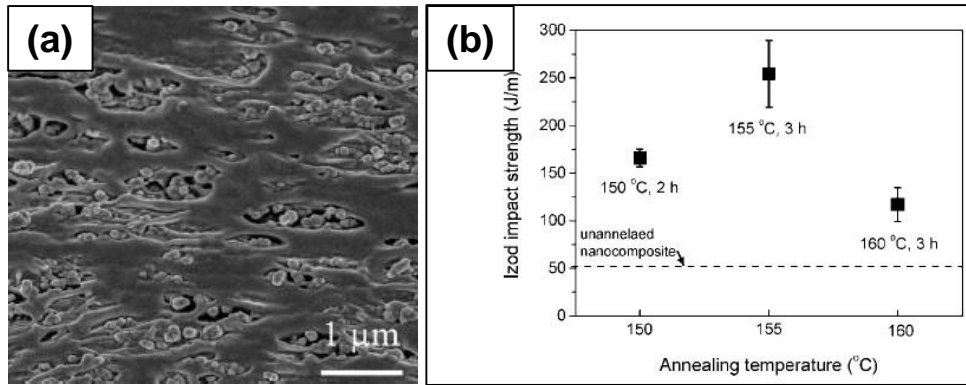
Figure 2.5. SEM micrographs of the (a) Low Density Polyethylene – CaCO₃ composite material and (b) its Izod impact strength with different annealing condition (Source: Lin et al., 2008).

Table 2.1 summarizes the studies about the different composite materials using CaCO₃ as filling material. As shown in the figure, when the particle size used in the studies were in nano-size, the improvements in the physical properties of the composite materials were significant.

Table 2.1. Using CaCO₃ as filler material in various studies.

Material	CaCO₃ size (µm)	Observed Effect	Reference
Polystyrene	0.03–0.1	➢ Enhancement in tensile yield strength and polymerization activity ➢ Increase in Young's Modulus and creep resistance	(Guo, Yu, & Cheng, 2006)
Polypropylene	0.04	➢ Increase in Young's Modulus and tensile	(Liang, 2007)
PVC	0.1	➢ Increase in tensile strength (10 %) and potency factor (24 %) ➢ Increase in elongation at break (150 %)	(Hu, Dong, & Zhen, 2009)

Table 2.1. (cont.)

Material	CaCO$_3$ size (μm)	Observed Effect	Reference
Polypropylene	0.11–2.13	➢ Increase in viscosity (3 fold) ➢ Increase in tensile yield strength (1.5 fold)	(Kiss, Fekete, & Pukanszky, 2007)
Polystyrene	0.04–0.08	➢ A very tight encapsulation between polystyrene and calcite	(Sheng et al., 2006a)
Acrylnitrile butadiene-strene copolymer	0.04–1.4	➢ Decrease in melting flow with the increase in the amount of the filling material (10 %)	(Tang & Liang, 2003)
High density polyethylene	0.44 0.7 3.5	➢ Increase in harness and toughness ➢ Increase in impact energy (50 %) ➢ Increase in Young's Modulus and impact energy (50 %)	(Bartczak, Argon, Cohen, & Kowalewski, 1999)
High density polyethylene	0.07	➢ Increase in Yield Stress (10 %) ➢ Increase in Young's Modulus (35 %) ➢ Increase in elongation at break (500 %)	(Zebarjad & Sajjadi, 2008)
Polyester amide	0.1–0.12	➢ Improvement in mechanical properties	(Liu, Zou, Cao, & Luo, 2007)
Polyethylene film	3 – 5	➢ Formation of crystal phase at polyethylene surface and increase in mechanical strength	(Silva, Pereira, Muniz, & Rubira, 2009)

2.3. Production Methods for Calcite

There are mainly two methods to produce $CaCO_3$: chemical method and carbonization method. These methods were shown briefly in Figure 2.6. The chemical method can also be divided into two process called as Solution method and Kraft method. In Solution method, $CaCI_2$ used as Ca^{++} ion source, and Na_2CO_3 utilized as CO_3^{2-} ion source, are mixed at certain conditions (Bolze et al., 2002; Pontoni, Bolze, Dingenouts, Narayanan, & Ballauff, 2003; Rieger, Thieme, & Schmidt, 2000; Wray & Daniels, 1957). There are several techniques to produce $CaCO_3$ from the reaction between Ca^{++} and CO_3^{2-} ions in solution method. These are batch and double-jet technique. In batch technique, known amount of Na_2CO_3 solution is added into $CaCl_2$ solution, which is performed in a batch reactor (Wray & Daniels, 1957). In double-jet technique, the solutions of Na_2CO_3 and $CaCl_2$ are pumped simultaneously into a reactor. The causticizing reaction is carried out in the chemical recovery of the Kraft Pulping Method, and $CaCO_3$ is a by-product in the NaOH production (Konno et al., 2003). In Kraft Method, $Ca(OH)_2$ used as Ca^{++} ion source and Na_2CO_3 used as CO_3^{2-} ion source, are mixed with known amounts and conditions (Konno et al., 2003; Merris, 1998). Since the parameters studied in chemical method can easily be controlled at the laboratory conditions, the effects of some parameters such as supersaturation, pH, stirring rate, temperature, feeding rates, additives on the crystallization morphology can be investigated (Y.S. Han, Hadiko, Fuji, & Takahashi, 2006b; Kitamura & Yasui, 2000; Kralj et al., 1997; Lopez, Zuddas, & Faivre, 2009). For example, the effect of the NaOH addition at various temperatures was studied using batch operations (Konno et al., 2003). However, the particle sizes of the product $CaCO_3$ were larger than micron sizes and it is very difficult to control the nucleation and crystal growth rate in chemical method. Although the chemical method is an easy method for the $CaCO_3$ production at the laboratory conditions, the production of $CaCO_3$ in nano sizes using chemical method could not be possible at large scale in industry.
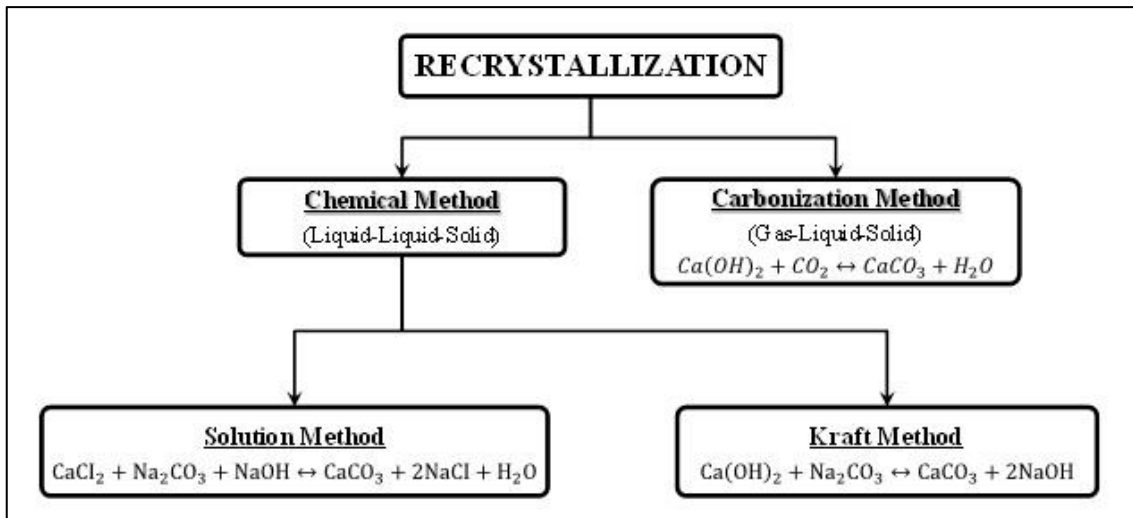
Figure 2.6. Production methods of CaCO$_3$.

Figure 2.7 shows typical CaCO$_3$ particles produced using chemical method (Konno et al., 2003). As shown in the figure, aggregation of particles was observed. The amount of pillar-like aragonite crystals were detected at 50°C as given in Figure 2.7a. The crystal sizes were significantly larger than 4 μm. At 75°C, granular calcite particles were obtained. These crystals were in aggregated form. At 75°C, needle-like aragonite particles in 10-20 μm in length were obtained.
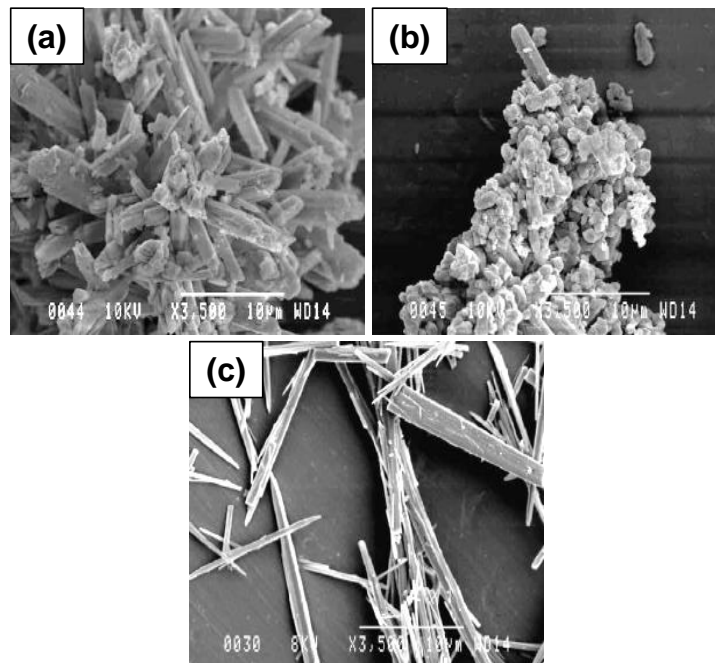
Figure 2.7. SEM images of CaCO$_3$ particles obtained by using chemical method: (a) Ca(OH)$_2$/Na$_2$CO$_3$=1:1.2 (50 ^{o}C, 60 min), (b) Ca(OH)$_2$/Na$_2$CO$_3$=1:1.2 (75 ^{o}C, 60 min), and (c) Ca(OH)$_2$/Na$_2$CO$_3$=1:1 (75 ^{o}C, 60 min) (Source: Konno et al., 2003).

The most widely used method for the production of $CaCO_3$ at industrial scale is the carbonization method. The raw materials for the carbonization method are cheap and readily available (Carmona et al., 2003a; Carmona, Morales, Sainz, Loste, & Clemente, 2004; Perić, Vučak, & Krstulović, 1995; Uebo, Yamazaki, & Yoshida, 1992). Figure 2.8 shows the typical carbonization method used for the synthesis of $CaCO_3$. The production of $CaCO_3$ by carbonization route generally consists of bubbling CO_2 gas through an aqueous slurry of slaked lime ($Ca(OH)_2$ suspension) in a batch or semi-batch process (Carmona et al., 2003a, 2003b; Carmona et al., 2003c; Carmona et al., 2004; Ukrainczyk et al., 2007; Ukrainczyk, Kontrec, & Kralj, 2009). $Ca(OH)_2$ slurry or its solution was prepared in a $Ca(OH)_2$ feeding tank at desired concentration. The $Ca(OH)_2$ solution was fed into crystallization tank to perform crystallization by a pump. The pH and conductivity values were set to desired values and adjusted by $Ca(OH)_2$ feeding flow rates and CO_2 feeding rates into the crystallization tank. The $Ca(OH)_2$ slurry or solution, and crystallization medium were homogenized by stirring. The temperature was set to a constant value during crystallization. CO_2 is generally fed into crystallization medium as bubbles. When $Ca(OH)_2$ feeding was stopped, CO_2 feeding to the crystallization medium was continued to complete crystallization. When the pH decreased to about 7.0, the reaction was terminated. Samples were collected at the end of the reaction and analyzed (Carmona et al., 2003b). Here, high CO_2 flow rates within the $Ca(OH)_2$ slurries may cause large and aggregated particles.
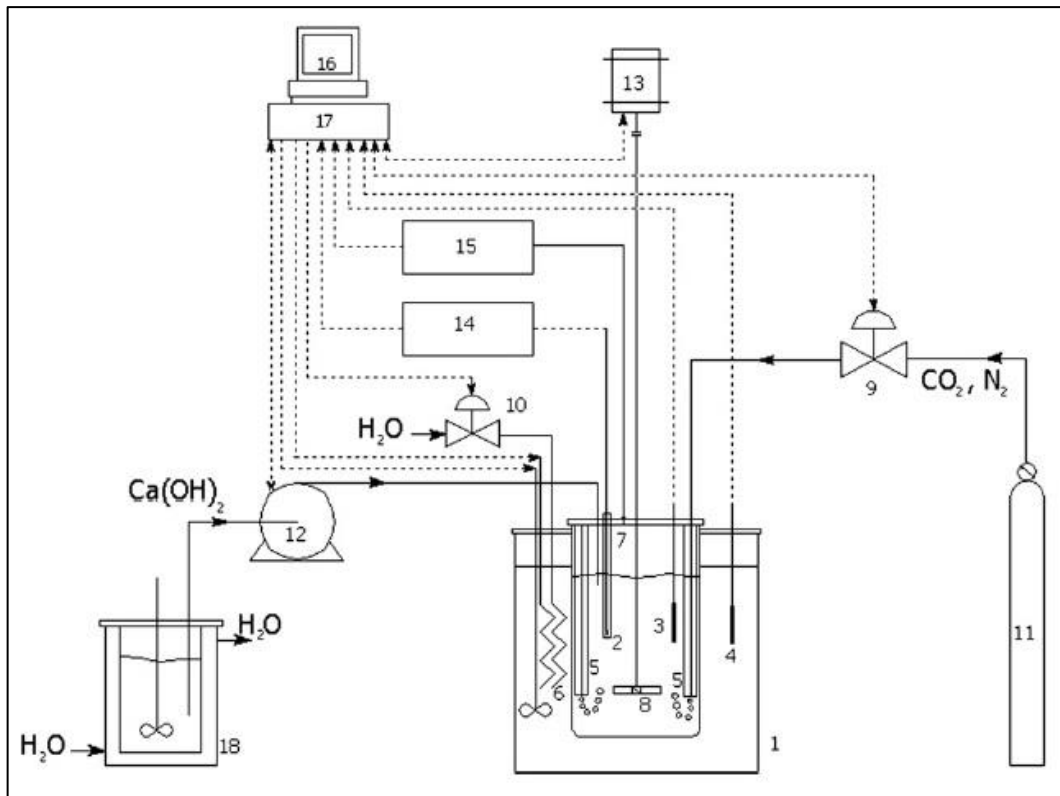
Figure 2.8. Schematic drawing of a typical production line of $CaCO_3$ by carbonization method: (1) jacketed reactor, (2) conductivity cell, (3,4) temperature probe, (5) baffles with nozzle for gas injection, (6) heater and cooler, (7) gas outlet, (8) 45o pitched blade turbine, (9) regulation valve, (10) magnetic valve, (11) gas supply bottle, (12) pump, (13) mixing motor, (14) conductivity meter, (15) CO_2 analyzer, (16) computer provided with control software, (17) controller, and (18) jacketed feeding tank (Source: Ukrainczyk et al., 2007).

Figure 2.9 shows the SEM images of the typical $CaCO_3$ particles obtained using carbonization process mentioned above. As given in the figure, the $CaCO_3$ particle sizes were larger than micron sizes. Moreover, the different morphologies for aggregated and chain-like particles were obtained. One reason to this could be related to the sharply decrease in pH value. When the pumping of the $Ca(OH)_2$ from $Ca(OH)_2$ preparation tank was stopped and CO_2 injection was continued to reaction medium, pH sharply decreases, resulting in the solubility of both $Ca(OH)_2$ and $CaCO_3$ to increase. Therefore, the surface charge of the $CaCO_3$ produced may change from negative to positive. The second reason could be defined the presence of alive ions and clusters in the crystallization mechanism which means that solution is composed of nuclei and growing $CaCO_3$ particles, resulting in growing particles. Therefore, there must be some technical errors made during the experiments.
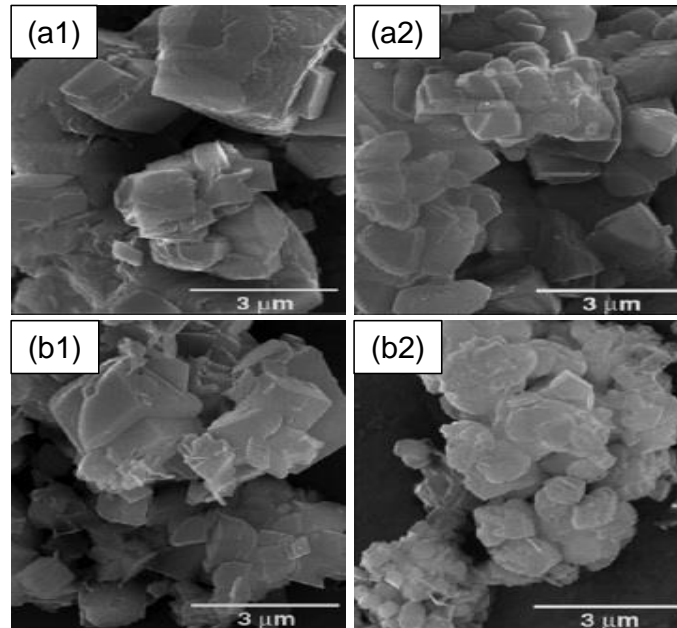
Figure 2.9. SEM images of CaCO$_3$ obtained by carbonization method: (a) 25 ^{o}C, (b) 30 ^{o}C, (1) 1 mS/cm, and (2) 3 mS/cm (Source: Carmona et al., 2003b).

2.4. The mechanisms of CaCO$_3$ Crystallization

The mechanism of CaCO$_3$ crystallization has been widely investigated in literature. However, there are some unexplained parts of CaCO$_3$ crystallization mechanism. Figure 2.10 shows the classical and non-classical crystallization, and four different pathways were proposed in classical crystallization mechanism. As presented in the figure, some nucleation clusters form the reaction between Ca^{++} and CO$_3^{2-}$ ions and grow to form primary nanoparticles until they reach the size of critical crystal nucleus growing to primary nanoparticles. Then, the primer can be amplified to a single crystal or arranged (path a) to form an iso-oriented crystal (path b). If the primary particles, known as nucleus, get covered by additives before they undergo a mesoscale assembly, they can form a mesocrystal (path c). Path d represents the amorphous particles to be formed into amorphous phase which leads to the complicated morphologies (Xu et al., 2007).
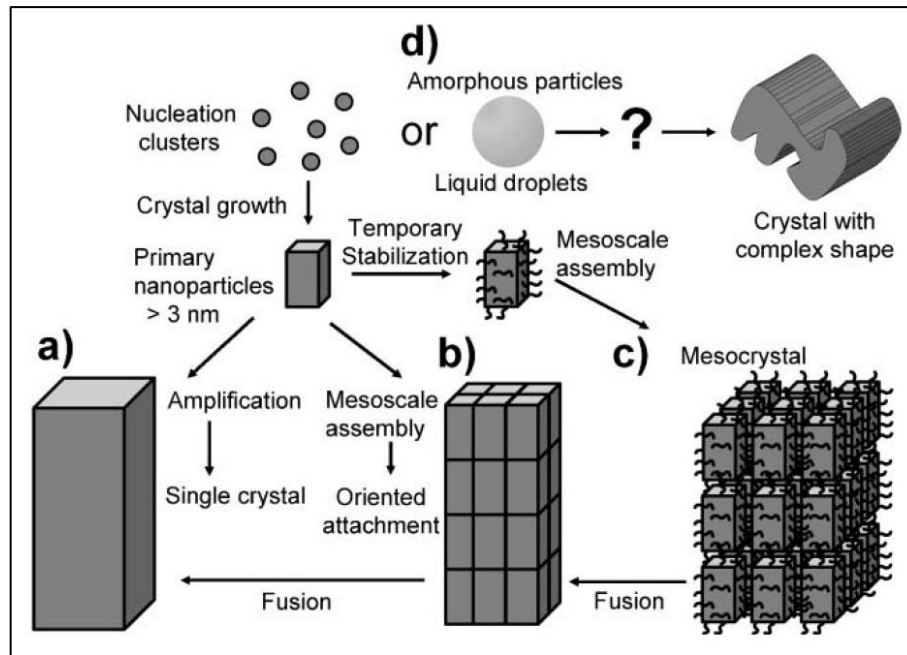
Figure 2.10. Schematic drawing of classical and non-clasical crystaalization
(Source: Xu et al., 2007).

Figure 2.11 shows the comparison of classical and novel crystallization mechanisms proposed by Gebauer et al., (Gebauer, Volkel, & Colfen, 2008). Novel model suggests that calcium ions binding during the pre-nucleation stage are related to the carbonate ion concentration, resulting in the stable cluster formation from these ions. The clusters and ions are in equilibrium, which is pH-dependent. Moreover, the stable clusters could form in both the under saturated and supersaturated stages. They stated that the number of ions combined in clusters (z) remains unknown, because the thermodynamic of cluster formation cannot be quantatively characterized by assuming the equilibrium as shown in Eq.1. It was indicated that hydrodynamic diameter of a cluster was found to be 2 nm in the supersaturated stage, and this size corresponds to about 70 Ca^{2+} and CO_3^{2-} ions combined in a single cluster on average. Then, larger clusters having the hydrodynamic diameter of about 4 nm was detected with low statistical relevance. The larger cluster species having the hydrodynamic diameter of about 6 nm was found in the early post-nucleation stage. After nucleation, the smaller cluster species cannot be detected, indicating that nucleation takes place through cluster aggregation. It was found that the ACC I is related to an amorphous phase exhibiting calcite, and ACC II is related to an amorphous phase exhibiting vaterite form as shown in Figure 2.11. The control mechanism of the nucleation of ACC phases remains

unknown. The control mechanism could be related to either the thermodynamics or kinetics (Gebauer et al., 2008).

$$z \times Ca^{2+} + z \times CO_3^{2-} \leftrightarrow \left[CaCO_3 \right]_Z \qquad (2.1)$$
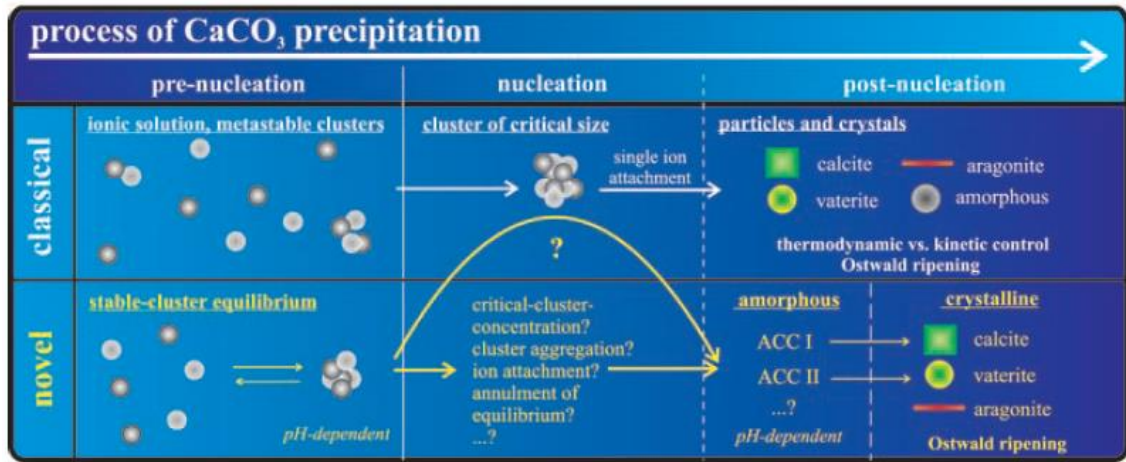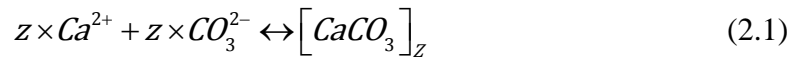
Figure 2.11. Schematic illustration of classical and novel CaCO$_3$ crystallization mechanism (Source: Gebauer et al., 2008).

Figure 2.12 shows the possible sizes and the mechanism of CaCO$_3$ formation (Pouget et al., 2009). In this study, pre-nucleation clusters formed from the complexation of Ca^{2+} and CO$_3^{2-}$ were found to be about 0.6 to 1.1 nm (step 0). These clusters aggregated to form 30 nm ACC nanoparticles (step 1). Then, these ACC particles clustered and start to grow to about 70 to 120 nm on the surface of the organic matrix, and it was claimed that the size of about 120 nm is a critical upper limit for the stability of the amorphous phase (step 2). The poorly crystalline particles were formed as a result of crystallization (step 3). Nano crystalline domains formed inside the amorphous matrix, and polycrystalline CaCO$_3$ had a minimal particle diameter of about 70 nm (step 4). The prevalent growth of the crystalline domain was stabilized by the template (step 5). Lastly, the oriented single crystals were formed and continued to grow. It was clearly presented that the pre-nucleation clusters persisted after nucleation, on the contrary to a study suggested by Gebauer et al., (Gebauer et al., 2008). They claimed that particles produced by the complexation of Ca^{2+} and CO$_3^{2-}$ ions were in equilibrium with the ions and the clusters in aqueous solution. Another significant point is that the large particles could be formed by the dissolution and the re-precipitation mechanism (Pouget et al., 2009).
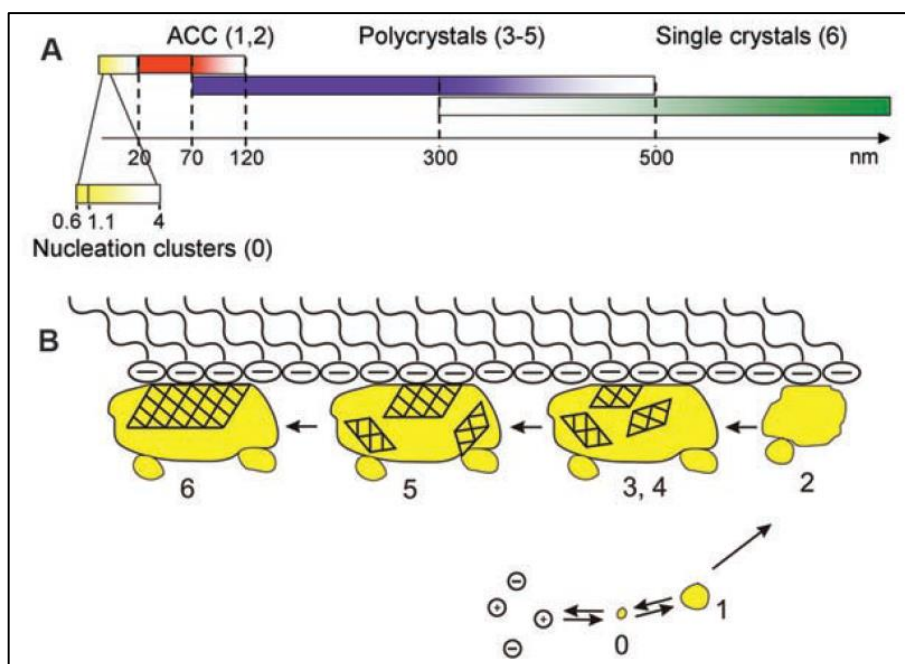
Figure 2.12. The different stages of template-controlled $CaCO_3$ formation
(Source: Pouget et al., 2009).

2.5. Efforts in Nano Calcite Production

In literature, various production methods have been applied for the production of nano $CaCO_3$. It was argued that The control of the nucleation and crystal growth by supersaturated solution is the key factor to control the crystal size (Ford, 2004; Kashchiev & Van Rosmalen, 2003). Since nano particles can be formed from small nuclei, and then grow to form larger particles, the nucleation section and the crystal growth section were suggested to be separated to obtain nano particles (G. Chen, Luo, Xu, & Wang, 2004). For an efficient CO_2 dissolution, a membrane reactor was suggested (K. Wang, Wang, Chen, Luo, & Wang, 2007).

The nucleation section is more sensitive to supersaturation (Isopescu, Mocioi, Zahanagiu, & Filipescu, 1996). The supersaturation ratio defined by Eq. (2.2) is an important factor which should be high enough for the production of nano particles (K. Wang et al., 2007).

$$s = \frac{\left[Ca^{2+} \right]\left[CO_3^{2-} \right]}{K_{sp}} \tag{2.2}$$

where $[Ca^{2+}]$ is the concentration of calcium ion (mol/dm^3), $[CO_3^{2-}]$ is the concentration of carbonate ion (mol/dm^3), and K_{sp} is the solubility product of $CaCO_3$. Therefore, high concentrations of calcium ions and/or carbonate ions are required to produce nanoscale particles.

The ratio of Ca^{++} and CO_3^{2-} ion concentrations is found to be another important factor to produce $CaCO_3$ in nanoscale. As shown in Figure 2.13, the crystallization rate is maximum when the ratio of Ca^{++} and CO_3^{2-} ion concentrations is about 1. On the other hand, when the ratio of Ca^{++} and CO_3^{2-} ion concentrations is much greater or much lower than 1, the crystallization rate is significantly slower (Nehrke, Reichart, Van Cappellen, Meile, & Bijma, 2007). We argue from Eq. (2.2) and Figure 2.13 that the $CaCO_3$ crystal size could be controlled by introducing the CO_2 gas into reaction medium slowly and with a controllable fashion.
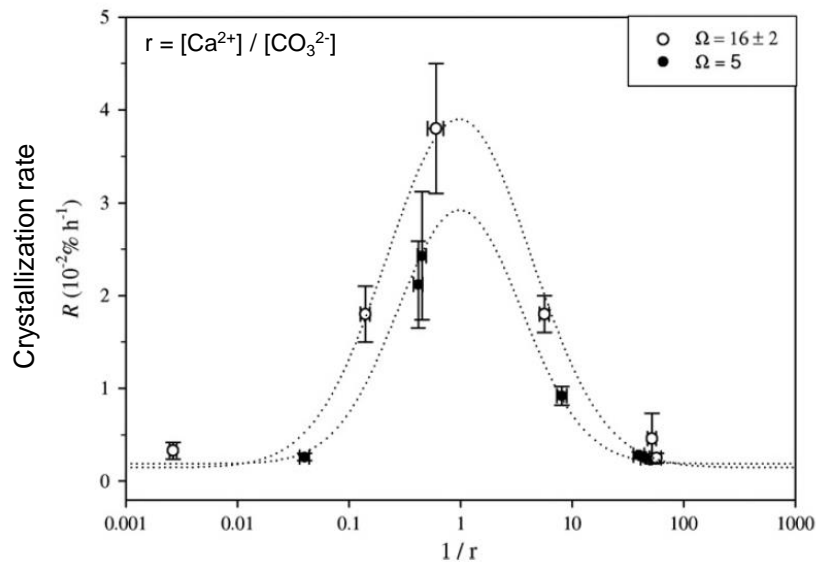
Figure 2.13. Growth rate versus the inverse of the solution the ratio of Ca^{++} and CO_3^{2-}, r, for two different degrees of supersaturation with respect to calcite (Source: Nehrke et al., 2007).

Wang et al., (2007) stated that nice mixing and fast mass transfer rate of CO_2 were required to enhance supersaturation (K. Wang et al., 2007). As shown in Figure 2.14, they used a membrane reactor to efficiently disperse CO_2 and increase the dissolution rate. The pump was used for the recirculation of $Ca(OH)_2$ solution between the membrane mini reactor and stirring tank indicating that nucleation and crystal growth section could be separated by the membrane reactor and the stirring tank.

Therefore, different sizes of $CaCO_3$ particles, whose average diameters ranged from 34.3 to 110 nm, were synthesized.
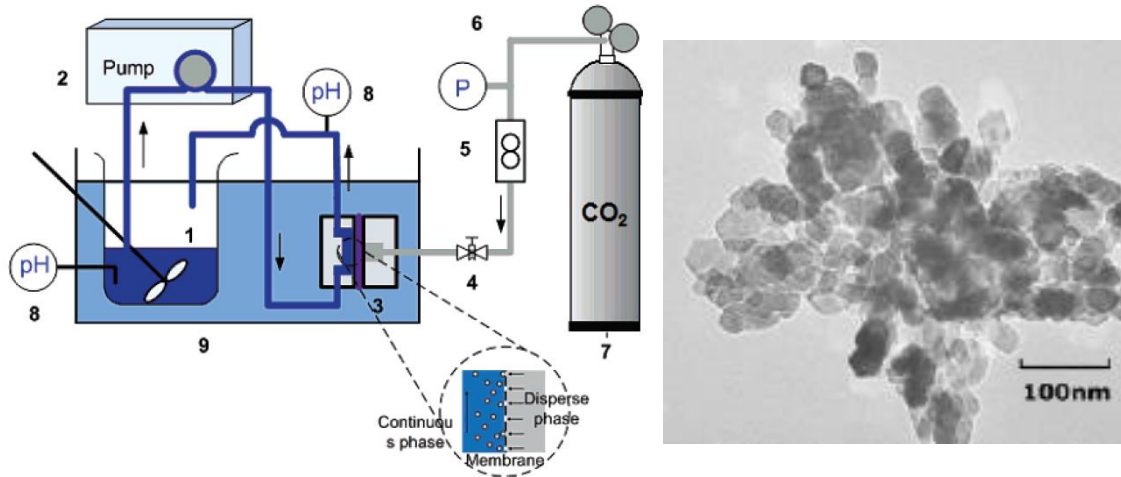
Figure 2.14. A schematic illustration of membrane dispersion minireactor: (1) stirring vessel, (2) measuring pump, (3) membrane dispersion minireactor, (4) valve, (5) flow meter, (6) pressure gauges, (7) source of the mixed gas, and (8) pH indicator, (temperature control bath (Source: K. Wang et al., 2007).

Wu et al., (2007) suggested a micropore membrane reactor as shown in Figure 2.15. Micropore membrane reactor enhance process of momentum transfer, mass transfer and reaction rate (Wu, Wang, Zhu, & Wang, 2007). The microporous membrane with a 10 μm pore size at the bottom of the reactor was used to obtain small gas bubbles. Once the small CO_2 bubbles were homogeneously distributed in the column reactor, cubic $CaCO_3$ particles were shown to be produced about 40 nm.
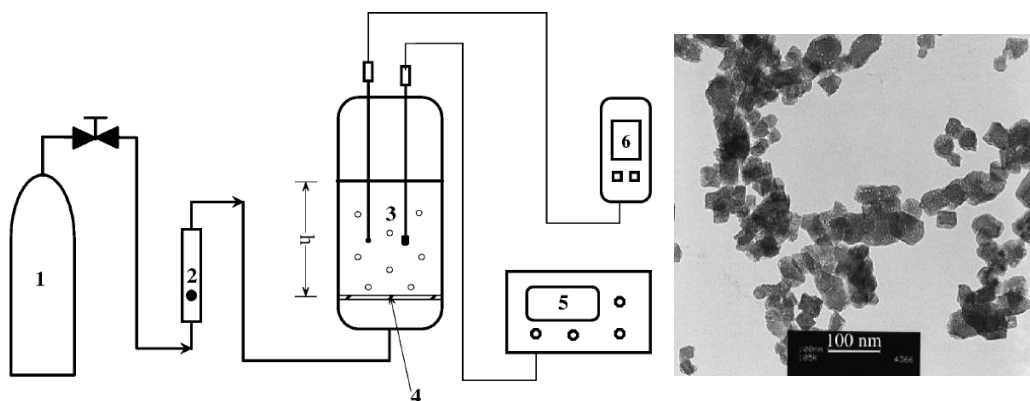
Figure 2.15. A schematic of experimental setup.
(Source: Wu et al., 2007).

Chen et al., (2000) proposed high-gravity reactive precipitation for the production of nano $CaCO_3$. Since the characteristic nucleation time is about less than 1 microsecond (μs) in aqueous phase and the mixing time of ions in molecular level is about 5-50 milliseconds (ms), the particle size distribution in the stirring tank could not be achieved at the desired levels. Therefore, high-gravity reactor was used shown in Figure 2.16 in order to separate the nucleation section and the crystal growth section from each other. The rate of mass transfer between $Ca(OH)_2$ and CO_2 could be increased at the gas-liquid interface and the micromixing was obtained by the high-gravity reactor. The high-gravity reactive precipitation technique was performed in the reactor consisted of a fixed bed which rotates on its own axis. $Ca(OH)_2$ solution pumped from stirring tank into the bed flowing in the radial direction under centrifugal force in the high-gravity reactor, and then recirculated to the stirring tank after a short contact time between thin film obtained in the high-gravity reactor and CO_2. Therefore, nucleation and crystal growth sections could be separated from each other. As shown in the figure, the $CaCO_3$ particles in the range of 17-36 nm were obtained using High-gravity reactor (J. F. Chen, Wang, Guo, Wang, & Zheng, 2000). (Song, Chu, M., & Chen, 2003).
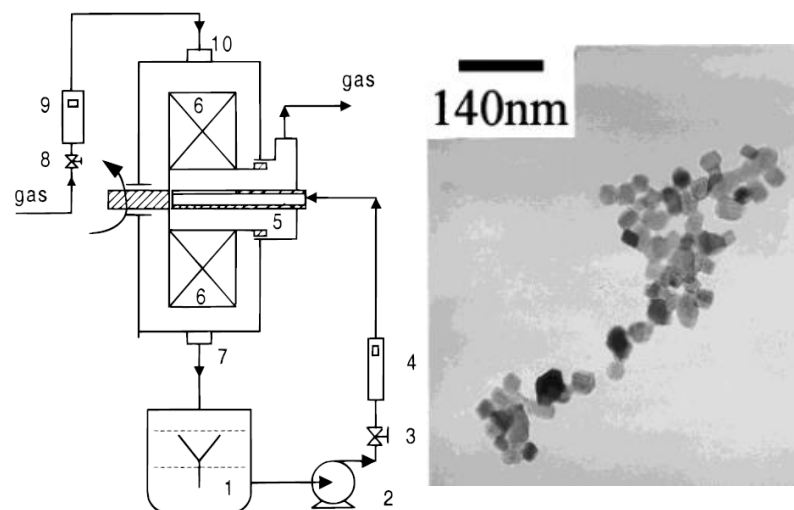
Figure 2.16. Schematic of High-gravity reactive precipitation: (1) stirred tank, (2) pump, (3) valve, (4) rotor flow meter, (5) distributor, (6) packed rotator, (7) outlet, (8) valve, (9) rotor flow meter, and (10) inlet (Source: J. F. Chen et al., 2000).

The effect of pH on the $CaCO_3$ particle size, size distribution, and $CaCO_3$ crystallization has been widely investigated in literature. Wang et al., (1998) stated that

the dissolution rate of $Ca(OH)_2$ increased exponentially with decreased values of pH over the range of $6.5 - 3.0$ (J. Wang, Kenner, Li, & Khang, 1998). Since pH value is generally greater than 12 during $CaCO_3$ crystallization, the dissolution rate of $Ca(OH)_2$ would be lower at about pH 12. Therefore, the Ca^{++} and OH^- ion concentrations obtained at about pH 12 would be lower than their theoretical values. In $CaCO_3$ precipitation, the types of ions and the electrical charges on the clusters and on the growing $CaCO_3$ particles could be different depending on pH.

As shown in Figure 2.17, Fenter et al., (2000) suggested that the surface of $CaCO_3$ particles would be negatively charged at higher pH's (pH>10). Since the $CaCO_3$ surface would be covered by water molecules at pH's between 8 and 10, it becomes positively charged. The surface would be positively charged at lower pH's (pH<8) (Fenter et al., 2000). Since pH sharply decreases at about zero conductivity in the carbonation route, the aggregation tendency and increase in the $CaCO_3$ sizes at these pH values could be related to the changes in the surface charges.
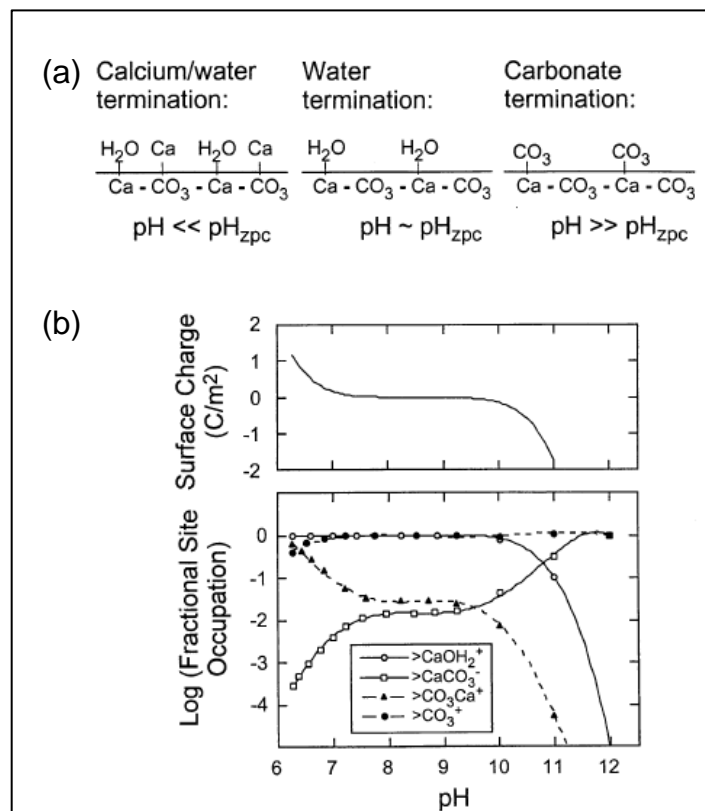
Figure 2.17. The predicted variation of the calcite surface speciation as a function of pH (Van Cappellen, Charlet, Stumm, & Wersin, 1993) with (a) a schematic summary of the different surface terminations, and (b) the predicted surface speciation as a function of pH under conditions of calcite–water equilibrium at $P_{CO2} = 10^{-3.5}$ atm and $T = 25^oC$ (Source: Fenter et al., 2000).

In the literature, various approaches were applied for the synthesis of nano calcite; however, a proven and repeatable method could not be suggested to produce $CaCO_3$ in nano sized, homogeneous size distribution and different morphologies, which were the main objectives of the present thesis.

CHAPTER 3

MATERIALS AND METHODS

3.1. Materials

Chemicals such as calcium hydroxide ($Ca(OH)_2$), commercial calcium carbonate ($CaCO_3$), acetone, were all purchased from Merck Chemicals. $Ca(OH)_2$ was supplied with a 96% purity, of which 3% was $CaCO_3$, and 1% were other impurities. Nitrogen (N_2) and carbon dioxide (CO_2) were purchased from Karbogaz A.Ş, Turkey.

3.2. Methods

3.2.1. Stability of CaCO$_3$ in Ca(OH)$_2$

The dissolution of both commercial $Ca(OH)_2$ and $CaCO_3$ in ultrapure water was studied. The pH and conductivity values for both $Ca(OH)_2$ and $CaCO_3$ solutions and slurry were measured at different concentrations. Before the experiments, the N_2 was fed into the 5-neck jacketed reactor to maintain CO_2 free atmosphere in the reactor. A 0.0667 g of $Ca(OH)_2$ was added into 900 ml of ultrapure water in a 5-neck jacketed reactor to prepare a 1 mM $Ca(OH)_2$ solution by stirring on a stir bar at 600 rpm at 23 ^{o}C. Then, additional $Ca(OH)_2$ powders were added into the solution to obtain 5, 10, 15, 20, 30, 50, and 100 mM of $Ca(OH)_2$ solution and slurries. pH and conductivity values were measured for each concentration. A 2 ml of samples were withdrawn from the solution when each concentration was prepared and the zeta potential and average particle size were measured by Malvern Zeta Sizer − Nano ZS. After measurements, the samples were poured back to the 5-neck jacketed reactor.

The dissolution of various $Ca(OH)_2$ concentrations in 10 mM $CaCO_3$ solution was studied to investigate the stability of $CaCO_3$ in $Ca(OH)_2$. A 9.0079 g of $CaCO_3$ was added into 900 ml of ultrapure water in a 5-neck jacketed reactor to prepare 10 mM of $CaCO_3$ solution. Then, a 0.0667 g of $Ca(OH)_2$ was fed into the 5-neck jacketed reactor to obtain the mixture (1 mM $Ca(OH)_2$ in 10 mM $CaCO_3$). Additional amounts of

Ca(OH)$_2$ were also added into the mixture for each concentration. pH and conductivity values were measured for each concentration. The CaCO$_3$ stability in 10 mM Ca(OH)$_2$ concentrations was also studied at 1, 5, 10, 15, 20, 30, 50 and 100 mM CaCO$_3$ solutions and slurries. On the other hand, the pH and conductivity values for 10 mM Ca(OH)$_2$ at various CaCO$_3$ concentrations were also determined by the same procedure. The zeta potential and particle sizes were also measured by taking 2 ml of sample for each concentration and they were returned to the reactor after measurement. Similar measurement was repeated for CaCO$_3$ concentration in 10 mM Ca(OH)$_2$ solution.

3.2.2. Method Development

The amount of gas dissolved in the liquid phase may be controlled by a short contact time between gas and liquid phases at the flow system. Figure 3.1 shows the possible velocity, concentration and small penetration thickness for a small penetration method. In this method, CO$_2$ in gas phase was tried to be transformed into the liquid phase within a small penetration thickness. The possible ion concentrations were also depicted in Figure 3.1. Since dissolved CO$_2$ will react to form CO$_3^{2-}$ at high pH, if would lead to such profiles and increase the mass transfer rates at the surface.
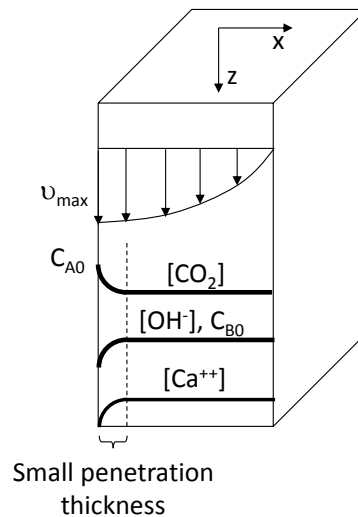
Figure 3.1. Possible velocity and concentration profile for the proposed small penetration method.

The diffusion of CO$_2$ from gas phase into the liquid phase with a small penetration theory can be given as shown in Eq.(3.1).

$$v_{max} \frac{\partial C_A}{\partial z} = D_{AB} \frac{\partial^2 C_A}{\partial x^2} - k_2 C_A C_B \qquad (3.1)$$

where v_{max} is maximum velocity of the liquid phase, C_A and C_B are the dissolved CO_2 concentration and OH^- ion concentration in the liquid phase, respectively, k_2 is the reaction rate constant between CO_2 and OH^- ions, and D_{AB} is the diffusion coefficient.

Boundary conditions can be expressed as:

B.C.1:   at z=0 $C_A=0$

B.C.2:   at x=0 $C_A= C_{A0}$

B.C.3:   at x=∞ $C_A=0$

The concentration profile of CO_2 in the small penetration thickness may be obtained by using $C_A=C_A(x,z).e^{-\beta z}$ transformation, with the boundary conditions. The resulting equation could be given as shown in Eq.(3.2).

$$C_A = C_{A0} \left(1 - erf \frac{x}{4D_{AB} \left(\dfrac{z}{v_{max}} \right)} \right) e^{-\frac{k_2 C_B}{v_{max}} z} \qquad (3.2)$$

It was assumed that OH^- ion concentration is constant during a short contact time between the gas and liquid phases. The dissolution rate of CO_2 in $mol/m^2 s$ in the liquid phase can be given as Eq.(3.3):

$$N_A = -D_{AB} \frac{\partial C_A}{\partial x} \bigg|_{x=0} = C_{A0} \sqrt{\frac{D_{AB} v_{max}}{\pi z}} e^{-\frac{k_2 C_B}{v_{max}} z} \qquad (3.3)$$

The average dissolution rate of CO_2 dissolved in the liquid phase in mol/s can be expressed as:

$$R_A = \int_0^W \int_0^L N_{Ax}\Big|_{x=0} dzdy = WLC_{A0}\sqrt{\frac{4D_{AB}v_{\max}}{\pi L}}\; e^{-\frac{k_2 C_B L}{v_{\max}}}\; f\big(C_B, L\big) \qquad (3.4)$$

Here, our purpose was neither to solve the given equation, nor determine the concentration profiles in the solution. All we need was to figure out the main effective parameters affecting the CO_2 transfer rate, and how we could control the CO_2's dissolution. According to Eq.(3.4), the dissolution rate is significantly related to the surface area of liquid phase, A, OH^- ion concentration in the liquid phase, C_B, maximum velocity of the liquid phase, $v_{\max}$, and the length of the contact area between liquid and gas phases, L. It is assumed that the diffusion coefficient, D_{AB}, reaction rate constant between CO_2 and OH^- ions, k_2, the CO_2 solubility, and C_{A0} are constant. Here, $f(C_B,L)$ is related to C_B concentration and length of the gas-liquid contact area, similar to the enhancement factor.

In the proposed method, it was assumed that small penetration thickness is so small enough for the direct reaction between Ca^{++} and OH^- ions, $Ca(OH)_2$ flow through the reaction chamber is in cylindrical form. Therefore, the kinetic expression of cylindrical form was taken as the same with the Cartesian coordinates.

3.2.3. Small Penetration Method

Unless otherwise indicated, the $CaCO_3$ precipitation experiments were conducted in the experimental set-up as shown in Figure 3.2a under standard experiment condition as given in Table 3.1.

The only aim of experimental set-up of small penetration method is to control the CO_2 diffusion from gas phase to liquid phase, not to measure the parameters such as concentration profile and diffusion rate. Figure 3.2b shows the CO_2 diffusion profile in the liquid phase. CO_2 diffusion from gas phase to liquid phase may be controlled by using small penetration set-up. Here, crystallization and stabilization sections were also separated from each other.

Figure 3.2a shows the experimental set-up according to the small penetration method developed. The experimental set-up consist of a reaction chamber attached to CO_2 tank with a flow controller (AALBORG), and a stabilization tank containing a magnetic stirrer, pH and conductivity probes (Orion). N_2 was fed on the surface of the

Ca(OH)$_2$ solution in stabilization tank to maintain CO$_2$ introduction to the stabilization tank. Before the experiments, pH, and conductivity probes were calibrated with calibration solutions. Before crystallization, the dissolution of Ca(OH)$_2$ was allowed to be completed. The Ca(OH)$_2$ solution prepared in the stabilization tank was circulated between the stabilization tank and the reaction chamber by a pump. The pH and conductivity values were monitored during crystallization.
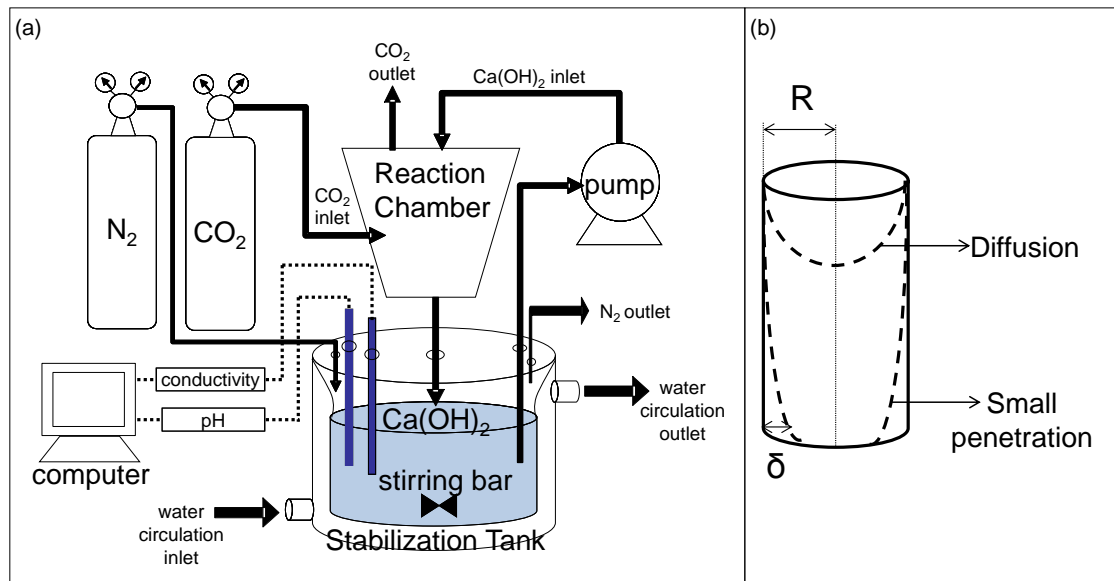
Figure 3.2. Experimental set-up for the production of nano calcite by small penetration method.

In standard experiment condition of small penetration method, a 1.0003 g of Ca(OH)$_2$ solution was added into 900 ml of ultrapure water (Millipore Elix-5/Milli-Q water treatment unit) to prepare 15 mM Ca(OH)$_2$ solution in 5-neck jacketed reactor (stabilization tank). 15 mM Ca(OH)$_2$ solution was stirred at 600 rpm during Ca(OH)$_2$ dissolution. The solution was fed into the reaction chamber by a pump at a flow rate of 13.31 ml/s (Aalborg Model V single flow tube meter). The temperature was kept constant at 23 $^{\circ}$C (Wise Circu Water Bath). The flow rate of N$_2$ injected on the surface of Ca(OH)$_2$ solution in stabilization tank was arranged to a constant value at 1.0 L/min (Aalborg Model P single flow tube meter). The CO$_2$ was continuously injected into the reaction chamber at a flow rate of 4.27 ml/s (Aalborg Model P single flow tube meter). A 6.5 mm of the inner pipe diameter of 15 mM Ca(OH)$_2$ was selected for the recirculation of Ca(OH)$_2$ solution. The length of reaction chamber was 30 cm. 15 mM

Ca(OH)$_2$ solution was recirculated by a pump into stabilization tank after a short contact time between the CO$_2$ gas and 15 mM Ca(OH)$_2$ solution.

Table 3.1. Standard experiment conditions for small penetration method.

Parameter	Value
Stirring rate	600 rpm
Flow rate of Ca(OH)$_2$	13.31 ml/s
Flow rate of CO$_2$	4.27 ml/s
Ca(OH)$_2$ concentration	15 mM
Stabilization tank volume	900 ml
Feeding pipe inner diameter of Ca(OH)$_2$	6.5 mm
Length of reaction chamber	30 cm
Ca(OH)$_2$ purity	96%, unfiltered
CO$_2$ percentage	99.99%
Temperature	23°C

The pH and conductivity values were monitored with a pH probe (Orion) and a conductivity cell (Orion), both attached to a Thermo Orion 5-Star pH meter. All data were recorded online by a 5 Star Navigator software program before and during CaCO$_3$ precipitation experiments. CaCO$_3$ synthesis was ended when the pH was 7.

2 ml of samples were withdrawn from stabilization tank for the determination of zeta potential, particle size distribution and average particle size measurements. Another 2 ml of samples were also withdrawn from stabilization tank, placed into eppendorf tubes at specified conductivity values, and, centrifuged for 20 min at 9000 rpm for SEM imaging. 50 ml of samples collected from stabilization tank were withdrawn in a 50 ml falcon tubes and centrifuged for 20 min at 9000 rpm and centrifuged for 20 min at 9000 rpm to perform XRD analysis at certain conductivity values. The precipitated samples obtained for XRD and SEM analysis were collected, and washed by acetone. Precipitates collected for SEM imaging were dried in an oven under vacuum condition at 85°C and samples for XRD analysis were dried in an oven at 105°C over night before characterization. Precipitates were characterized by Scanning Electron Microscopy and X-ray diffraction.

50 ml of samples was collected from the reaction chamber outlet at different conductivity values during precipitation to compare the difference in pH and

conductivity between stabilization tank and reaction chamber outlet. Then, 50 ml of solution was returned into the stabilization tank after the measurements.

In order to obtain the BET surface area of $CaCO_3$ particles produced by the small penetration method, 50 ml of samples obtained at various conductivity values was withdrawn from the stabilization tank, and centrifuged for 20 min at 9000 rpm. The precipitates were collected, and washed by acetone. Precipitates obtained from 50 ml falcon tubes were dried in an oven at $105^{o}C$ over night before characterization.

In order to obtain the conversion of $Ca(OH)_2$ to $CaCO_3$ over the reaction, 50 ml of samples were collected from stabilization tank at selected conductivity values. 7 different Teflon filter papers with a 200 nm pore size were washed by ultrapure water, dried in an oven at $90^{o}C$, and weighted. Then, filter papers were again washed by ultrapure water, dried and weighted. The same procedure was repeated three times to understand the error in the measurement. When the error was found to be about 0.1%, 50 ml of samples collected from stabilization tank at selected conductivity values were poured into the vacuum filtration unit, and then, filter papers were dried in an oven under vacuum at $90^{o}C$ overnight. All filter papers were weighted, and the conversion of $Ca(OH)_2$ to $CaCO_3$ was calculated at different conductivity values.

3.2.4. CO_2 Pulsation in the Small Penetration Method

Crystallization was studied by a pulse injection of the CO_2 into the reaction chamber for a certain time interval and stopped for other certain time intervals. The development stage of the crystallization and the late stage of the crystallization were investigated under standard conditions as shown in Table 3.1. A 600 ml of tank volume and 5.2 ml/s of $Ca(OH)_2$ flow rate were selected. Samples were collected at each pulse interval and analyzed for zeta potential, particle size and morphology.

3.2.5. Parametric Studies

The CO_2 dissolution was proposed to be one of the important factors to obtain nano sized and monodisperse $CaCO_3$ particles. The developed small penetration method was employed to control the CO_2 dissolution rate by employing various parameters as indicated in Eq.(3.4). These parameters could be related to the surface area of liquid

phase (A), OH$^-$ ion concentration in the liquid phase (C_B), maximum velocity of the liquid phase (v_{max}), and the length between liquid and gas phases (L). Therefore, $Ca(OH)_2$ flow rate, CO_2 flow rate, stirring rates in the stabilization tank, $Ca(OH)_2$ concentration, stabilization tank volume, pipe inner diameter for liquid phase $Ca(OH)_2$ solution, length of the reaction chamber, $Ca(OH)_2$ purity, and CO_2 percentage were chosen to be the main parameters which can directly affect the CO_2 dissolution rates.

Experiments were performed under standard conditions as shown in Table 3.1. Effects of different parameters on the particle size were investigated by altering only the related parameter in the small penetration method. pH and conductivity values for each parametric experiments were monitored. The consumption rates of $[Ca^{++}]$ and $[OH^-]$ ions were determined for different parametric experiments by using three interval data of $[Ca^{++}]$ and $[OH^-]$ concentrations over time.

3.2.6. Sample Characterization

3.2.6.1. Particle Size Distribution and Average Particle Diameter

Particle size distribution and average particle diameter from each sample collected during the experiments were determined by using dynamic light scattering (DLS) technique with a Malvern Nano Zetasizer. Samples were withdrawn into a disposable cuvette without any dilution. Particle sizes from a maximum size range of 3 nm to 10 μm were analyzed by the software controlled program.

3.2.6.2. Zeta Potential Analysis

Zeta potential measurements were analyzed by Malvern Nano ZS Instrument. Sample was placed into the zeta potential measurement cuvette and software controlled measurement was chosen to measure the zeta potential. Dispersed particles in the solution were mobilized with a velocity by applying an electric field, which was related to their zeta potential. Phase analysis Light Scattering technique was used for the measurement of the velocity and enabled the electrophoretic mobility calculation. Finally, zeta potential and potential distribution were measured.

3.2.6.3. BET Surface Area Analysis

BET surface area measurements were performed by Micromeritics Gemini V adsorption apparatus with a decreasing at 100 ^{o}C for 24 hours. The surface area of $CaCO_3$ particles were measured by N_2 adsorption technique in the liquid nitrogen at 77 K.

3.2.6.4. Scanning Electron Microscope (SEM) Analysis

The morphologies of the precipitated $CaCO_3$ crystals were analyzed by Scanning Electron Microscope provided by Philips XL 30S FEG. After SEM viewing, the $CaCO_3$ powders obtained at the end of the drying process for each experiment were coated with gold. Then, the samples were mounted on copper sample stubs with conducting carbon tape for the SEM imaging, operated at an accelerating voltage of 15 kV.

3.2.6.5. X-Ray Diffraction (XRD) Analysis

X-Ray Diffraction measurements were analyzed by Philips X'Pert Pro X-Ray Diffractometer conducted on computer program. Cu Ka radiation equipped with a diffracted beam monochromator accelerating detector was performed on the fine $CaCO_3$ powders packed into a zero background sample holder at 45 kV and 40 mA. The amount of powder used in the XRD analysis is only related to intensity and can be varied. Step scan of 2θ was 0.0334^{o} and counting step was 10.16 sec. The diffraction pattern was determined from 10° to 80° for 2θ. Search Match Computerized Technique was also used for the identification of $CaCO_3$ crystals in a mix. XRD reference peaks for different polymorphs and/or forms were given in Figure 3.3 for information .
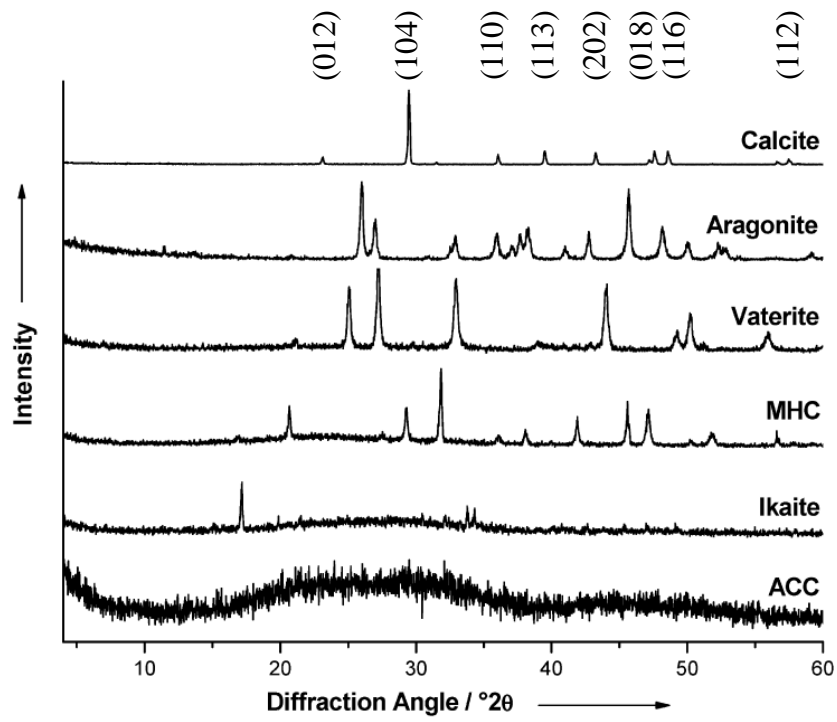
Figure 3.3. XRD patters of different CaCO$_3$ forms on JCPDS (MHC: monohydrocalcite, ACC: Amorphous CaCO$_3$) (Nebel, Neumann, Mayer, & Epple, 2008).

CHAPTER 4

RESULTS AND DISCUSSIONS

4.1. Stability of $CaCO_3$ in $Ca(OH)_2$

The ions (Ca^{++}, OH^-, CO_3^{2-}, HCO_3^- etc.) and the electrical charges on the clusters and on the growing $CaCO_3$ particles can be different at different pH values. Especially, the sharp decrease in the pH at about zero conductivity may be associated with the consumption of some ions. Chibowski et al., (2003) stated that the positive net charge on the $CaCO_3$ surface can be obtained as a result of the surface $-Ca^+$ sites (E Chibowski, Hotysz, & Szcześ, 2003a). Moreover, the excess Ca^{++} ions may increase the zeta potential and solve the aggregation problem in small penetration method. Therefore, monodisperse calcite particle can be obtained by the stability of $CaCO_3$ in $Ca(OH)_2$ solution and/or slurry.

The particle size and zeta potential for commercial $Ca(OH)_2$ and $CaCO_3$ were measured. Initially, small amount of both commercial $CaCO_3$ and $Ca(OH)_2$ were dissolved in ultrapure water. The pH and conductivity of these solutions, zeta potential, and average particle size were estimated. Additional powders were added into each solution, samples were withdrawn for each step in order to estimate particle size, zeta potential, and SEM images.

Dissolution of commercial $CaCO_3$ in 10 mM $Ca(OH)_2$ solution, and dissolution of $Ca(OH)_2$ in 10 mM of $CaCO_3$ slurry were also studied.

Figure 4.1 shows the pH and conductivity values in the presence of stepwise $Ca(OH)_2$ addition into ultrapure water. As shown in figure, the pH and conductivity values increased when $Ca(OH)_2$ was added into the ultrapure water up to saturation point of about 20 mM for $Ca(OH)_2$, then, stabilized upon further addition of the $Ca(OH)_2$ amount.
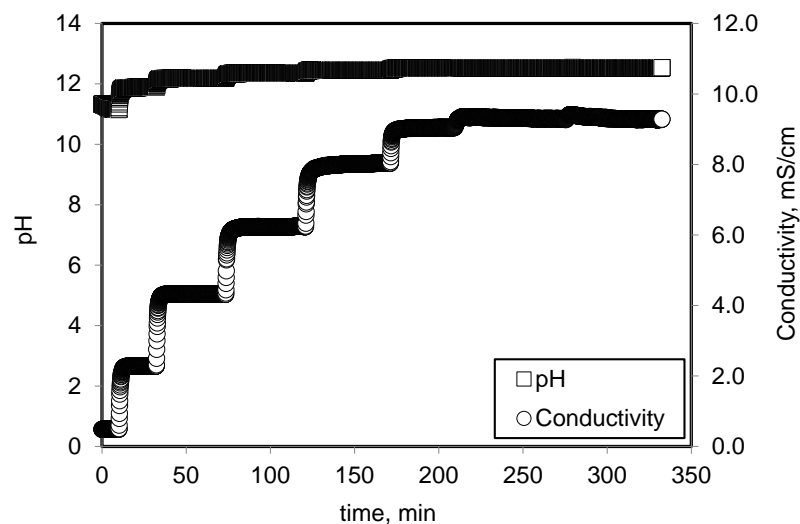
Figure 4.1. Change of pH and conductivity in the presence of various Ca(OH)$_2$ addition.

The zeta potential and average particle size in Ca(OH)$_2$ solution was shown in Figure 4.2. As mentioned before, the Ca(OH)$_2$ used in the experiments was purchased from Merck with a purity of 96%. A 3% of the impurity was CaCO$_3$, and 1% was the other impurities. Therefore, there was a small amount of CaCO$_3$ in Ca(OH)$_2$ solution. As shown in figure, the zeta potential increased gradually up to saturation point upon the addition of Ca(OH)$_2$ into ultrapure water. After the peak point, zeta potential decreased back from a value of 40 mV to about 25 mV at higher Ca(OH)$_2$ concentrations where Ca(OH)$_2$ was formed a slurry. Chibowski et al., (2003) stated that the positive net charge on the CaCO$_3$ surface could be obtained as a result of the surface –Ca$^+$ sites (E Chibowski et al., 2003a). They indicated that zeta potential of precipitated CaCO$_3$ from equimolar concentration of Ca^{++} and CO$_3^{2-}$ was around zero or, small positive. The zeta potential of CaCO$_3$ precipitated from excess of CO$_3^{2-}$ was negative, and the zeta potential of CaCO$_3$ precipitated from excess of Ca^{++} was positive. The Ca^{++} ion concentration increased up to the saturation point. Ca^{++} ion concentration did not change although the amount was increased. Therefore, the decrease in the zeta potential could be related to the increase in the undissolved CaCO$_3$ particles in the solution. The average particle size measured from 1 mM to 20 mM Ca(OH)$_2$ addition was found to be nearly the same at about 300 nm. When the concentration was higher than 20 mM, the average particle size were measured significantly higher upon addition of the Ca(OH)$_2$ powder for which the Ca(OH)$_2$ could not be dissolved above its saturation limit. Therefore, the increase in the average particle size at concentration above 20 mM could be due to the undissolved particles in the solution.

36
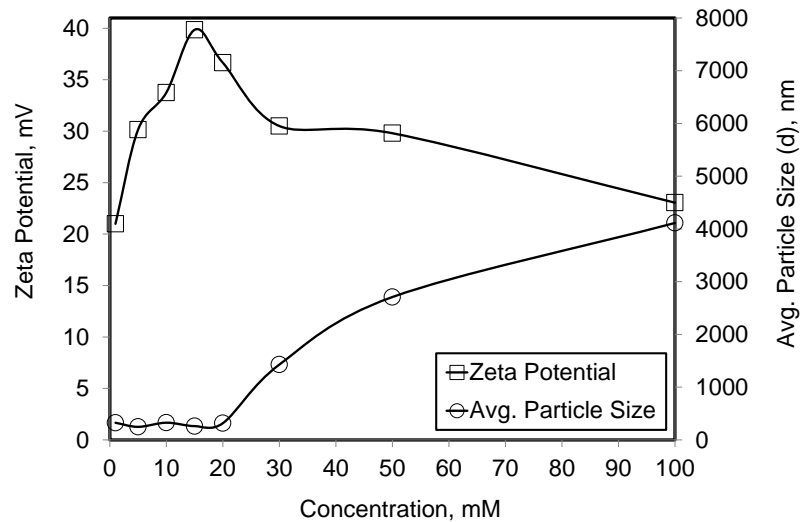
Figure 4.2. Zeta potential and average particle size value obtained by different $Ca(OH)_2$ addition.

Figure 4.3 shows the pH and conductivity values in the presence of various $CaCO_3$ addition into the ultrapure water. Perry et al., (1984) stated that the dissolution of $CaCO_3$ was about between the values of 1.2×10^{-5} kg/kg and 1.4×10^{-5} kg/kg, which are very low comparing to the $Ca(OH)_2$ dissolution limit (Perry, Green, & Maloney, 1984). As seen in the figure, while pH was almost stable, the conductivity values were slightly increased at each addition of $CaCO_3$ in the solution indicating that slight formation of charged clustered particles could form.
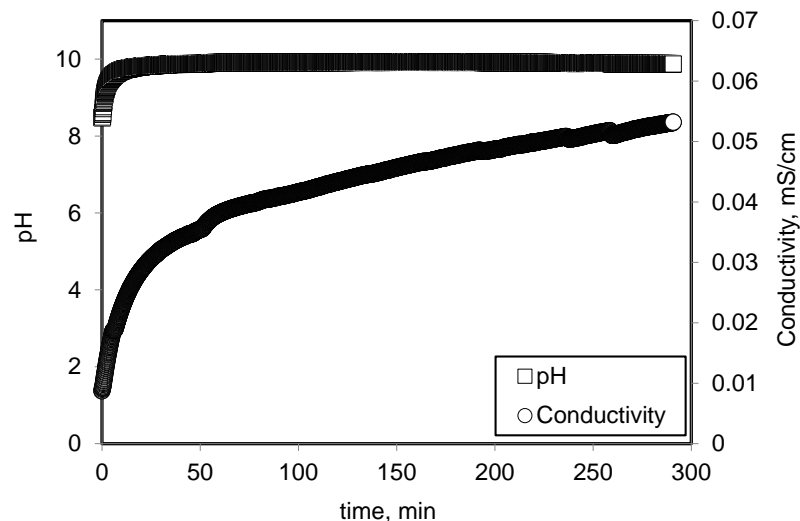
Figure 4.3. pH and conductivity values obtained by various $CaCO_3$ addition.

Figure 4.4 shows the zeta potential and average particle size values in the presence of various addition of $CaCO_3$. As shown in the figure, zeta potential was about

-10 mV and the average particle size was about 4 μm. Upon further addition of CaCO$_3$ did not affect much for the zeta potential and indicated about 5 μm of particles in the solution. Here, the zeta potential was found to be negative for all CaCO$_3$ concentrations. pH of CaCO$_3$ solution was about 9.93. Fenter et al., (2000) reported that the CaCO$_3$ surfaces are covered by water molecule and become positively charged (Fenter et al., 2000). Although the solubility of CaCO$_3$ was low, Ca^{++} and CO$_3^{2-}$ ions were obtained when the CaCO$_3$ particles were dissolved. At high pH, Ca^{++} and OH$^-$ may form complexes resulting in CO$_3^{2-}$ buffer and a net negative charge on the surface of CaCO$_3$ particles.
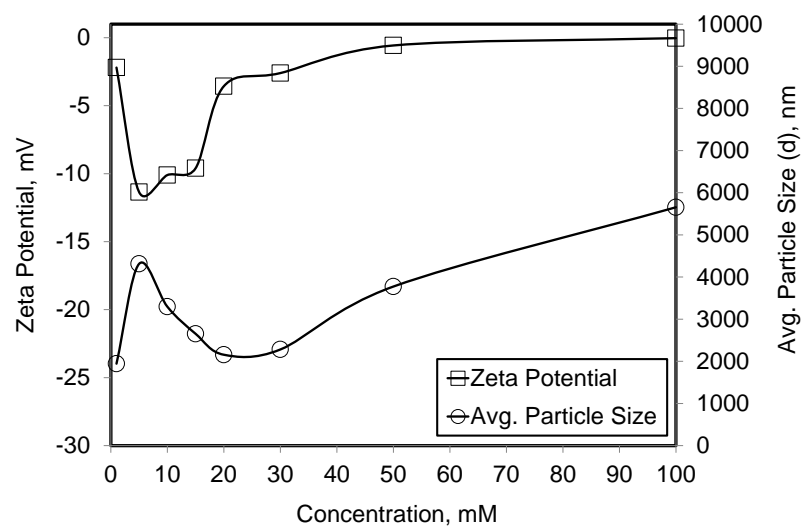
Figure 4.4. Change of zeta potential and average particle size in the presence of various CaCO$_3$ addition.

Figure 4.5 shows pH and conductivity values during the addition of Ca(OH)$_2$ powder into a 10 mM of CaCO$_3$ slurry. As shown in the figure, pH and conductivity values were increased with the addition of various amount of Ca(OH)$_2$.
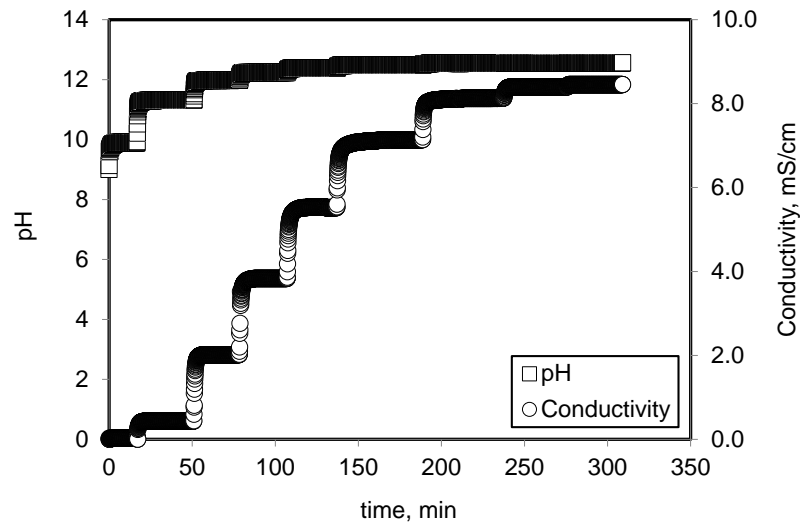
Figure 4.5. Change of pH and conductivity in the presence of various Ca(OH)$_2$ addition into 10 mM CaCO$_3$.

Figure 4.6 shows zeta potential and average particle size during Ca(OH)$_2$ addition into 10 mM Ca(OH)$_2$. As shown in the figure, zeta potential of 10 mM CaCO$_3$ was found to be about -2 mV. The zeta potential increased to 35 mV upon addition of Ca(OH)$_2$. The Ca^{++} and OH$^-$ ion concentration increased when different amount of Ca(OH)$_2$ was dissolved in 10 mM CaCO$_3$ slurry. The negatively charged surface of 10 mM CaCO$_3$ slurry became positively charged when Ca^{++} ions adhered to the surface of CaCO$_3$ particles when Ca(OH)$_2$ was added into 10 mM CaCO$_3$ slurry. Therefore, the zeta potential of CaCO$_3$ particles increased from -2 to 39 mV indicating that the stability of CaCO$_3$ particles could be achieved upon the addition of Ca(OH)$_2$. On the other hand, the particle size for the 10 mM slurry was about 4 μm and it was decreased to about 300 nm upon addition of Ca(OH)$_2$. Above the saturation limit for the Ca(OH)$_2$, the particles size started to increase because there seems to be undissolved Ca(OH)$_2$ particles in the system.
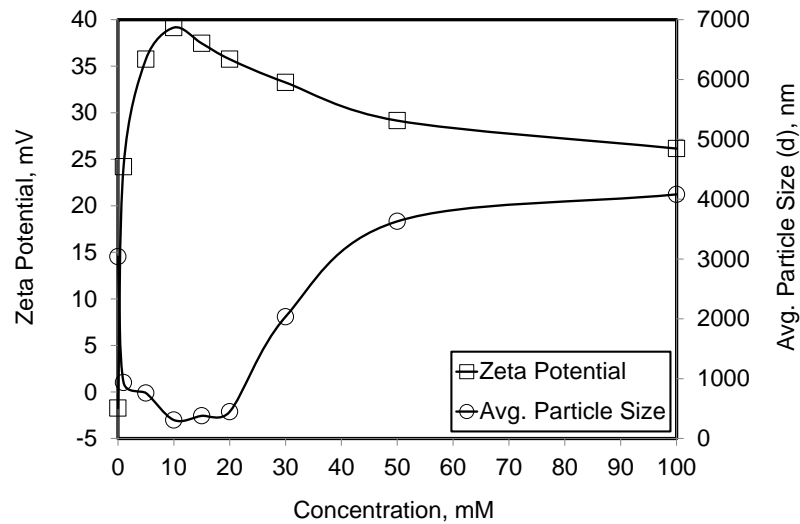
Figure 4.6. Change of zeta potential and average particle size in the presence of various Ca(OH)$_2$ addition into 10 mM CaCO$_3$.

Samples were taken from suspensions during each addition of Ca(OH)$_2$ in 10 mM of CaCO$_3$ suspension. Figure 4.7 shows their SEM images. As shown in the figure, the particle sizes are about 6 μm for CaCO$_3$ suspension. Upon addition of Ca(OH)$_2$, it was expected that Ca(OH)$_2$ was fully dissolved at concentrations lower than 20 mM. There is clear evidence that some new particles were formed and precipitated on the surface of the CaCO$_3$ particles. Also, the surface of the CaCO$_3$ particles were seen to be deformed or eroded in the presence of Ca(OH)$_2$. Thus, it can be argued that the zeta potential of CaCO$_3$ particles in the presence of Ca(OH)$_2$ is positively charged. On the other hand, the settling velocity is proportional to particle size. Bigger particles were expected to settle faster than smaller particles. Especially, 5 μm of CaCO$_3$ particles will settle during particle size measurement (Molva, 2011), and the rest in the solution would be newly synthesized smaller particles. During particle size distribution and average particle size analysis performed by the DLS technique, these particles cannot settled completely, however, coagulation would affect the size measurement adversely. Therefore, the inconsequence between SEM images and average particle size obtained by DLS technique could be related to the settling of large particles. The smaller particles may be measured by DLS technique for the zeta potential and average particle sizes.
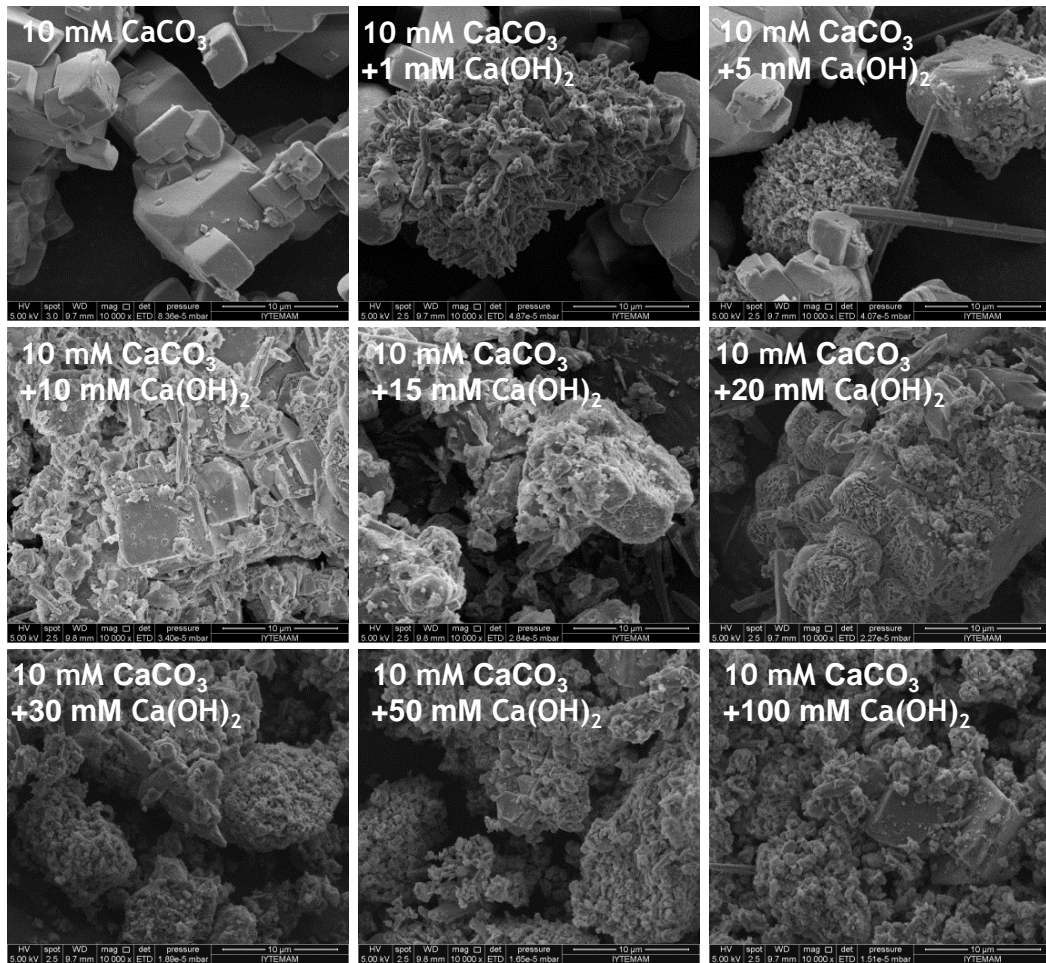
Figure 4.7. SEM images of particles during Ca(OH)$_2$ powder addition into a 10 mM CaCO$_3$ slurry (Scale: 10 μm).

Similarly, CaCO$_3$ powder was also added into 10 mM of Ca(OH)$_2$ solution. Figure 4.8 shows pH and conductivity values during the addition of CaCO$_3$ powder into the Ca(OH)$_2$ solution. The change in pH and conductivity values was not significant when CaCO$_3$ powder was added.
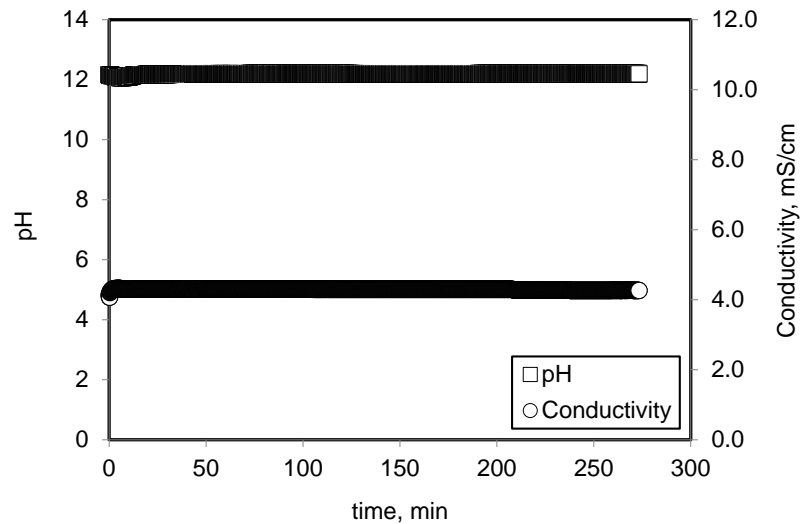
Figure 4.8. pH and conductivity values during $CaCO_3$ addition into 10 mM $Ca(OH)_2$.

Figure 4.9 shows the zeta potential and average particle size measured when $CaCO_3$ particles were added into a 10 mM $Ca(OH)_2$ solution. As shown in the figure, zeta potential values were almost constant or slightly decreased upon addition of $CaCO_3$. The particle size almost did not change. However, at concentration higher than 20 mM, both zeta potential and average particle size slightly increased. However, the particle sizes were measured still less than 1 μm.
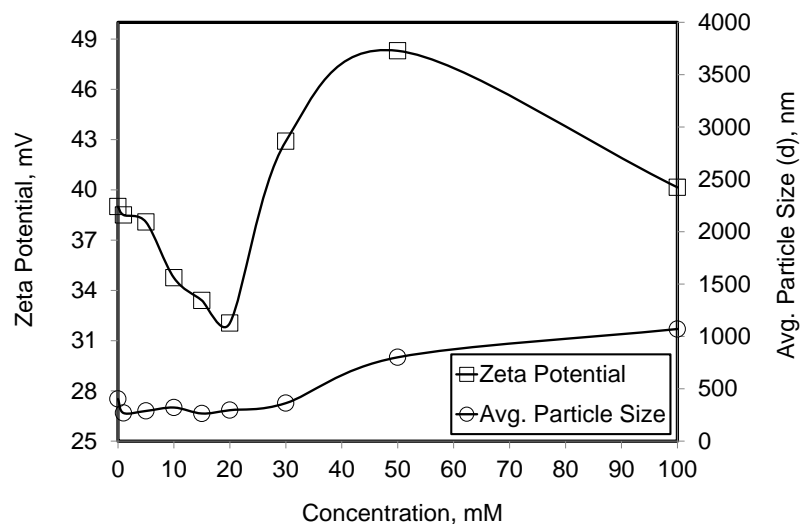
Figure 4.9. Zeta potential and average particle size values during addition of $CaCO_3$ into a 10 mM $Ca(OH)_2$ solution.

SEM images of particles during the addition of commercial $CaCO_3$ powder into 10 mM of $Ca(OH)_2$ solution were shown in Figure 4.10. As shown in the figure, particles obtained from 10 mM of $Ca(OH)_2$ solution look like highly aggregated nano

particles. It was expected that $Ca(OH)_2$ in 10 mM concentration must be fully dissolved. Considering a 3% of $CaCO_3$ as the impurity in $Ca(OH)_2$ powder, it may be assumed that nano particles would be produced in the presence of $Ca(OH)_2$ and $CaCO_3$, for which Ca^{++} ions mostly come from $Ca(OH)_2$ and CO_3^{2-} ions came from $CaCO_3$. Thus, what were measured during zeta potential and particle sizes were probably these newly produced particles in the solution.
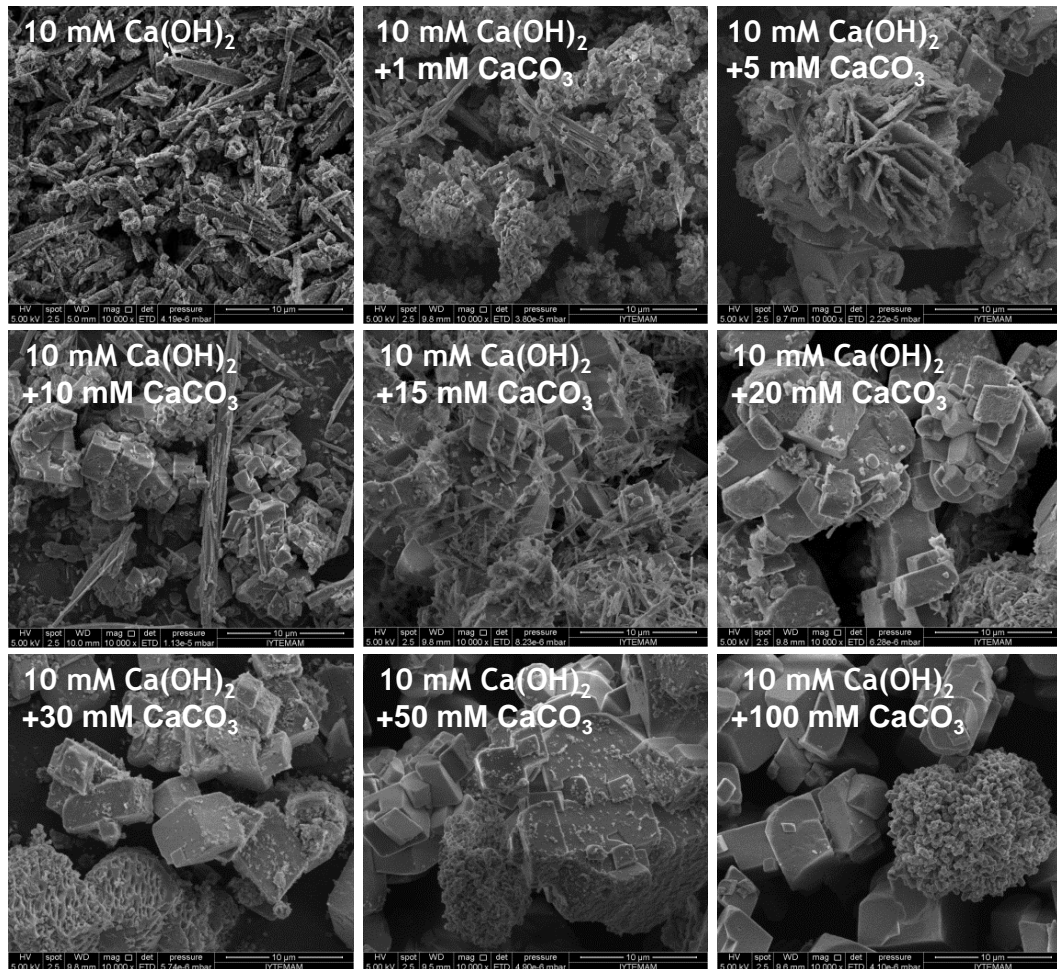
Figure 4.10. SEM images of various $CaCO_3$ addition into 10 mM $Ca(OH)_2$ (Scale: 10 μm).

The conductivity values were measured for different concentration of $Ca(OH)_2$ and $CaCO_3$ (from 1 to 100 mM) in ultrapure water and plotted as shown in Figure 4.11. The equilibrium conductivity values for $Ca(OH)_2$ reported by Burns et al., (2005) (Burns & Jachuck, 2005) were also included in Figure 4.11 for different $Ca(OH)_2$ concentrations. As shown in the figure, the conductivity values obtained were in good agreement with Burns' data. As shown in the figure, the linear increase in conductivity

values could be related to the increase in Ca(OH)$_2$ concentration up to the saturation limit. After the saturation limit, the conductivity values did not change with the addition of Ca(OH)$_2$. Burns et al., (2005) (Burns & Jachuck, 2005) stated that the conductivity values deviated 24% from the theoretical values. This difference may explain the complexation formation between Ca^{++}, OH$^-$, and CO$_3^{2-}$ ions in the solution below the solubility limit. Above the solubility limit, beside complexation between ions, considerable amount of Ca(OH)$_2$ probably remained undissolved in ultrapure water.
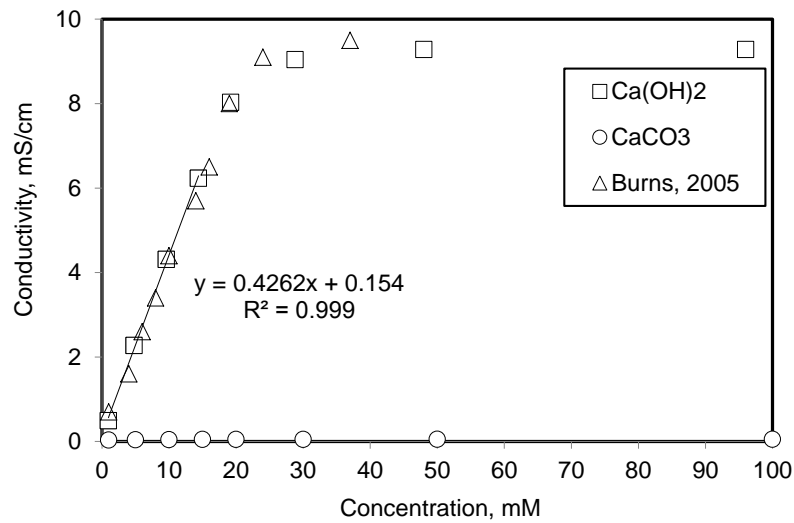
Figure 4.11. Conductivity values for Ca(OH)$_2$ and CaCO$_3$.

The Ca^{++} ion concentration could be related to the linear change of conductivity by the Ca(OH)$_2$ concentration up to the solubility limit. The Ca^{++} ion concentration in the Ca(OH)$_2$ solution can be estimated by Eq. (4.1).

$$\left[Ca^{++} \right] = Conductivity \times \frac{1}{slope} \tag{4.1}$$

The OH$^-$ ion concentration can be calculated from the pH values as given in Eq.(4.2).

$$\left[OH^- \right] = 10^{\left(-(14 - pH) \right)} \tag{4.2}$$

The [Ca^{++}] and [OH$^-$] ion concentrations, calculated from Eq.(4.1) and Eq.(4.2), respectively, were shown in Figure 4.12 during the addition of Ca(OH)$_2$. Theoretically,

44

15 mM Ca^{++} and 30 mM OH^- ion concentrations would be obtained when 15 mM $Ca(OH)_2$ was dissolved in ultrapure water. However, much of the $Ca(OH)_2$ powder was left undissolved as depicted also by Burns et al., (2005) (Burns & Jachuck, 2005). Therefore, the concentration of $[Ca^{++}]$ and $[OH^-]$ ions were smaller than the theoretical values as shown in the figure. Moreover, the OH^- ion concentration would be two times bigger than the Ca^{++} ion concentration. As shown in the figure, the OH^- ion concentration was not bigger than Ca^{++} ion concentration indicating that clustering of OH^- ions would occur in solution. As understood from these data that clustering may affect nano $CaCO_3$ production.
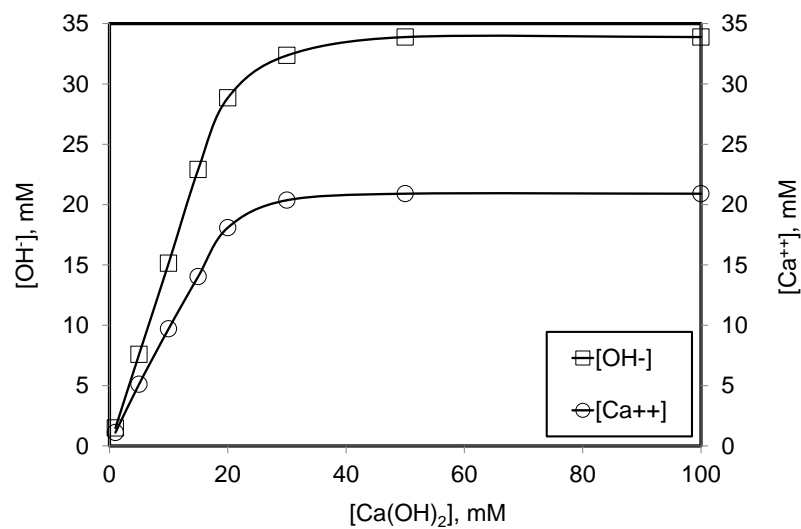
Figure 4.12. Calculated OH^- and Ca^{++} ion concentrations in $Ca(OH)_2$ solution.

4.2. Small Penetration Method

In small penetration method, crystallization section and stabilization section were separated from each other. As shown in Figure 4.13, the reaction between Ca^{++} and CO_3^{-2} ions was performed in the reaction chamber, and stabilization of produced $CaCO_3$ particles was achieved in the stabilization tank. Therefore, there may be a difference in pH and conductivity values between reaction chamber outlet and stabilization tank. As shown in Figure 4.13a, dissolution of $Ca(OH)_2$ was achieved in between -5 and 0 min in the stabilization tank. The conductivity and pH values were almost constant when $Ca(OH)_2$ powders were dissolved in the ultrapure water. The CO_2 was shown to be injected into the reaction chamber at 0 min. There were four conductivity regions in carbonation process. Figure 4.13a shows the pH and

45

conductivity values for the stabilization tank and the reaction chamber outlet. As shown in the figure, the pH and conductivity values for reaction chamber was found to be smaller than the pH and conductivity values for the stabilization tank up to near zero conductivity. After near zero conductivity, the pH and conductivity values for reaction chamber were higher. The increase in the conductivity for both stabilization tank and reaction chamber beyond zero conductivity could be related to the increase in charged species due to the CO_2 dissolution as well as Ca^{++} ions as a result of the redissolution of $CaCO_3$. These results indicate that the penetration of CO_2 into $Ca(OH)_2$ solution could only occur within small penetration depth rather than neutralizing the whole bulk liquid. Therefore, small penetration method is applicable for the production of nano calcite.

Figure 4.13b presents the calculated Ca^{++} and OH^- ions concentration in the stabilization tank and reaction chamber. As shown in the figure, the CO_2 injected into the reaction chamber cannot completely consume the Ca^{++} and OH^- ions fed into the reaction chamber indicating that CO_2 was penetrated up to the small penetration thickness as proposed. Therefore, it may be argued that there was only a small $Ca(OH)_2$ conversion takes place into $CaCO_3$ through the reaction chamber.

The consumption rate of Ca^{++} and OH^- ion concentrations obtained from Figure 4.13b was shown in Figure 4.14. The consumption rate of Ca^{++} and OH^- ions concentrations sharply increased when CO_2 was fed into the reaction chamber. Then, the consumption rates slightly decreased with the decrease in the Ca^{++} and OH^- ion concentrations. The consumption rate of OH^- ion concentration was expected to be 2 times higher than that for the Ca^{++} ion concentration. However, the consumption rate of OH^- ion was not 2 times bigger. Moreover, there appeared some oscillations in the consumption rate of OH^- ion concentration. In addition, the conversion of $Ca(OH)_2$ solution to $CaCO_3$ in the reaction chamber could be related to the CO_2 injection rate into the reaction chamber since the CO_2 dissolution rate decreased with decreasing OH^- ion concentration as shown in Eq.(3.4).
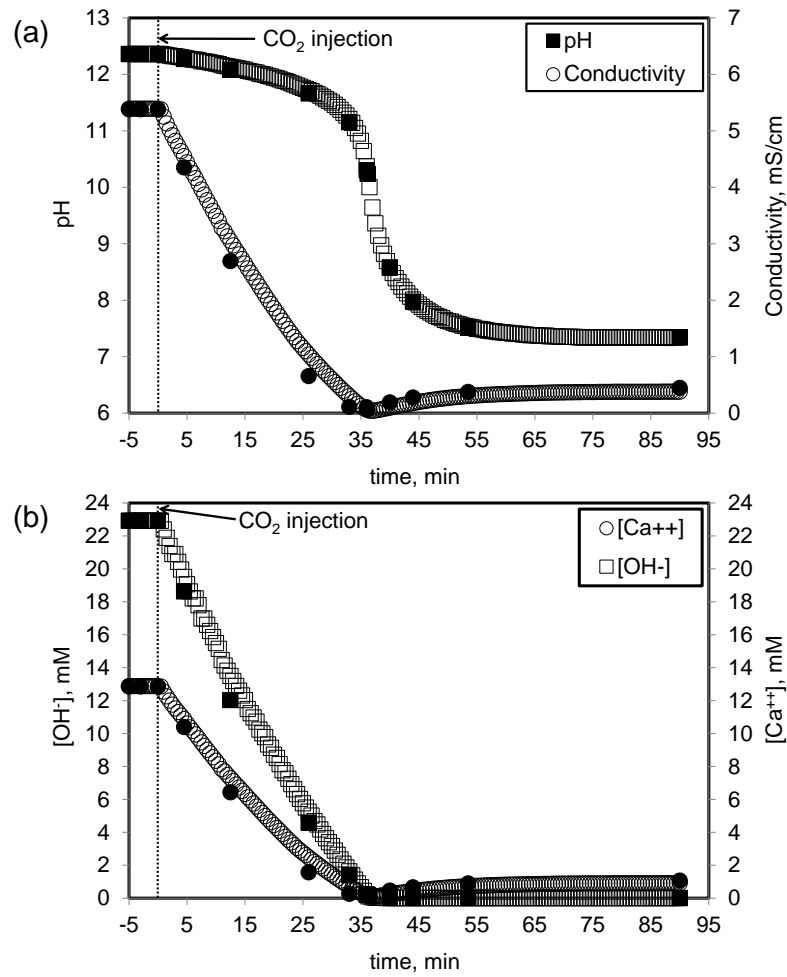
Figure 4.13. (a) pH, and conductivity values, (b) [OH⁻] and [Ca⁺⁺] ion concentration in the stabilization tank and reaction chamber outlets (open symbol: stabilization tank, closed symbol: reaction chamber outlet).
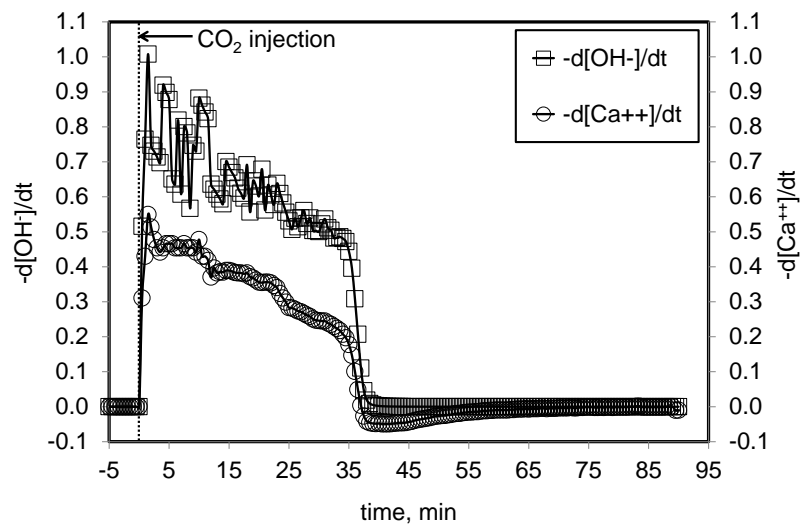
Figure 4.14. Consumption rate of OH⁻ and Ca⁺⁺ ion concentration during crystallization in the stabilization tank.

The particle size distributions of $CaCO_3$ particles obtained from stabilization tank at certain conductivity values were shown in Figure 4.15. The sampling was started before the CO_2 injection. As shown in the figure, the particle size distribution of 15 mM $Ca(OH)_2$ solution had two peaks, which are lied from 100 to 1250 nm, and from 2250 to 6500 nm. Since 15 mM $Ca(OH)_2$ solution used in the experiment was below the solubility limit at 23^oC (Windholz, Budavari, Stroumtsos, & Fretig, 1976), it would have been consisted of only ions and/or ion clusters. Because the $Ca(OH)_2$'s purity was 96% (3% $CaCO_3$ and 1% other impurities), the larger particles would come from the impurity.

It can be shown from the inner figure that the newly produced particle size was about 75 nm to 750 nm and particle size distribution was shifted from left to right as the crystallization progressed.
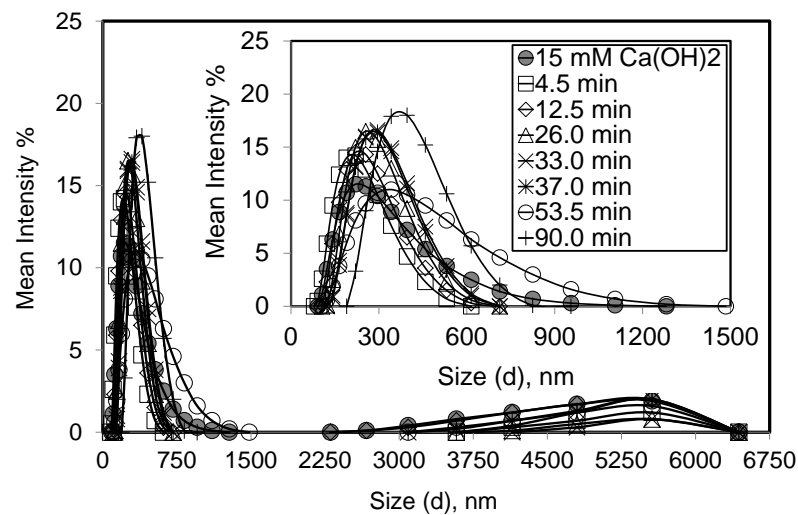
Figure 4.15. Particle size distribution change during crystallization in the stabilization tank.

Figure 4.16 shows the zeta potential and average particle size before and during the $CaCO_3$ crystallization in the stabilization tank. Zeta potential value of 15 mM $Ca(OH)_2$ solution was determined as about 33 mV. Because $Ca(OH)_2$ in 15 mM is fully dissolved, the measured zeta potential could be related to the impurities, or the newly synthesized $CaCO_3$ particles at 0 min. There was a sharp increase in zeta potential upon injection of CO_2. It was reported that the surface of $CaCO_3$ particles is negatively charged at higher pH's (10<pH) (Fenter et al., 2000). In our experiment, zeta sizer gave positive values for zeta potential at higher pH's instead of negative values. The

positively charged surface of $CaCO_3$ particles in $Ca(OH)_2$ solution may result in stable $CaCO_3$ particles. When the crystallization progressed, the zeta potential began to decrease slightly with decreasing ion concentrations. After the zeta potential was reached to near zero conductivity, the zeta potential value started slightly to increase.

As shown in the figure, the average particle size decreased sharply upon introducing CO_2 for crystallization. The sharp decrease in average particle size may indicate the newly formed particles with smaller sizes. The average particle diameter obtained at the beginning of the reaction was about 220 nm, and then increased slightly to 450 nm at the end of the crystallization.
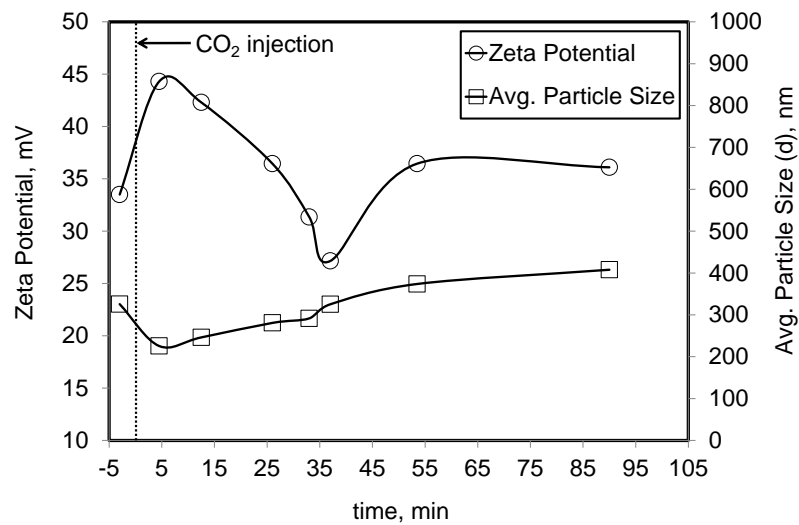
Figure 4.16. Zeta potential and average particle size in the stabilization tank during reaction.

Figure 4.17 shows the SEM images of $CaCO_3$ particles obtained at specified conductivity values. As shown in the figure and evidence from the XRD patterns, shown in Figure 4.19, aragonite (needle-like) and calcite (rhombohedral) particles were obtained at the very early stage of crystallization with sizes of 300 nm. When crystallization progressed, rhombohedral calcite particles were obtained until the conductivity was decreased to 1 mS/cm value. There was no aragonite morphology after the initial stage of crystallization. Hollow calcite particles were formed at the late stage of crystallization. The tendency of hollow structure formation was started from 1.0 mS/cm to 0.30 mS/cm conductivity values, and the numbers of the hollow calcite particles were increased at a conductivity value of about 0.00 mS/cm. It seems that there was some dissolution on the surface of the produced calcite particles at a conductivity

value of about 0.3 mS/cm, and the surface dissolution was significant at conductivity values between 1.0 and 0.3 mS/cm. When pH was started to decrease, the conductivity value started to increase from about 0.00 mS/cm to 0.38 mS/cm. During this step, the number of the hollow particles started to decreased. At low pH, bicarbonate ions (HCO_3^-) started to appear in the solution, therefore, dissolution was discerned among the particles, resulting in filling of the hollow particles to form rhombohedral calcite particles. As a result, rhombohedral calcite particles were obtained at the end of the crystallization in almost monodisperse size distribution with sizes less than 300 nm.
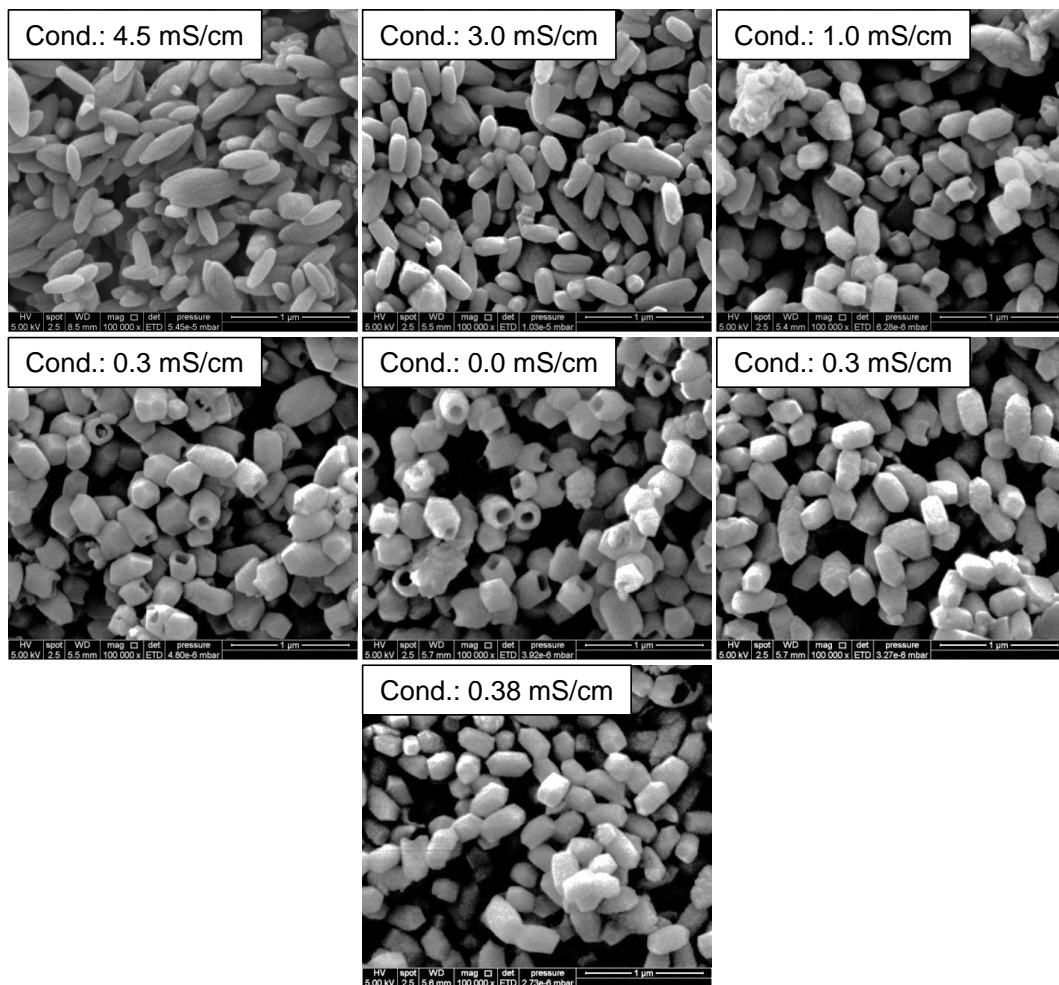
Figure 4.17. SEM images of the precipitates obtained in the stabilization tank by small penetration method at different conductivity values over reaction (Scale: 1 μm).

A possible mechanism for nano calcite production with the proposed small penetration method was shown in Figure 4.18. As shown in the figure, a rice-like $CaCO_3$ particles were synthesized at the very early stage of crystallization. The end

sides of rice seems to be very energetic so that growth is faster at these end sites. When CaCO₃ crystallization progresses, the high energetic end sites started to also dissolve faster. Interestingly, the dissolution was progressed through the inside of the particles resulting in hollow calcite particles. At the very late stages of crystallization, the hollow structure was filled probably due to the dissolution-recrystallization mechanism and a rhombohedral calcite particles were produced.
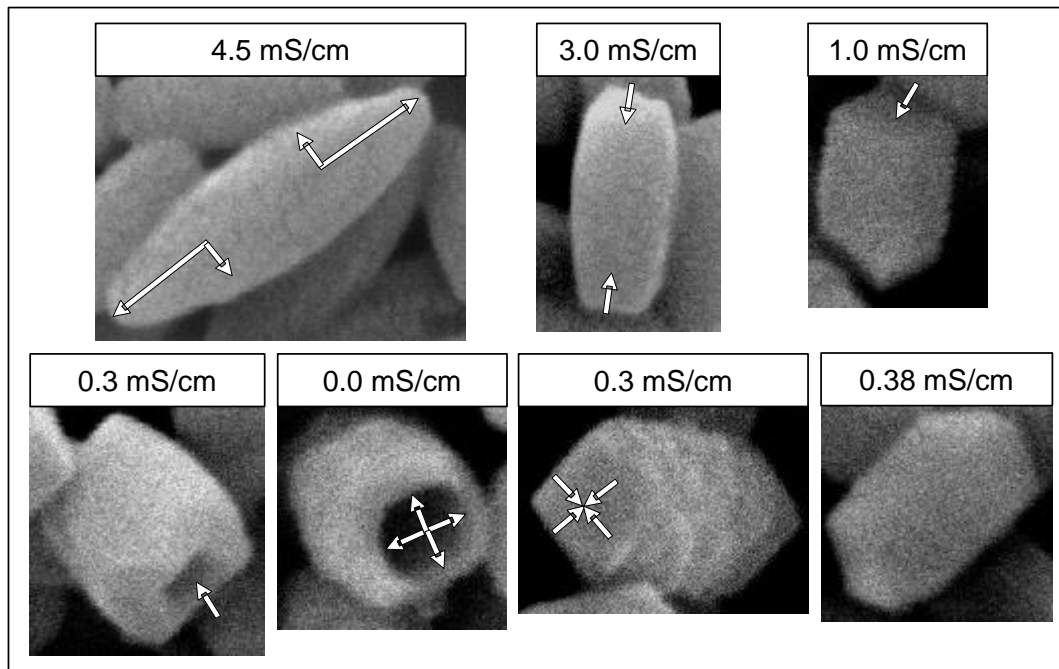
Figure 4.18. A possible mechanism for CaCO₃ crystallization in the proposed small penetration method.

As shown in Figure 4.19, the CaCO₃ crystals obtained at 4.50 mS/cm was indexed to aragonite and calcite. As shown in the figure, all precipitated solids obtained for other specified conductivity values were typical calcite crystals with the same orientation and lattice positions.
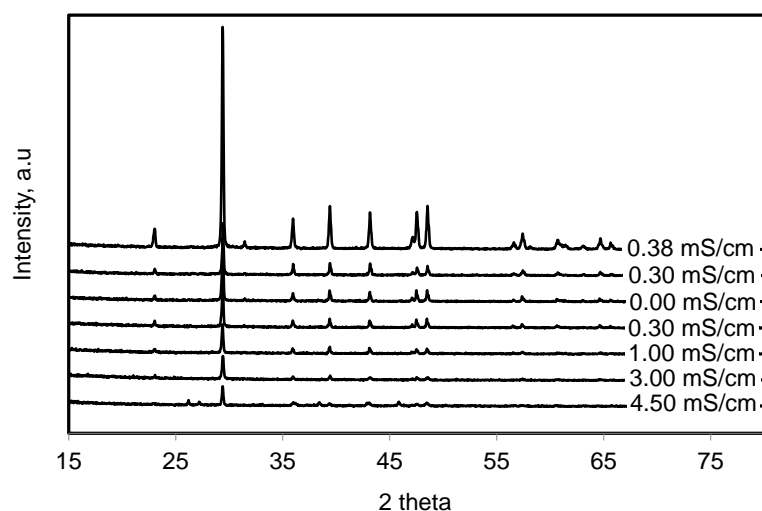
Figure 4.19. XRD patterns of the precipitates obtained in the stabilization tank by small penetration method over reaction.

Figure 4.20 shows the specific surface area of $CaCO_3$ particles obtained at different specified conductivity values through crystallization. At the beginning of the crystallization, the surface area of $CaCO_3$ particles was found to be 11.26 m^2/g. The specific surface area increased and reached the highest value due to the hollow calcite particles at about zero conductivity. Then, the surface area decreased at the very late stage of the crystallization, when the conductivity value was about 0.38 mS/cm. As shown in the figure, the surface area of $CaCO_3$ sharply increased when hollow structures were produced. As shown in the figure, at zero conductivity, BET surface area was found to be 14.75 m^2/g. The surface area decreased sharply when the hollow particles were filled completely. At the end of the crystallization, 12.27 m^2/g of surface area was obtained by the developed small penetration method. Montes-Hernandez et al., reported that nano calcite crystals can be produced with high specific surface area of 6-10 m^2/g by Hydrothermal Carbonation (Montes-Hernandez et al., 2008). Therefore, the surface areas obtained over the reaction by small penetration method were higher than the specific surface area obtained by the Hydrothermal Carbonation. The BET surface area shown in the figure demonstrates that nano calcite crystals with high specific surface area can be produced by the developed small penetration method, with a high potential for the industrial applications.
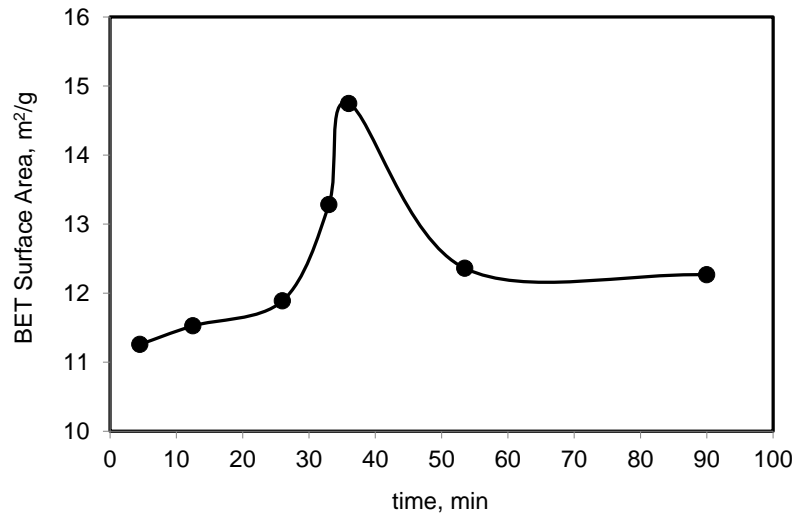
Figure 4.20. Change of surface areas of $CaCO_3$ particles produced in the stabilization tank by small penetration method over reaction.

The conversion over the crystallization in the developed small penetration method was determined. As shown in Figure 4.21, at the initial stage of crystallization, conversion of $Ca(OH)_2$ to $CaCO_3$ was found to be about 21%. When conductivity value decreased to the value of 3.0 mS/cm, 47% of conversion was obtained. The conversion value increased until the conductivity value decreased to near 0.0 mS/cm. A near zero conductivity value indicated that all the $Ca(OH)_2$ would be consumed, converting all the Ca^{++} ions. At this point, a conversion of $Ca(OH)_2$ of 87.9% was obtained. A 88.04% conversion was obtained at the end of crystallization at about 0.38 mS/cm. After the near zero conductivity, it can be seen that there was no significant change in the conversion when reaction was completed at about zero conductivity.
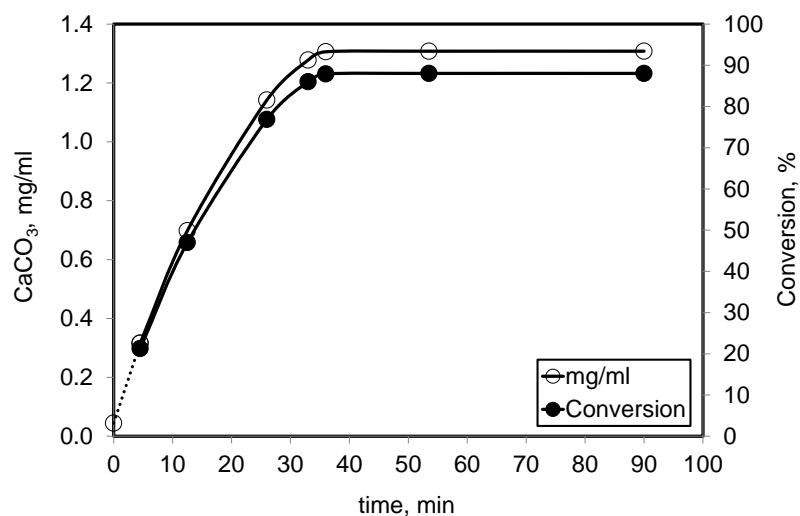
Figure 4.21. Change of conversion of $Ca(OH)_2$ to $CaCO_3$ over the reaction.

4.3. CO_2 Pulsation in the Small Penetration Method

Calcite particles were synthesized at different morphologies at different stages of crystallization. Whether different morphologies would be accumulated at each stage of crystallization, a pulsation method was studied. pH and conductivity values obtained by CO_2 pulsation in the reaction chamber were shown in Figure 4.22. As shown in figure, there was no significant change in pH and conductivity when CO_2 injection was stopped, and when CO_2 was injected, the decrease in the pH and conductivity was significant.
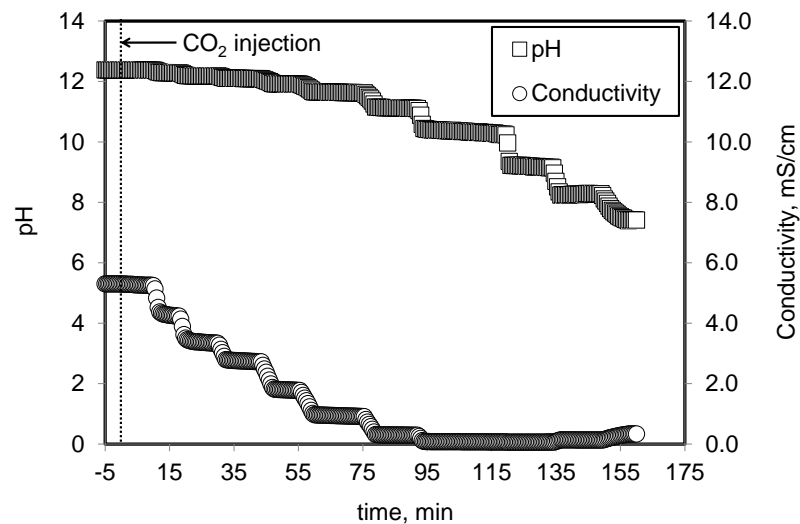
Figure 4.22. pH and conductivity during CO_2 pulsation into the reaction chamber.

Figure 4.23 shows the calculated [OH^-] and [Ca^{++}] concentration, and the consumption rate of these ions during the CO_2 pulsation. As shown in the figure, both OH^- and Ca^{++} ion concentration decreased when CO_2 was injected into the reaction chamber, and stabilized when CO_2 feeding into the reaction chamber was stopped. The neutralization of OH^- ions and the production of CO_3^{2-} ions were achieved by the dissolution of CO_2 into $Ca(OH)_2$ solution. When CO_3^{2-} was obtained by the dissolution of CO_2, Ca^{++} ions were consumed by the direct reaction with the CO_3^{2-} ions. Therefore, the Ca^{++} and OH^- ions decreased when CO_2 was injected into the reaction chamber. From the figure, the consumption rates for OH^- and Ca^{++} ions indicate that a sudden increase were seen when CO_2 injection was started, and rates became zero. Therefore, the consumption of Ca^{++} and OH^- ion concentrations can only be obtained by the CO_2 injection into the reaction chamber.
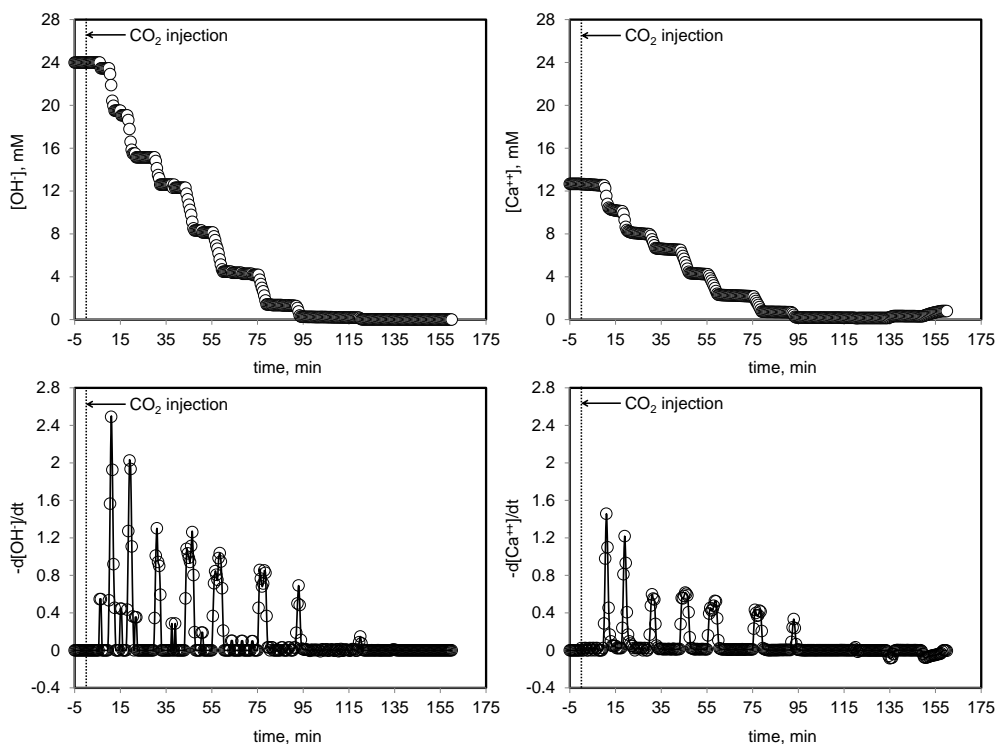
Figure 4.23. Calculated OH$^-$, and Ca^{++} ion concentrations, and their consumption rates.

Zeta potential values of particles were measured by the CO_2 pulsation method as shown in Figure 4.24. The zeta potential of 15 mM Ca(OH)$_2$ solution was found to be about 33 mV. When CO_2 was injected into the reaction chamber, zeta potential value increased suddenly from 33 mV to 47 mV. When CO_2 was fed into the reaction chamber, a 21% conversion was achieved as shown in Figure 4.24, and thus the zeta potential of $CaCO_3$ particles became higher in the Ca(OH)$_2$ solution. Upon producing more $CaCO_3$ particles and consuming the ions in the solution, zeta potential values slightly decreased until the conductivity was near 0.0 mS/cm. After the near zero conductivity, the increase in the zeta potential could be related to the redissolution of $CaCO_3$, resulting in variation in the surface charge of $CaCO_3$ particles.
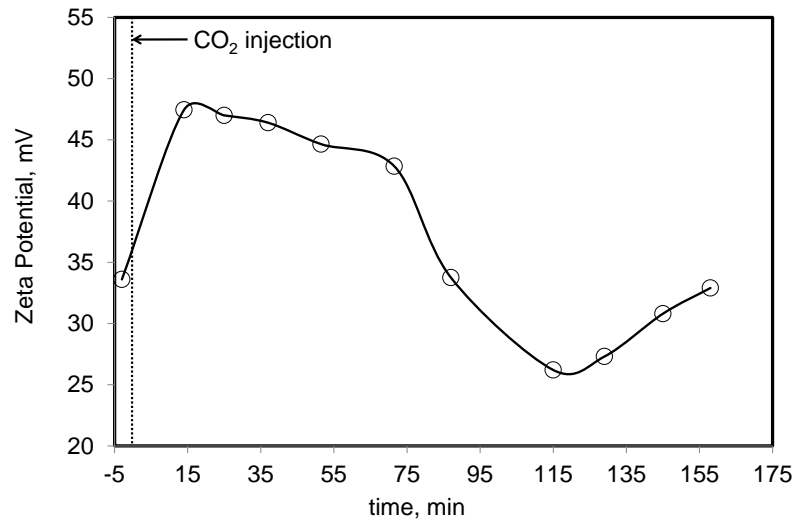
Figure 4.24. Zeta potential values during CO_2 pulsation.

Figure 4.25 shows the SEM images of the $CaCO_3$ particles obtained with the pulsation method at different conductivity values. As shown in the figure, the mechanism of $CaCO_3$ production was similar to the mechanism of continuous CO_2 injection as summarized in Figure 4.17. At the beginning of the $CaCO_3$ synthesis, submicron rice-like particles were obtained. It was proved from their XRD patterns shown in Figure 4.26 that the produced rice-like particles were aragonite and the other particles were calcite crystals. The length of produced rice-like particles decreased when the conductivity decreased. As shown in the figure, the formation of hollow particles was started at around 0.2906 mS/cm and produced at about zero conductivity. After near zero conductivity, hollow $CaCO_3$ particles were filled and submicron calcite particles were produced at the end of the crystallization by the CO_2 pulsation.

Cond.: 4.25 mS/cm

Cond.: 3.35 mS/cm

Cond.: 2.74 mS/cm

Cond.: 1.778 mS/cm

Cond.: 0.913 mS/cm

Cond.: 0.2906 mS/cm

Cond.: 0.0674 mS/cm

Cond.: 0.0695 mS/cm

Cond.: 0.1307 mS/cm

Cond.: 0.331 mS/cm
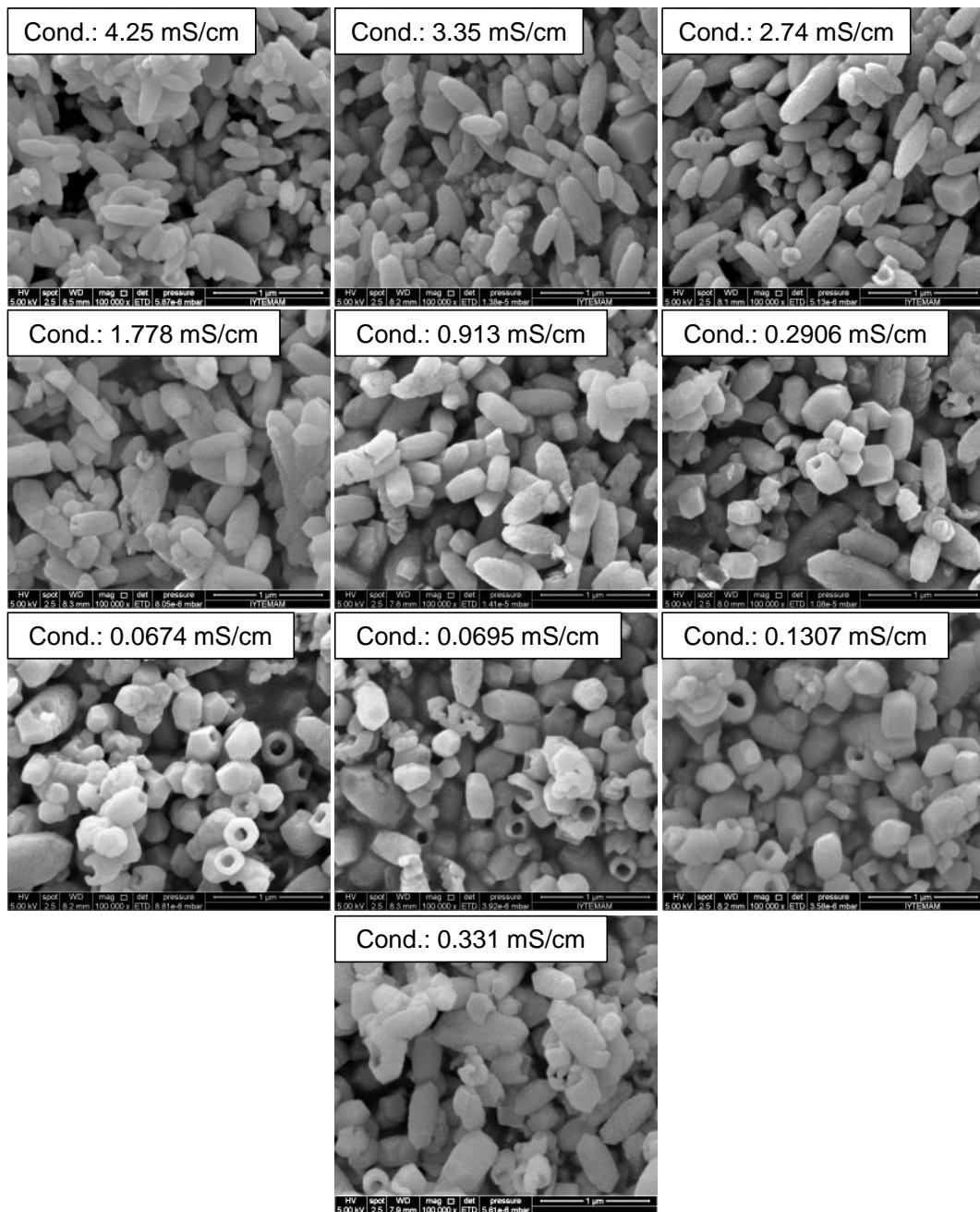
Figure 4.25. SEM images of the precipitates obtained at diffent conductivity values over the reaction by CO_2 Pulsation Method (Scale: 1 μm).

57
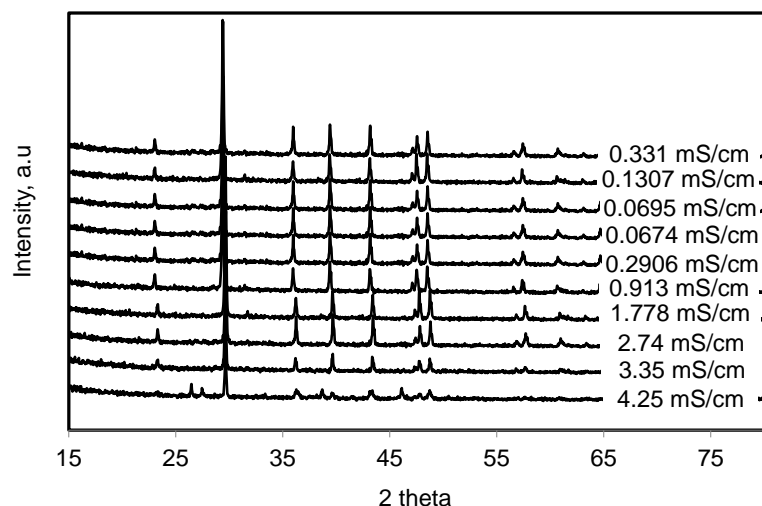
Figure 4.26. XRD patterns of all precipitates obtained over the reaction by CO_2 Pulsation Method.

In order to investigate the progress in hollow $CaCO_3$ particle formation at near zero conductivity values, CO_2 pulsation method was performed only at around zero conductivity value. Figure 4.27 shows the pH and conductivity value during CO_2 pulsation at about zero conductivity. The pH and conductivity values decreased in 10 min with the continuous CO_2 injection into the reaction chamber up to CO_2 pulsation. When CO_2 injection was stopped, the decrease in the pH and conductivity values stopped, and decreased again when CO_2 was started to inject.
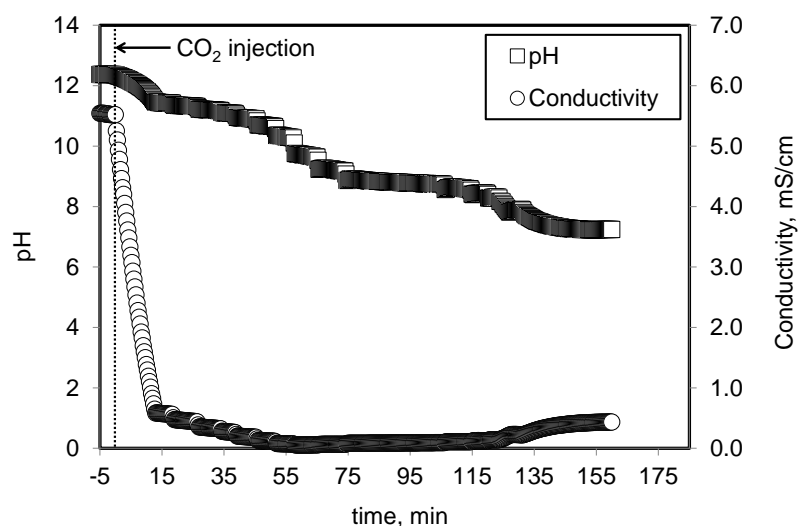
Figure 4.27. pH and conductivity values during CO_2 pulsation at around zero conductivity.

Calculated [OH⁻], and [Ca⁺⁺] ion concentration were shown in Figure 4.28. As depicted in the figure, the decrease in the OH⁻ ion concentration could be related to the dissolution of CO_2 in 15 mM of $Ca(OH)_2$ by the neutralization of OH⁻ ions, for which CO_3^{2-} ions will be produced. Therefore, the decrease in the Ca^{++} ion concentration could be related to the direct reaction with CO_3^{2-} ions. Figure 4.28 shows also the consumption rates for [OH⁻], and [Ca⁺⁺]. The increase in the consumption rates was significant when CO_2 was fed into the reaction chamber.
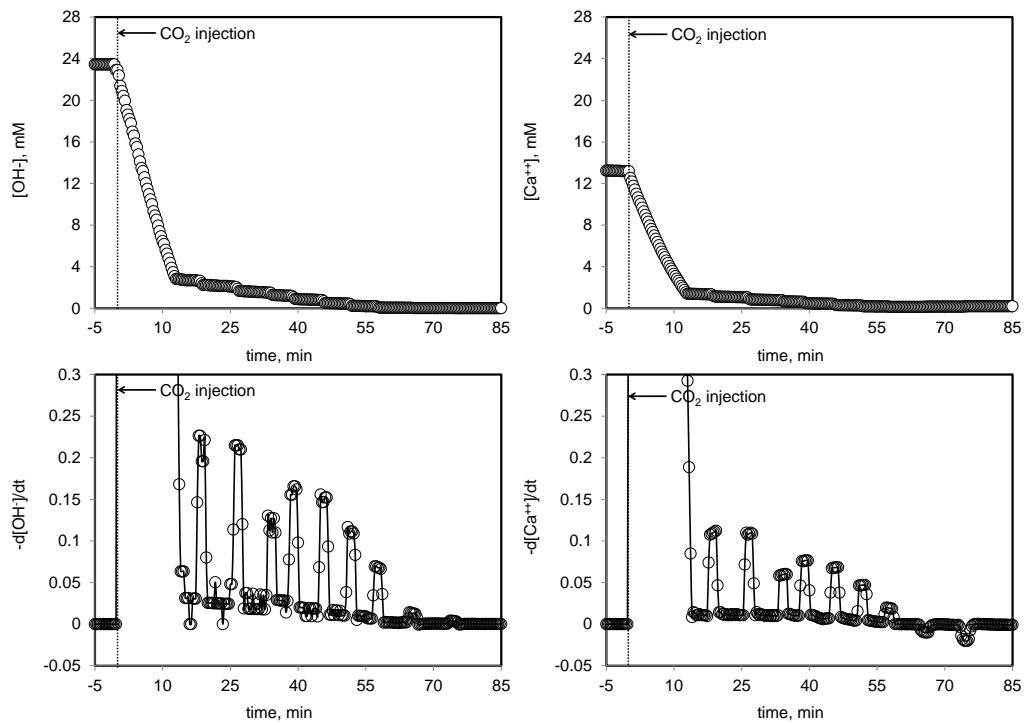
Figure 4.28. Calculated of OH⁻, and Ca^{++} ion concentrations, and their consumption rates during CO_2 pulsation method around zero conductivity value.

The zeta potential values of particles at about zero conductivity were shown in Figure 4.29. The zeta potential values decreased when the conductivity approached to the zero value. At about zero conductivity, the zeta potential reached its lowest value since the Ca^{++} ions were converted to the $CaCO_3$ by the reaction between Ca^{++} and CO_3^{2-} ions at about zero conductivity. After zero conductivity, zeta potential values increased slightly with the increase in ions such as HCO_3^- as a result of CO_2 dissolution, and particle dissolution.
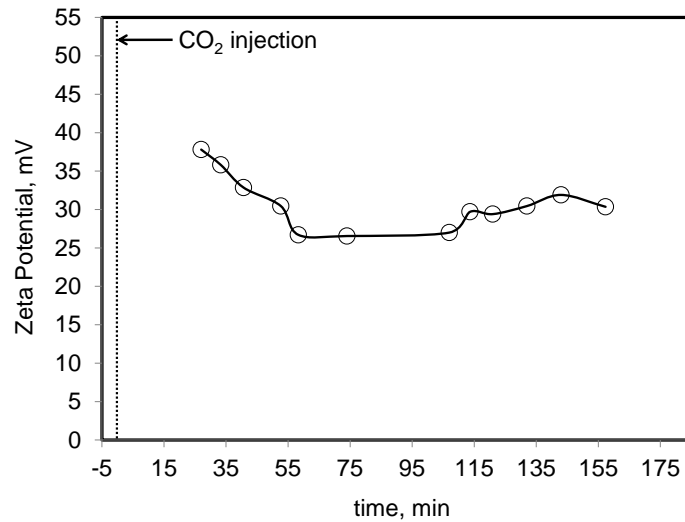
Figure 4.29. Calculated of zeta potential obtained at around zero conductivity by CO_2 Pulsation Method.

Figure 4.30 shows the SEM images of the crystals obtained by the CO_2 pulsation method at about zero conductivity. As shown in Figure 4.30, hollow $CaCO_3$ particles were produced about zero conductivity. It seems that the way how CO_2 was injected into the reaction chamber is important. When the CO_2 injection was cut, particle dissolution was slow and the number of hollow particle formation was lower. At late stage of crystallization, because the zeta potential values were lower, an aggregation among particles were seen. All particles produced were calcite as shown from the XRD patterns in Figure 4.31.

Cond.: 0.450 mS/cm

Cond.: 0.340 mS/cm

Cond.: 0.264 mS/cm

Cond.: 0.115 mS/cm

Cond.: 0.071 mS/cm

Cond.: 0.0647 mS/cm

Cond.: 0.0918 mS/cm

Cond.: 0.106 mS/cm

Cond.: 0.125 mS/cm

Cond.: 0.222 mS/cm

Cond.: 0.354 mS/cm

Cond.: 0.427 mS/cm
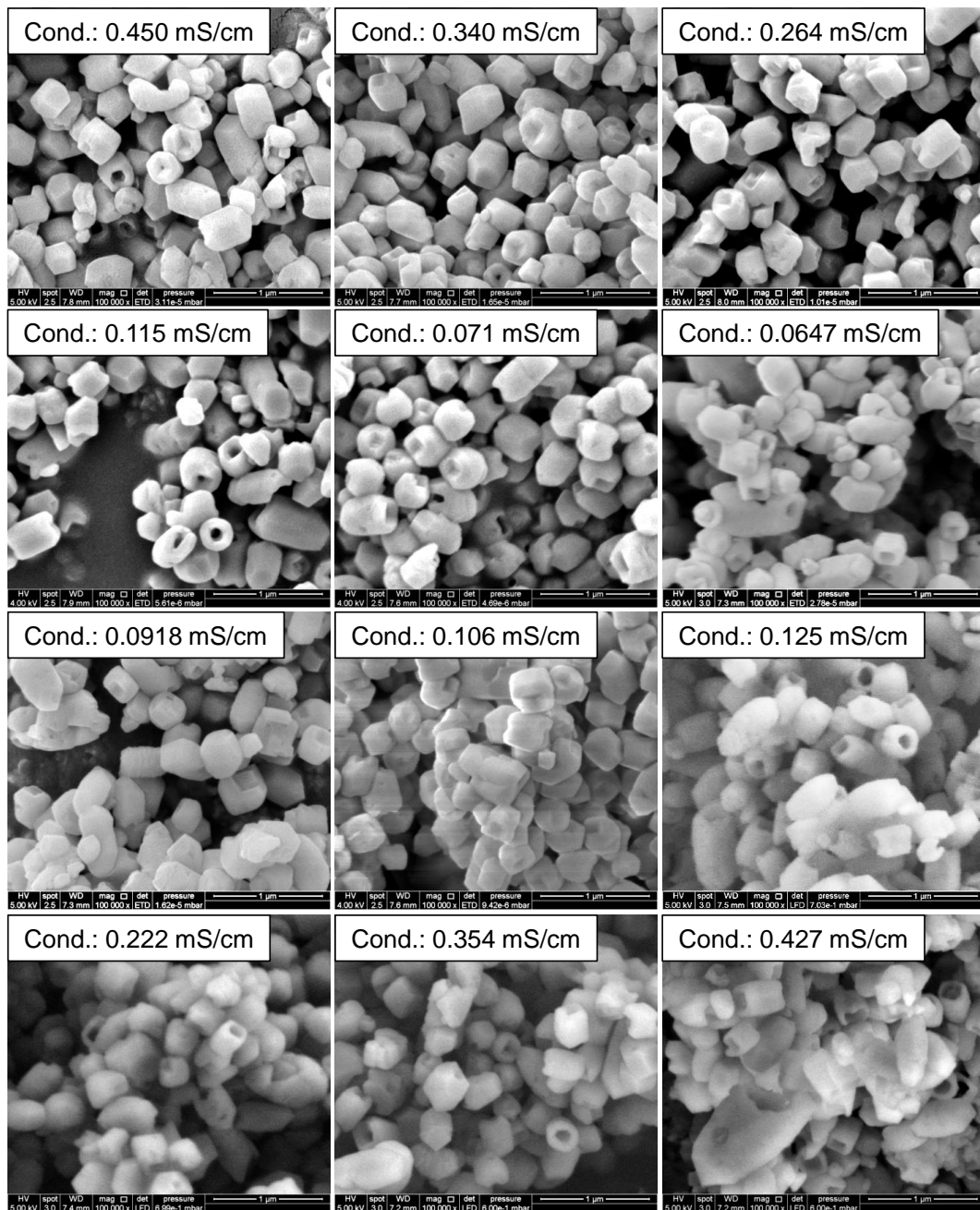
Figure 4.30. SEM images of calcite obtained from diffent conductivity values at around zero conductivity by CO_2 pulsation method (Scale: 1 µm).
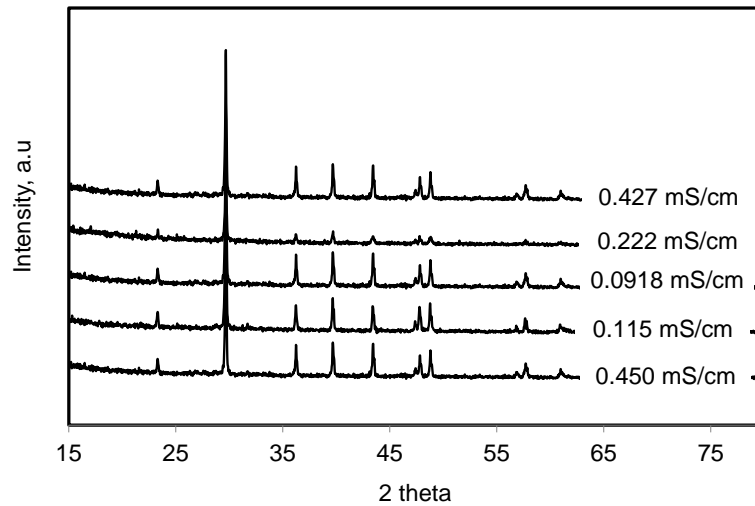
Figure 4.31. XRD patterns of various precipitates obtained at around zero conductivity.

4.4. Parametric Studies

The CO_2 dissolution in liquid phase may be important parameter to obtain monodisperse and nano sized $CaCO_3$ crystals. It was proposed that CO_2 dissolution rate could be related to the different parameters, as shown in Eq.(3.4), such as the surface area of liquid phase (A), OH^- ion concentration (C_B), maximum velocity of liquid phase (v_{max}), and the length between liquid and gas phases (L). Such parameters could determine CO_2 dissolution rate and affect the particle size, and therefore, their effects were investigated for the nano $CaCO_3$ formation as follows.

4.4.1. Effect of Stirring Rate

Effect of stirring rate on the nano $CaCO_3$ particle formation was investigated. Stirring rate in the stabilization tank would not directly associate with the CO_2 dissolution rate as shown in Eq.(3.4). However, Kitamura et al., (2002) reported that the amount of the agglomerated particles of calcite could be large at low stirring rate (Kitamura, Konno, Yasui, & Masuoka, 2002). In addition, needle-like aragonite particles could be obtained when the stirring rate in a 300 ml cylindrical crystallizer increased since the shear rate can be considerably high result in vortex formation. Therefore, the effect of stirring rate on the polymorph of $CaCO_3$ may be considered.

pH and conductivity values recorded for each stirring rate were shown in Figure 4.32. Calculated [OH⁻] and [Ca⁺⁺] ion concentrations obtained from the pH and conductivity values were also included in the figure. pH and conductivity values seemed to be the same for each stirring rate during the $CaCO_3$ synthesis. Change in [OH⁻] and [Ca⁺⁺] ion concentrations were also the same for different stirring rate experiments during the precipitation indicating that the repeatable and reproducible results could be obtained. As shown in the figure, the [OH⁻] and [Ca⁺⁺] ion concentrations decreased up to near zero conductivity value when the CO_2 was fed into the reaction chamber. After the near zero conductivity, while the OH⁻ ion concentration was found to be about 0 mM, there was a slight increase in [Ca⁺⁺] ion concentration after the near zero conductivity. The increase in the [Ca⁺⁺] could be associated with the increase in charged species due to the CO_2 dissolution such as HCO_3^-, H^+, $CaOH^+$ ionic species, and $CaCO_3^+$ clusters as well as the consumption of OH⁻ ion concentration.
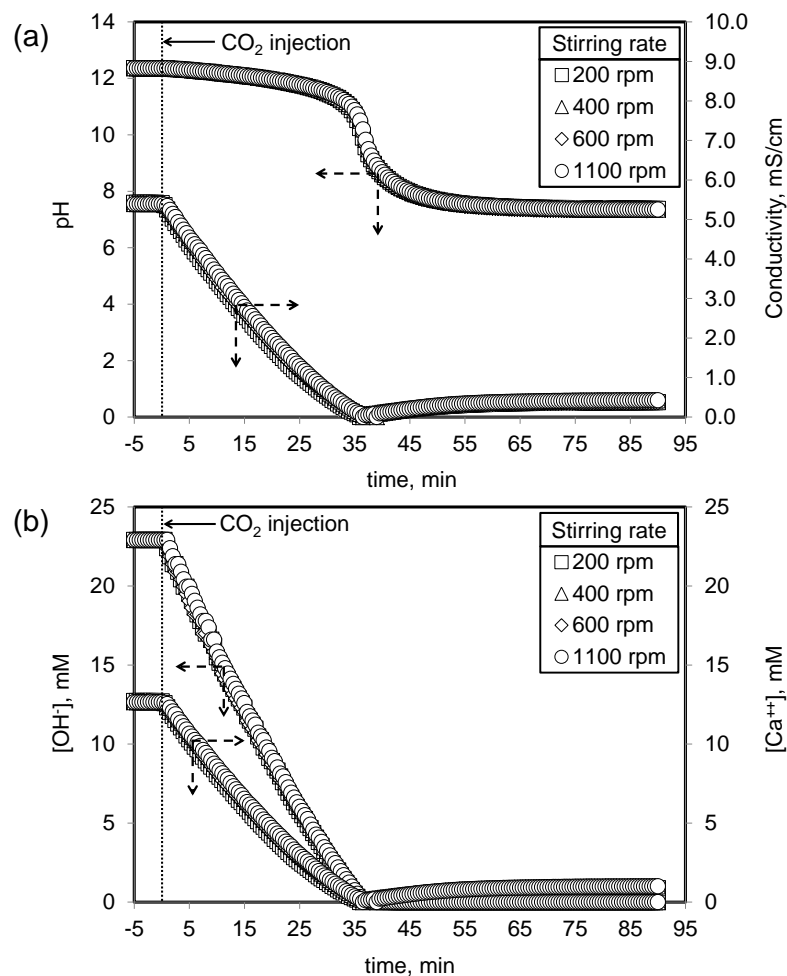
Figure 4.32. (a) pH, and conductivity values and (b) calculated [OH⁻] and [Ca⁺⁺] ion concentrations obtained for each stirring rate during crystallization.

Figure 4.33 shows the consumption rate for [OH⁻] and [Ca⁺⁺] ion concentrations during $CaCO_3$ crystallization at 200 rpm. The consumption rate for both Ca^{++} and OH^- ion concentrations were sharply increased. These consumption rates were decreased as the crystallization progressed. The decrease in the consumption rate could be related to the consumption of [OH⁻] and [Ca⁺⁺] ions in the crystallization chamber. At about zero conductivity, the consumption rate for both ion concentrations decreased sharply, where [OH⁻] ion concentration reached the smallest value of about 0, and the consumption rate of [Ca⁺⁺] reached the negative values, and then returned back to the positive values. The negative value for the consumption rate means the generation of Ca^{++} ions at about zero conductivity. Also worth to note that, while this consumption rate for Ca^{++} ions was steady, that for the OH^- ions, the consumption rate was fluctuated, especially at the initial stage of the crystallization indicating that there might form some OH^- ions complexes, or any surfaces attached by the OH^- ions would be desorbed back, and therefore, OH^- ion concentration would be fluctuated in the crystallization solution.
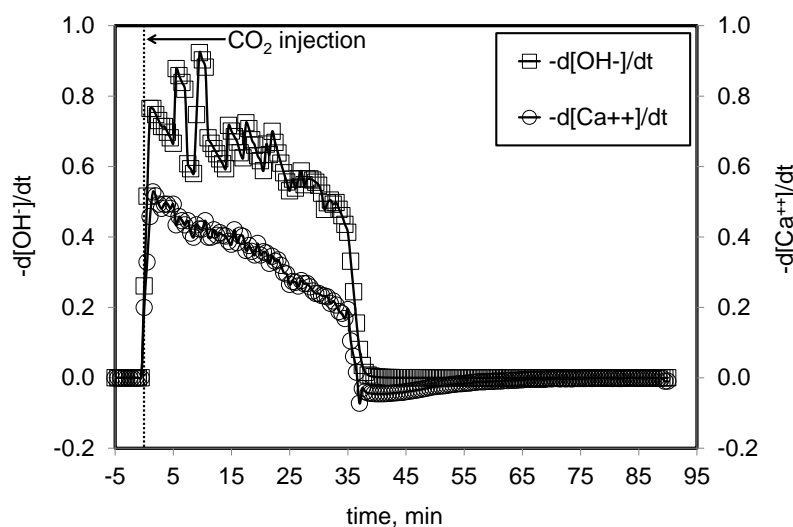
Figure 4.33. Consumption rate of OH^- and Ca^{++} ion concentrations during $CaCO_3$ crystallization performed at 200 rpm.

Figure 4.34 shows the zeta potential and average particle size obtained for each stirring rate experiments. As shown in the figure, repeatable results were obtained. The zeta potential for a 15 mM $Ca(OH)_2$ solution was found to be about 33 mV. When CO_2 was injected into the reaction chamber, zeta potential values for different stirring rate experiments increased significantly. Then, zeta potential value decreased up to near zero conductivity with the consumption of Ca^{++} ions in the aqueous solution. After near zero

conductivity, zeta potential values slightly increased with the increase in charged species due to the CO_2 dissolution as well as the newly formed $CaCO_3$ redissolution. The average particle size for each stirring rate experiment increased with time during $CaCO_3$ synthesis. The changes in zeta potential and the average particle size were the same for each stirring rate experiments, indicating repeatable and reproducible results in the developed small penetration method.
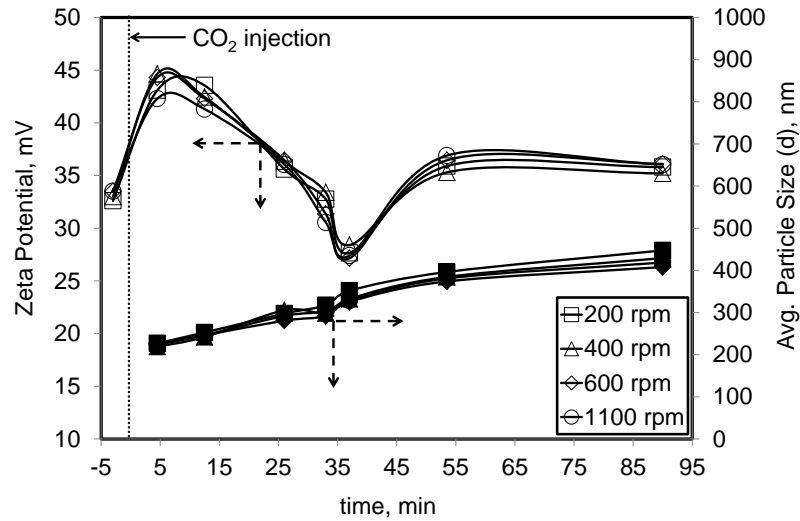
Figure 4.34. Zeta potential and average particle size obtained for different stirring rates during $CaCO_3$ crystallization.

Figure 4.35 shows the SEM images for the $CaCO_3$ crystal particles obtained at 200 rpm during $CaCO_3$ precipitation. At the beginning of the reaction, rice–like and rhombohedral crystals were obtained. Then, the length of particles decreased with decreasing conductivity as the crystallization progressed. The hollow particle formation was started at conductivity values about 0.3 mS/cm. The maximum populations of hollow particles were obtained at near zero conductivity. After the near zero conductivity, the hollow crystals were filled and submicron $CaCO_3$ particles were produced.
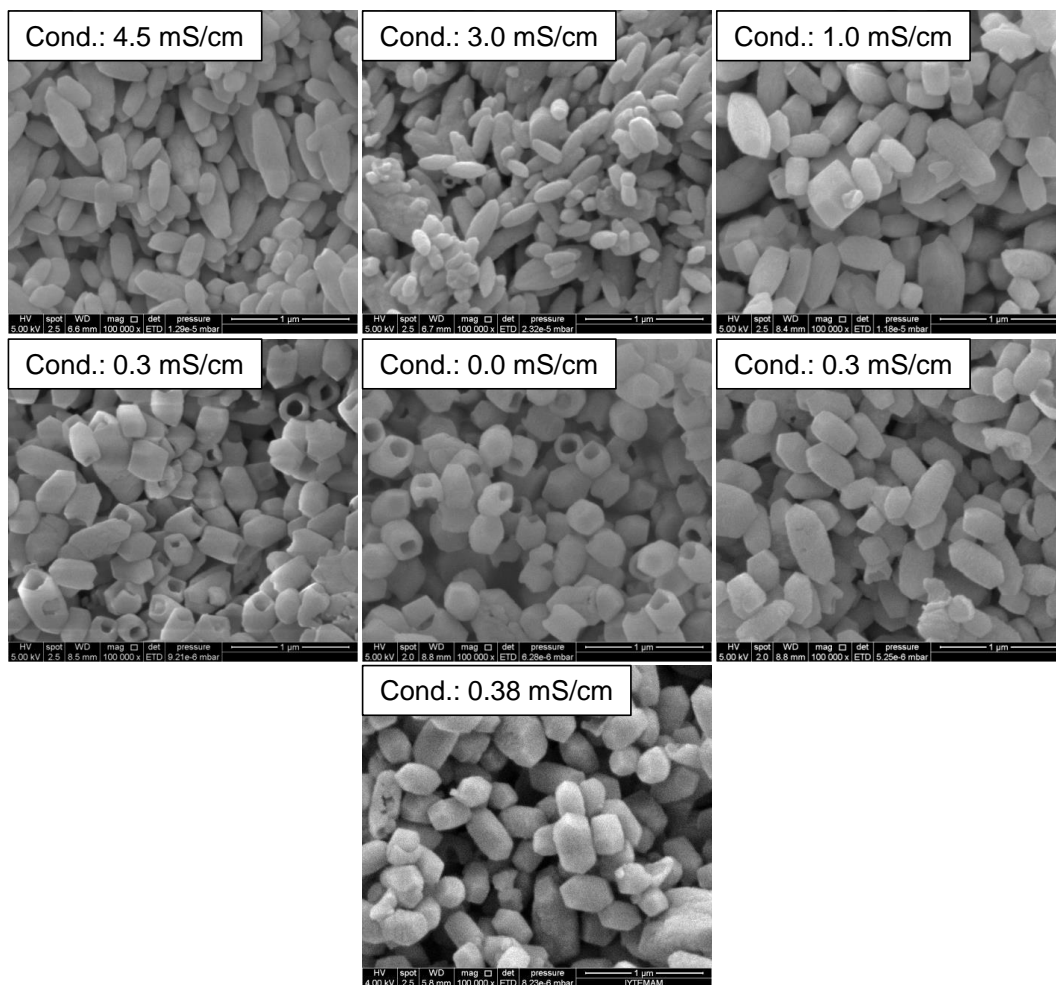
Figure 4.35. SEM images of the $CaCO_3$ particles obtained at 200 rpm stirring rate (Scale: 1 μm).

The SEM images of $CaCO_3$ particles obtained at the end of each stirring rate experiments were compared in Figure 4.36. Since the CO_2 dissolution rates for all stirring rates were the same, there was no significant difference in the $CaCO_3$ crystals precipitated at the end of each stirring rates. As shown in Figure 4.37, all precipitated crystals obtained for each stirring rate experiment were calcite crystals.
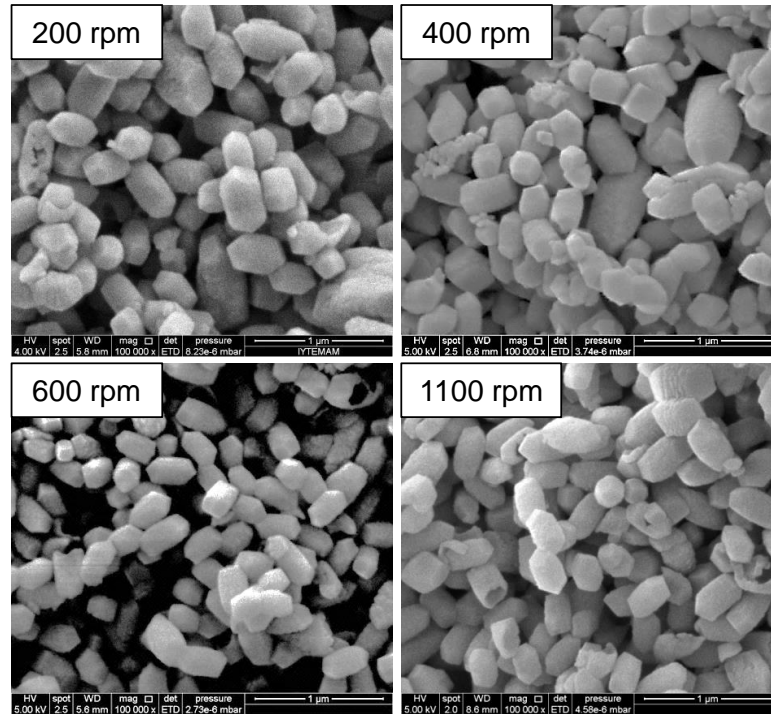
Figure 4.36. SEM images of CaCO$_3$ particles obtained for different stirring rates at the end of crystallization (Scale: 1 μm).
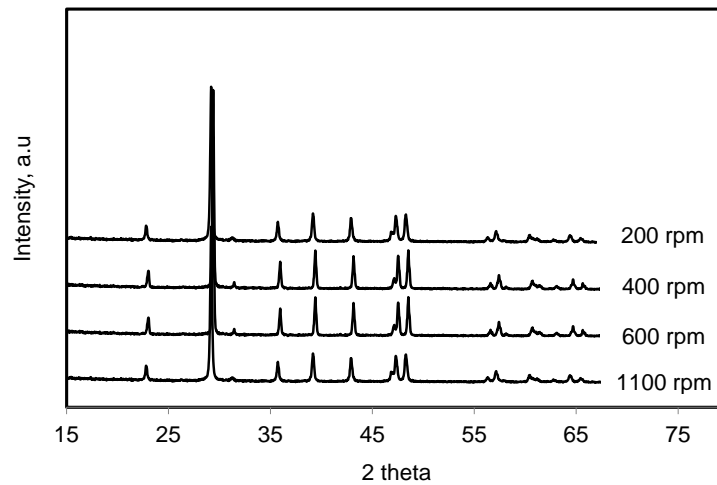
Figure 4.37. XRD pattern of the precipitates obtained for all stirring rates at the end of the reaction.

4.4.2. Effect of Ca(OH)$_2$ Flow Rate

As shown in Eq.(3.4), the maximum velocity of the liquid phase may be directly related to the CO$_2$ dissolution rate in small penetration method. The maximum velocity of liquid phase is proportional to the Ca(OH)$_2$ flow rate when the feeding pipe diameter

were kept constant for each $Ca(OH)_2$ flow rates. Therefore, the change in the $Ca(OH)_2$ flow rate resulted in the change in the maximum velocity of the $Ca(OH)_2$ solution. As a result, the change in the CO_2 dissolution rate can be varied with the different liquid flow rates.

Figure 4.38 shows the pH and conductivity values for each $Ca(OH)_2$ flow rates during $CaCO_3$ precipitation. As shown in the figure, the conductivity values for different $Ca(OH)_2$ flow rates decreased when the CO_2 was injected into the reaction chamber. However, the consumption time of ions decreased with the increasing $Ca(OH)_2$ flow rate indicating that the increase in maximum velocity of 15 mM $Ca(OH)_2$ could be related to the decrease in the consumption time of ions. The figure also shows the calculated $[OH^-]$ and $[Ca^{++}]$ concentrations during $CaCO_3$ crystallization. The change in $[OH^-]$ ion concentration could be related to the CO_2 dissolution rate indicating that the consumption time of [OH-] decreased when the CO_2 dissolution rate increased. Therefore, the CO_2 dissolution rate in liquid phase increased with increasing maximum velocity of liquid phase. As shown in the figure, the consumption time for the $[Ca^{++}]$ ions decreased when CO_2 dissolution rate increased. On the other hand, the linearity in the $[OH^-]$ ion concentration change with time during reaction showed that the constant CO_2 injection were obtained for each $Ca(OH)_2$ flow rate experiments.
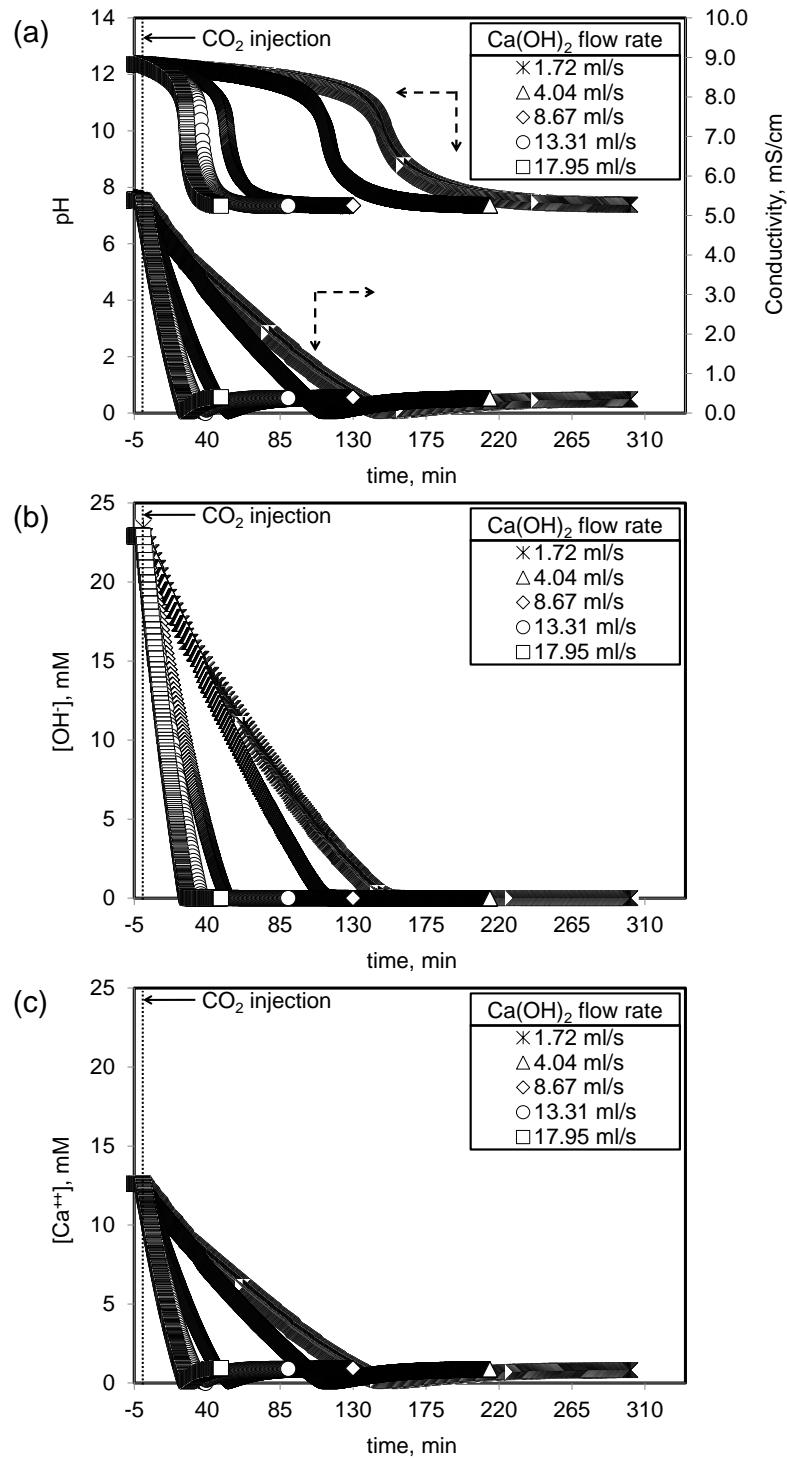
Figure 4.38. (a) pH, and conductivity values, (b) calculated [OH⁻] and (c) [Ca⁺⁺] for
Ca(OH)₂ flow rate experiments.

Figure 4.39 shows the calculated [OH⁻], and [Ca⁺⁺] concentrations and their
consumption rates for [Ca(OH)₂ flow rate at 17.95 ml/s during the $CaCO_3$
crystallization. As given in the figure, the consumption rate of [OH⁻] and [Ca⁺⁺]
increased initially when CO_2 was injected into the reaction chamber, and reached its

maximum value. Then, the consumption rate started to decrease through crystallization when [OH⁻] and [Ca⁺⁺] concentrations were decreased with time. At about zero conductivity, the consumption rate of [OH⁻] and [Ca⁺⁺] sharply decreased.
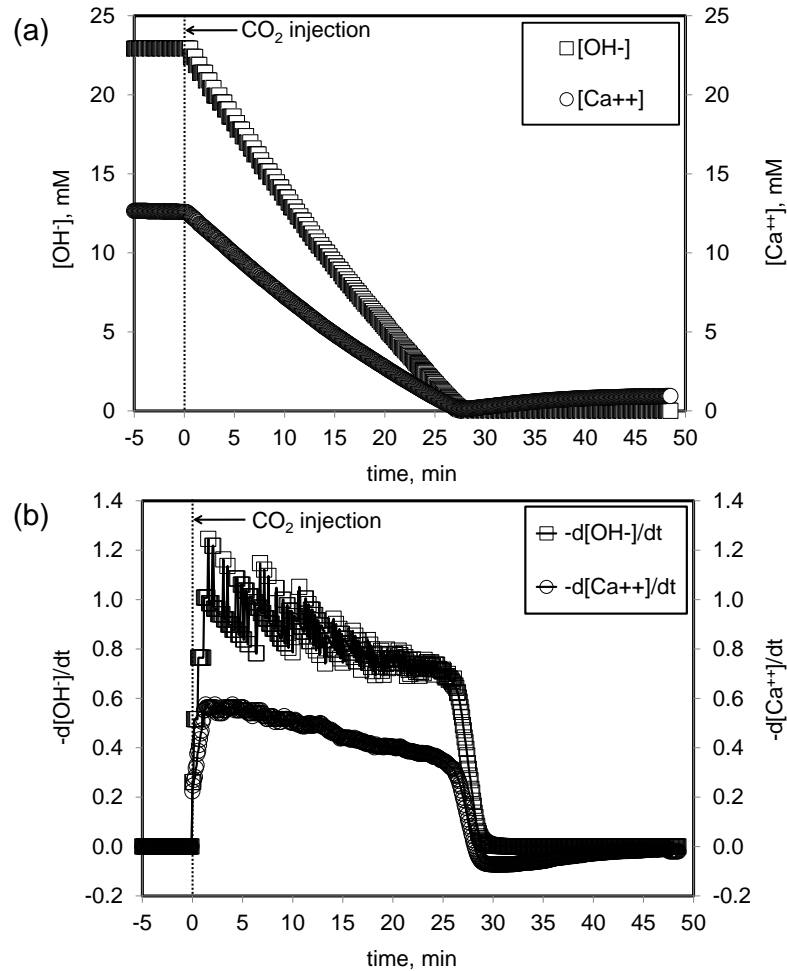
Figure 4.39. (a) Calculated OH⁻, and Ca⁺⁺ ion concentrations, and (b) their consumption rate for $Ca(OH)_2$ flow rate at 17.95 ml/s.

Figure 4.40 showed the zeta potential and average particle size obtained for different $Ca(OH)_2$ flow rate experiments. As shown in the figure, the change in the average $CaCO_3$ size was found to be smallest for higher $Ca(OH)_2$ flow rate. On the other hand, the change in the average particle size was higher when the $Ca(OH)_2$ flow rate was lower during $CaCO_3$ precipitation. It was expected that the faster the CO_2 dissolution, the larger the particle size. However, the opposite results were obtained as shown in the figure. The stabilization time was longer for low $Ca(OH)_2$ flow rates and it was shorter for higher $Ca(OH)_2$ flow rates, which affect did not affect the particle size. The stabilization time is the required time to transport the $CaCO_3$ particles from the

reaction chamber to the stabilization tank in order to stabilize the particles with the Ca^{++} ions. Although CO_2 dissolution rate was higher for the higher $Ca(OH)_2$ flow rates, the stabilization time was smaller. As shown in the figure, the minimum value for zeta potential were increased when the $Ca(OH)_2$ flow rate was increased. Although the increase in the $Ca(OH)_2$ flow rate significantly reduced the crystallization time, the formation of particles followed the same trend and similar sized particles were obtained. Therefore, the stabilization time would be an important parameter for nano $CaCO_3$ particle size.
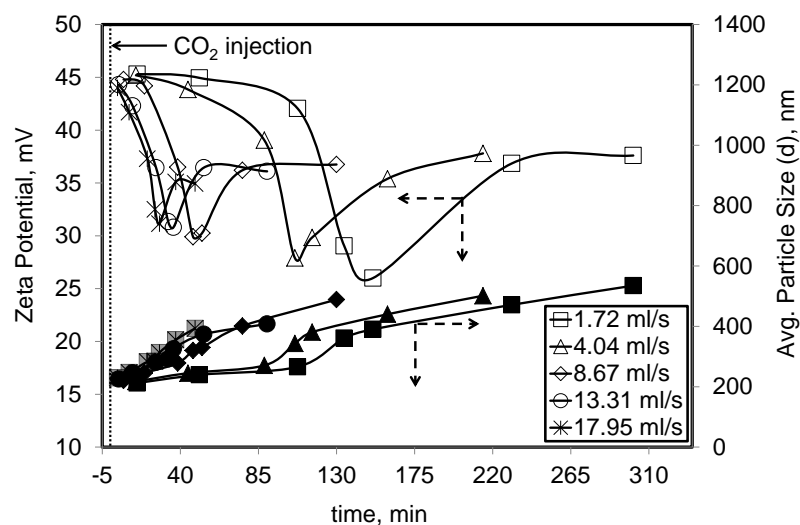
Figure 4.40. Zeta potential and average particle size for different $Ca(OH)_2$ flow.

The SEM images of the $CaCO_3$ particles produced for $Ca(OH)_2$ flow rate at 17.95 ml/s were shown in Figure 4.41. As shown in the figure, similar particles were produced as discussed before. Rice-like particles were produced initially. These particles were converted into hollow nano $CaCO_3$ particles at around zero conductivity values, and solid nano $CaCO_3$ particles were obtained at the end of the crystallization. As shown from the XRD patterns in Figure 4.42, aragonite and calcite peaks were observed at the beginning of the reaction. Afterwards, all crystals were found to be calcite.
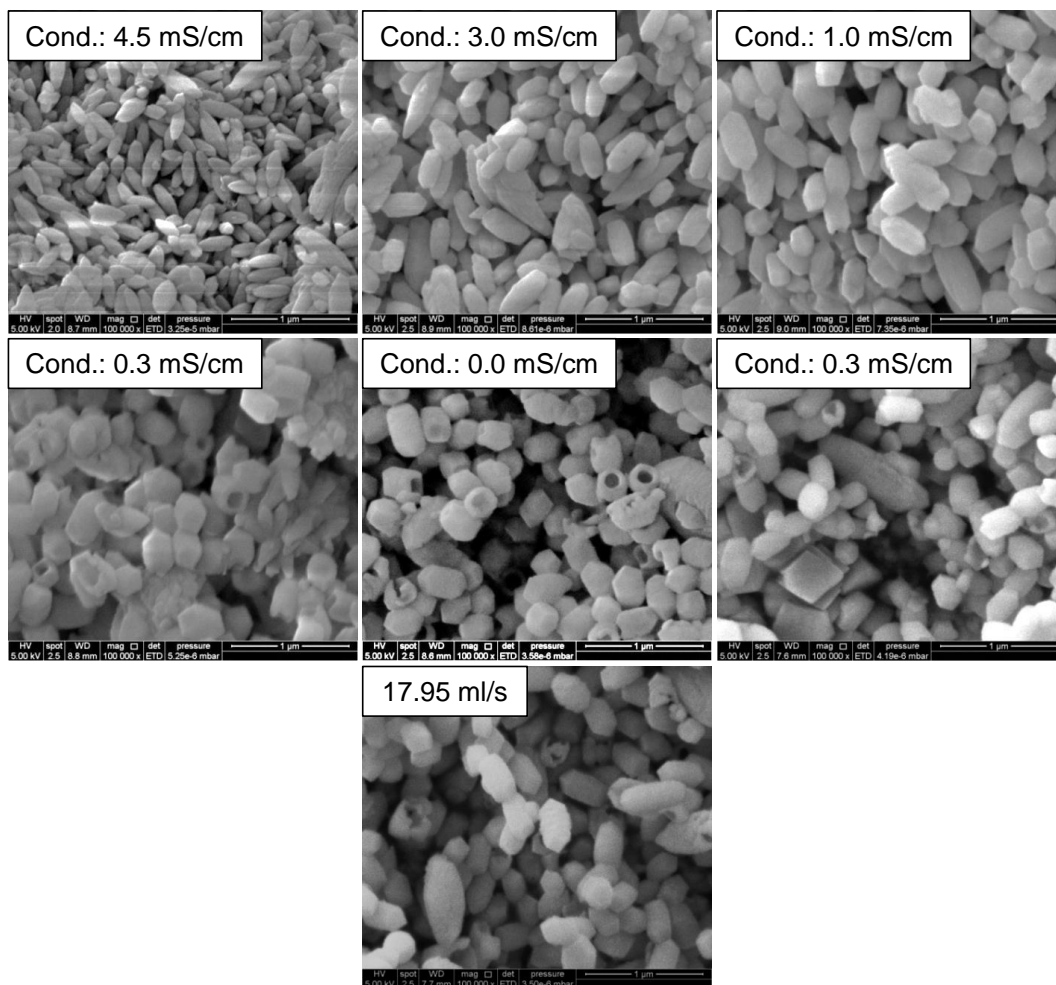
Figure 4.41. SEM images of CaCO$_3$ crystals obtained for Ca(OH)$_2$ flow rate at 17.95 ml/s during CaCO$_3$ crystallization (Scale: 1 μm).
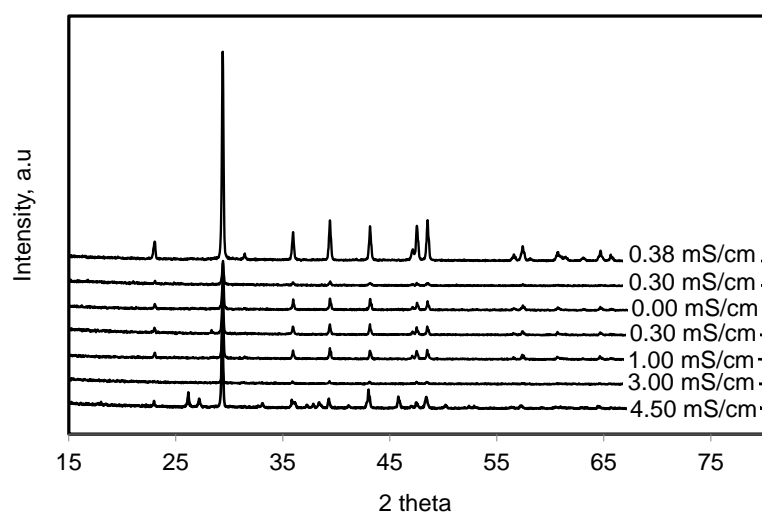
Figure 4.42. XRD patterns of the particles obtained for different conductivity values during the CaCO$_3$ crystallization at 17.95 ml/s.

Figure 4.43 shows the SEM images of CaCO$_3$ particles obtained at the end of crystallization for different Ca(OH)$_2$ flow rates. As shown in the figure, similar particles were produced but some aggregated particles were discerned. The aggregation of precipitates were noticeable at lower Ca(OH)$_2$ flow rates. The rhombohedral CaCO$_3$ particles were obtained for each Ca(OH)$_2$ flow rate. All of CaCO$_3$ particles obtained were calcite as evidenced from the XRD patterns as shown in Figure 4.44.
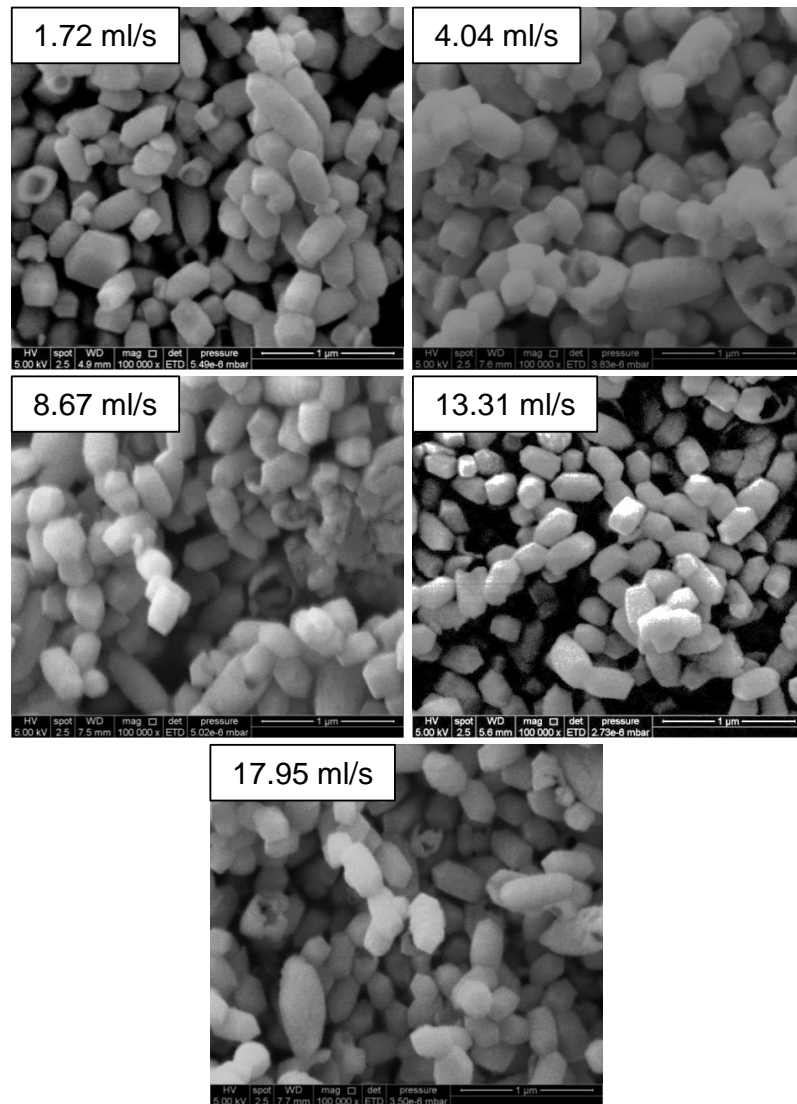
Figure 4.43. SEM images of the CaCO$_3$ particles obtained for different Ca(OH)$_2$ flow rate experiments (Scale: 1 μm).
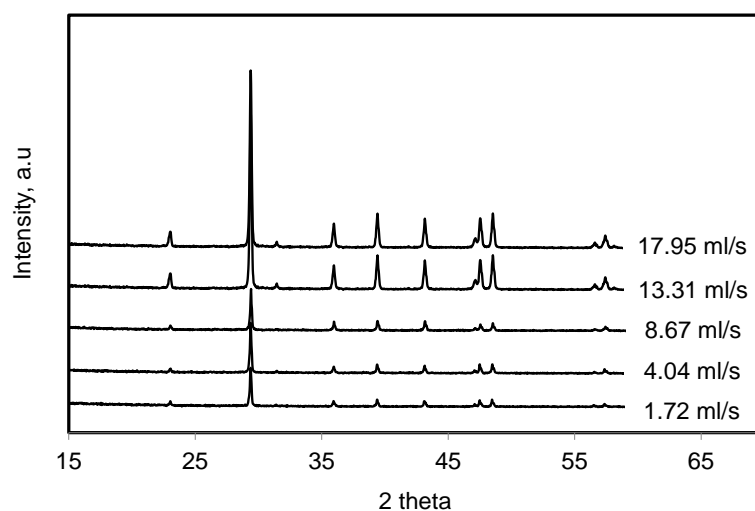
Figure 4.44. XRD patterns of the $CaCO_3$ particles obtained for different $Ca(OH)_2$ flow rates.

4.4.3. Effect of CO_2 Flow Rate

CO_2 dissolution rate may affect the aggregation of particles, particle size, and monodisperse $CaCO_3$ production. Therefore, 4 different CO_2 flow rates were studied keeping the reaction chamber, volume, and all the other parameters to be constant. Figure 4.45 shows pH and conductivity values for different CO_2 flow rates during $CaCO_3$ crystallization. As shown in the figure, the consumption time of ions decreased significantly when CO_2 injection rate into the reaction chamber was increased. The calculated $[OH^-]$ and $[Ca^{++}]$ ion concentrations for each CO_2 flow rates were also shown in the figure. The consumption time for $[OH^-]$ ion could be directly related to the CO_2 dissolution rate. As shown in the figure, the consumption rate of $[OH^-]$ during the $CaCO_3$ synthesis decreased with the increase in the CO_2 flow rate.
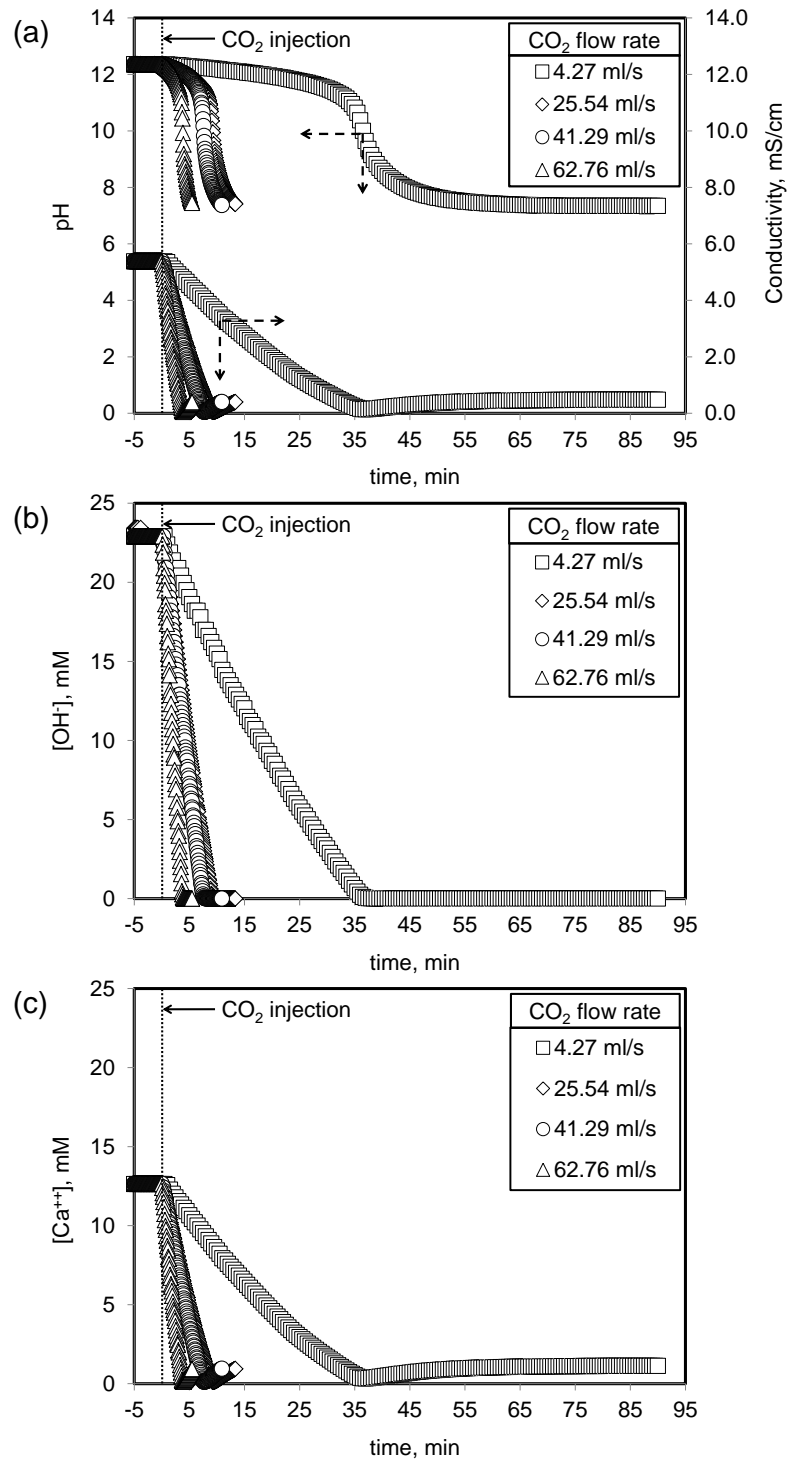
Figure 4.45. (a) pH, and conductivity values and (b) calculated [OH⁻] and (c) [Ca⁺⁺] ion concentrations for each CO_2 flow rate during $CaCO_3$ crystallization.

Figure 4.46 shows the calculated [OH⁻], and [Ca⁺⁺] ion concentrations, and their consumption rates for highest CO_2 flow rate at 62.76 ml/s during the $CaCO_3$ crystallization. As depicted above, the consumption of both [OH⁻] and [Ca⁺⁺] concentrations decreased linearly when the CO_2 was fed into the reaction chamber. The

consumption rate of [OH⁻] ion concentration increased sharply when the CO_2 was injected into the reaction chamber while [OH⁻] concentrations decreased linearly. Then, the consumption rate of both [OH⁻] and [Ca⁺⁺] ions decreased with the decrease in the [OH⁻] and [Ca⁺⁺] ion concentrations. At about zero conductivity, the decrease in [OH⁻] and [Ca⁺⁺] reached the lowest values.
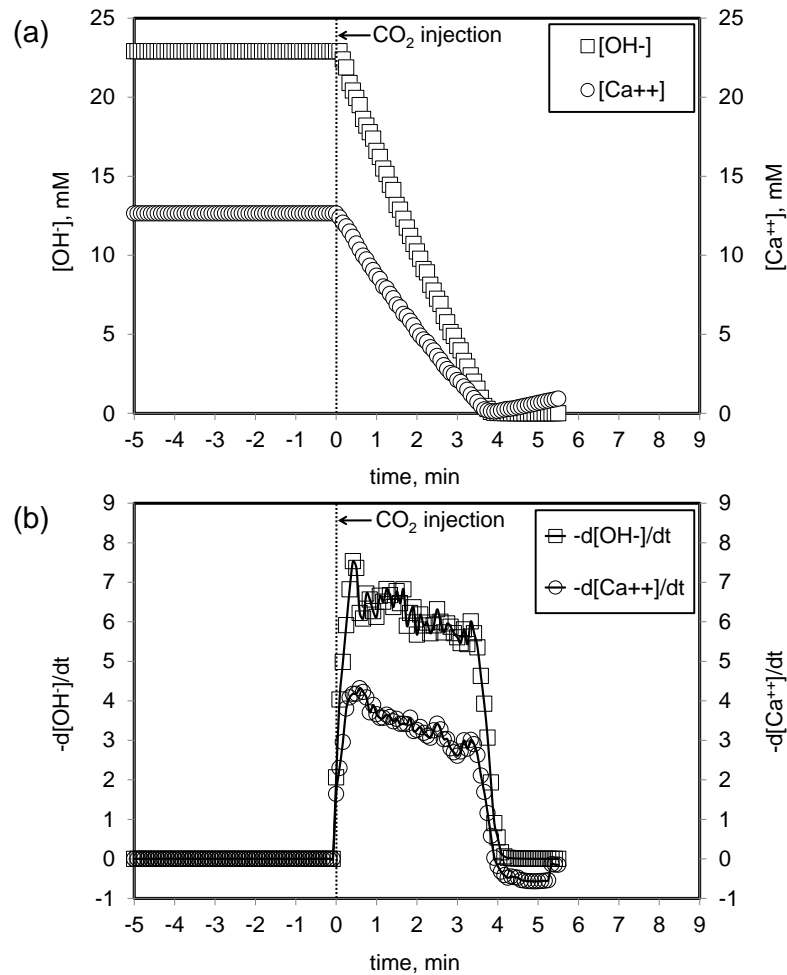
Figure 4.46. (a) Calculated OH⁻, and Ca⁺⁺ ion concentrations, and (b) their consumption rates at high CO_2 flow rate at 62.76 ml/s.

Figure 4.47 shows zeta potential and average particle size for different CO_2 flow rate experiments during crystallization. As shown in the figure, similar trend was shown for each CO_2 flow rate. However, when noticed, the minimum value for the zeta potential decreased when the CO_2 flow rate was increased during the $CaCO_3$ synthesis. The average particle size was small when the CO_2 flow rate was smaller and when the CO_2 flow rate was increased, the average particle size was significantly higher.
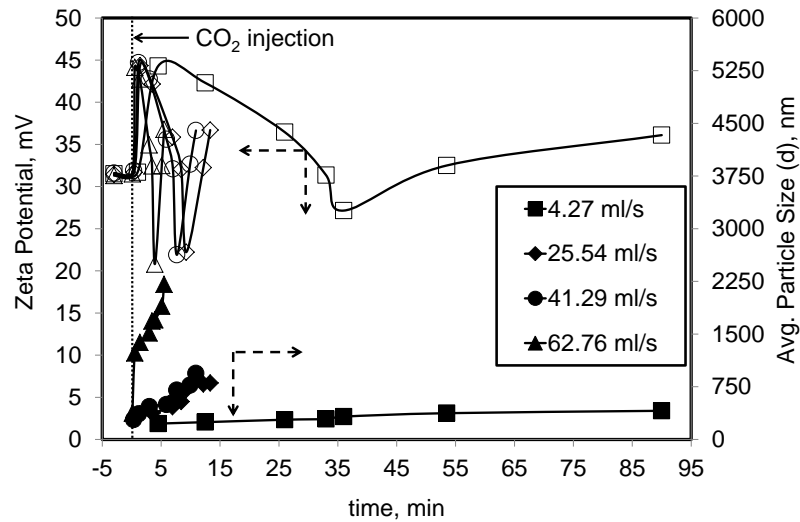
Figure 4.47. Zeta potential and average particle diameter obtained for different CO_2 flow rates.

Figure 4.48 shows the SEM images of precipitated crystals obtained at CO_2 flow rate of 62.76 ml/s. As shown in the figure, aggregated nano particles were formed during the crystallization. High supersaturation is required to produce nanoparticles as presented in Eq.(2.2) (K. Wang et al., 2007). Since high concentration of carbonate ion was obtained when CO_2 flow rate was increased, the supersaturation ratio was increased. Therefore, nano particles were obtained during the $CaCO_3$ synthesis. However, those crystals were found to be in the aggregated form. Since the zeta potential for 62.76 ml/s of CO_2 flow rate was found to be in between the aggregation limit (-30 and +30 mV) as shown in Figure 4.47, some of the nano particles were found in the aggregated form. Therefore, when the CO_2 flow rate was higher, the $CaCO_3$ particles will probably form aggregates.
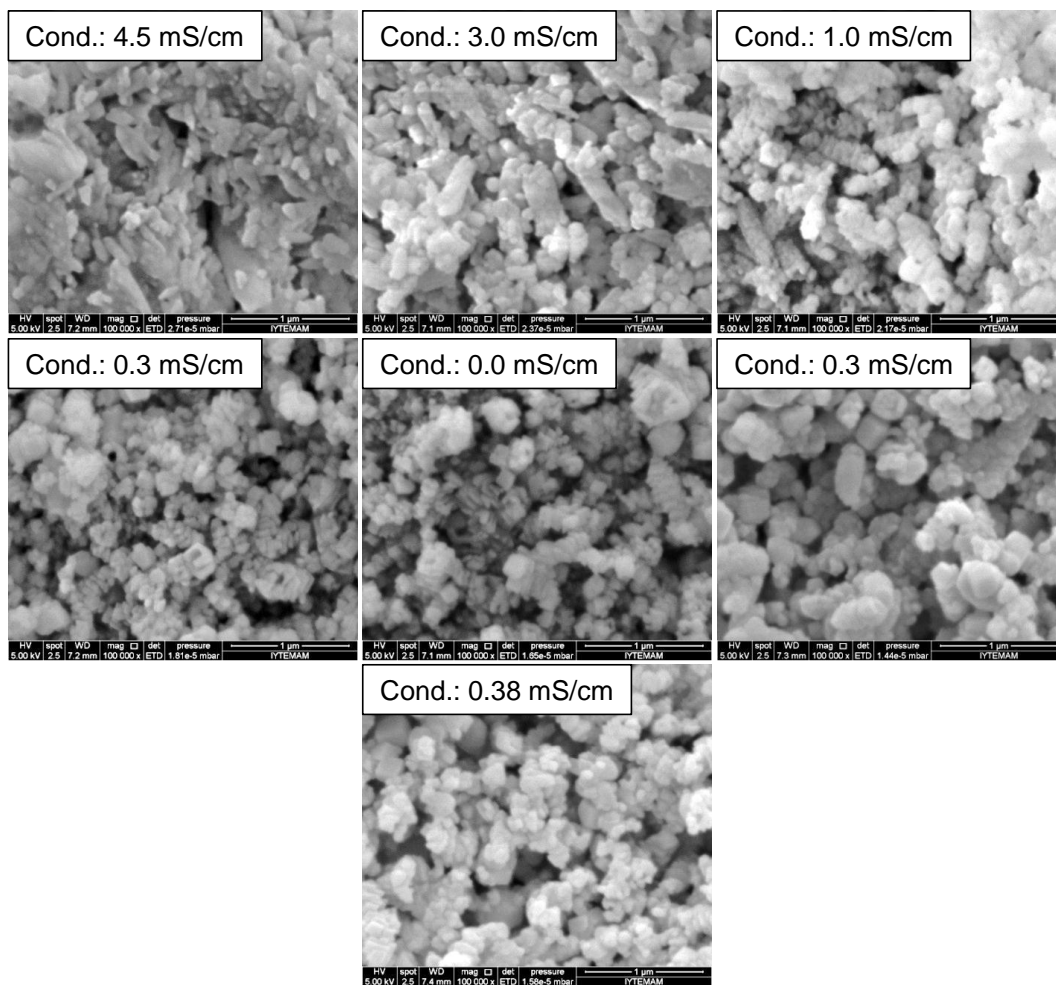
Figure 4.48. SEM images of $CaCO_3$ crystals obtained for CO_2 flow rate at 62.76 ml/s (Scale: 1μm).

SEM images of the $CaCO_3$ particles obtained at the end of each CO_2 flow rates were given in Figure 4.49. As shown in the figure, monodisperse calcite particles were obtained for lower CO_2 flow rate at 4.27 ml/s. When CO_2 flow rate was increased, an aggregation was observed. On the other hand, particle size decreased with increasing CO_2 flow rate. Therefore, monodisperse $CaCO_3$ particles with sizes of about 250 nm were produced at lower CO_2 injection rate whereas aggregated nano crystals in sizes between 50 and 100 nm were obtained at faster CO_2 injection rates. As shown from the XRD patterns in Figure 4.50, all precipitates obtained at the end of each CO_2 flow rates were calcite.
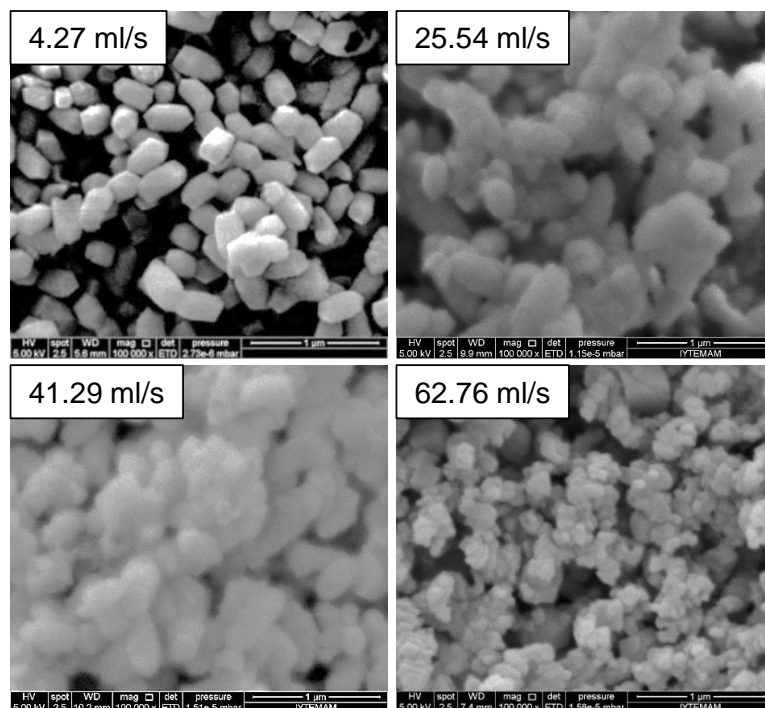
Figure 4.49. SEM images of CaCO₃ particles at different CO₂ flow rates (Scale: 1 μm).
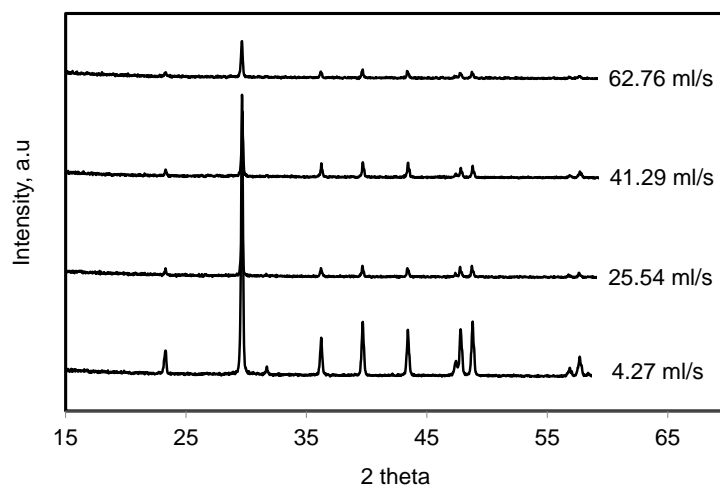
Figure 4.50. XRD patterns of CaCO₃ particles obtained for different CO₂ flow rates at the end of the crystallization.

4.4.4. Effect of Ca(OH)₂ Concentration

Effects of Ca(OH)₂ concentration on the CaCO₃ crystallization were studied. CaCO₃ solution up to 20 mM and Ca(OH)₂ slurries up to 100 mM were prepared. Keeping the crystallization conditions unchanged, any effect of Ca(OH)₂ concentration on CaCO₃ crystallization were determined. Figure 4.51 shows pH and conductivity

values for different $Ca(OH)_2$ solution and slurries during the $CaCO_3$ crystallization. As shown in the figure, the conductivity values decreased almost linearly for 5, 10, 15, and 20 mM of $Ca(OH)_2$ solutions. On the other hand, the conductivity values were almost uncharged for 30, 50, and 100 mM of $Ca(OH)_2$ slurry initially and after a while decreased at similar fashion. The solubility of $Ca(OH)_2$ has been reported as 0.185 g/100 ml at 25^oC, which is about 25 mM (Windholz et al., 1976). Therefore, 5, 10, 15, and 20 mM of $Ca(OH)_2$ solution were classified as below the solubility limit, and 30, 50, and 100 mM of $Ca(OH)_2$ were grouped as above the solubility limit. At higher $Ca(OH)_2$ concentrations, crystallization took place in the $Ca(OH)_2$ slurry. However, any Ca^{++} and OH^- ions consumed during the crystallization were supplied from the undissolved $Ca(OH)_2$ particles at high $Ca(OH)_2$ slurry. When $Ca(OH)_2$ powders were dissolved completely, the conductivity started to decrease in significant amount. Therefore, the second linear decrease was started when the dissolution of $Ca(OH)_2$ was completed. A stable decrease in conductivity indicates that the slow step in $CaCO_3$ crystallization is the CO_2 dissolution rate rather than neither $Ca(OH)_2$ dissolution rate nor $CaCO_3$ crystallization rate.

Figure 4.51 shows also the calculated $[OH^-]$ and $[Ca^{++}]$ concentrations during the $CaCO_3$ crystallization at different $Ca(OH)_2$ concentrations. When the dissolution of various $Ca(OH)_2$ concentration was completed before the CO_2 injection, the Ca^{++} ion concentrations were found to be about 4.3, 8.0, 12.6, and 14.9 mM at higher $Ca(OH)_2$ concentrations, and the hydroxide ion concentration for 5, 10, 15, 20 mM of $Ca(OH)_2$ solutions were found to be about 10.2, 19.9, 22.9, and 29.5 mM, respectively. The $[OH^-]$ for 30, 50, and 100 mM were found to be about 33 mM. Comparing the calculated Ca^{++} and OH^- ion concentrations, there seemed to be some loss in OH^- as well as Ca^{++} ions, which could be due to the formation of some cluster in between, forming new particles, or adsorbed on the particles present in the solution.
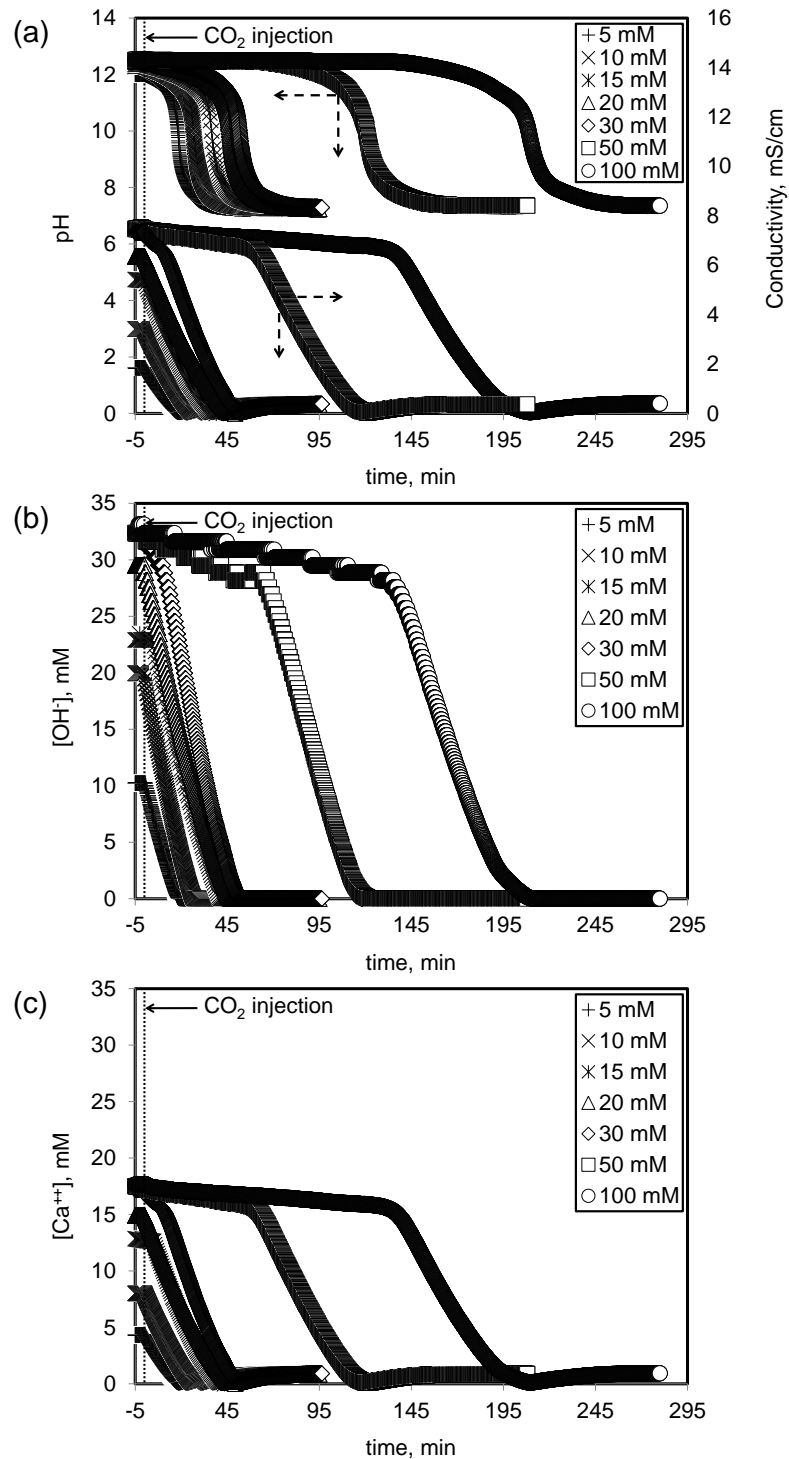
Figure 4.51. (a) pH, and conductivity values, (b) calculated $[OH^-]$ and (c) $[Ca^{++}]$ ion concentrations during the $CaCO_3$ crystallization at different $Ca(OH)_2$ concentrations.

Figure 4.52 shows calculated $[OH^-]$, and $[Ca^{++}]$ concentrations for 100 mM of $Ca(OH)_2$ slurry, and their consumption rates during $CaCO_3$ crystallization. As shown in the figure, $[OH^-]$ and $[Ca^{++}]$ concentrations decreased slowly due to the undissolved $Ca(OH)_2$ powders in the 100 mM of $Ca(OH)_2$ slurry. Upon CO_2 addition, the $CaCO_3$

crystallization consumed all the Ca^{++} and OH^- ions, and in the meantime, additional Ca^{++} and OH^- ions were generated from the undissolved $Ca(OH)_2$ chunks in the slurry. Therefore, a slight decrease was seen in this initial step of crystallization at higher $Ca(OH)_2$ slurry. When undissolved $Ca(OH)_2$ powders were dissolved completely, a decrease in both $[OH^-]$ and $[Ca^{++}]$ concentrations were seen to occur sharply. The consumption rates were slight at the beginning and the rate were higher for the late stage of crystallization when $Ca(OH)_2$ particles were completely dissolved.
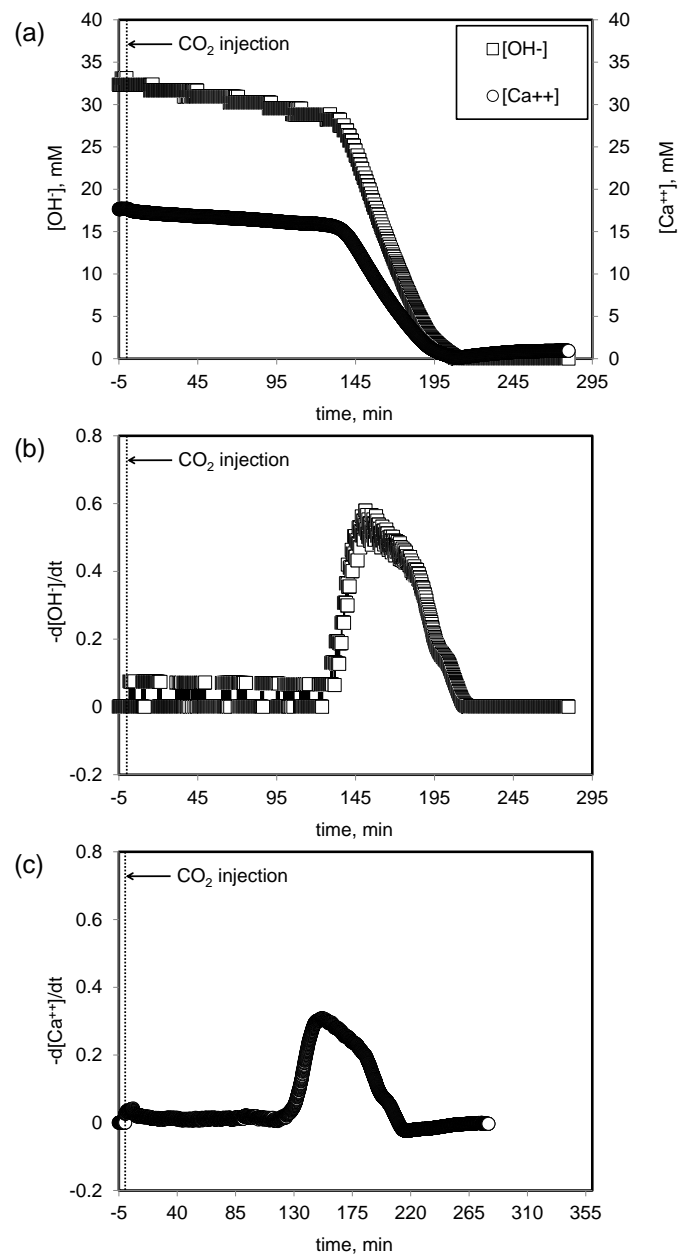
Figure 4.52. (a) Calculated $[OH^-]$, and $[Ca^{++}]$ concentrations, and (b) and (c) their consumption rates for a 100 mM of $Ca(OH)_2$.

Figure 4.53 shows the zeta potential and average particle size for different $Ca(OH)_2$ concentrations. As shown in the figure, the zeta potential of 5 mM $Ca(OH)_2$ solution was found to be about -10 mV. As mentioned before, it was reported that the $CaCO_3$ surface is negatively charged at higher pH's (10<pH) (Fenter et al., 2000). In addition, 5 mM $Ca(OH)_2$ solution was below the solubility limit. At this concentration, there may not be enough Ca^{++} ions adsorbing on the $CaCO_3$ surfaces in the aqueous solution. Therefore, the surface of $CaCO_3$ particles was covered partially by Ca^{++} ions. The zeta potentials of 5 mM solution changed from about -10 mV to +35 mV during the crystallization. The zeta potential values for other concentrations were nearly the same starting at about 30 mV. When CO_2 was injected into the reaction chamber, Ca^{++} ions were consumed during $CaCO_3$ synthesis. After the near zero conductivity, the increase in charged species due to the CO_2 dissolution as well as Ca^{++} ions as a result of the re-dissolution of $CaCO_3$ may affect the increase in zeta potential. The zeta potential of 20, 30, and 50 mM showed the similar behavior. The increases in the zeta potential for 20, 30, and 50 mM $Ca(OH)_2$ solution and slurries could be related to the undissolved $Ca(OH)_2$ particles existing in the $Ca(OH)_2$ solution. The zeta potential of 20 and 30 mM increased when CO_2 was fed into the reaction chamber, indicating the formation of new $CaCO_3$ particles. As shown in the figure, average particle size increased during crystallization for concentrations below the solubility limit. The average particle size for 5 mM was larger, and the average particle size decreased by increasing the $Ca(OH)_2$ concentration up to 15 mM. The average particle size obtained for 15 mM varied from about 200 to 400 nm. The average particle size for the 20 mM solution was in the range from 300 to 500 nm. The average particle size for the 30 mM solution was about 1 μm, and the average particle size for the 50 and 100 mM $Ca(OH)_2$ slurries were above the micron sizes.
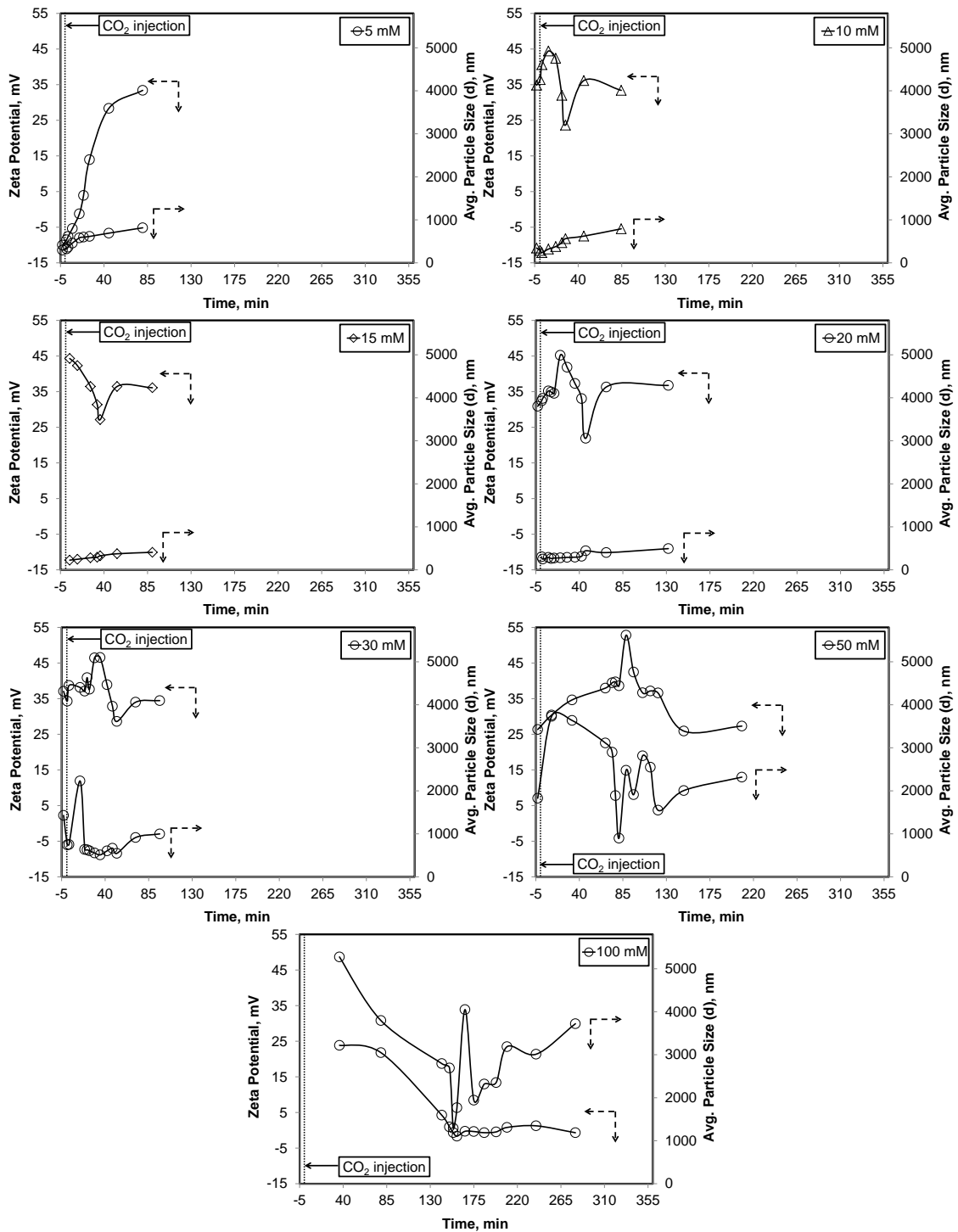
Figure 4.53. Zeta potential and average particle size for different $Ca(OH)_2$ concentrations.

Figure 4.54 shows average particle size obtained at the end of the crystallization for the different $Ca(OH)_2$ concentrations. As shown in the figure, U-type curve was obtained for average particle size for different $Ca(OH)_2$ concentrations. The smallest average particle size could be obtained at 15 mM, which was slightly below the solubility limit. When the concentration was lower, the average particle size would be

higher. When the $Ca(OH)_2$ concentration was higher than the solubility limit, the particle size became bigger.
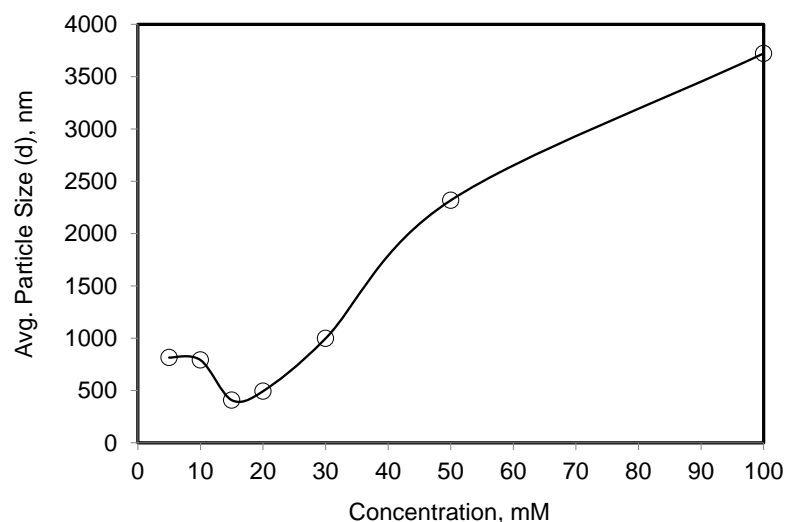
Figure 4.54. Change of average size of $CaCO_3$ with $Ca(OH)_2$ concentrations obtained at the end of the each $Ca(OH)_2$ concentration experiments.

SEM images of $CaCO_3$ particles obtained from a 100 mM of $Ca(OH)_2$ slurry were shown in Figure 4.55. As shown in the figure, scalenohedral $CaCO_3$ crystals were obtained for a 100 mM of $Ca(OH)_2$ slurry. The particle sizes during $CaCO_3$ synthesis were larger than micron sizes. Small particles were also synthesized at the beginning of crystallization. Aggregation of particles was also seen. Figure 4.56 shows the XRD patterns of particles obtained during $CaCO_3$ crystallization. As shown in the figure, the unconverted $Ca(OH)_2$ powders were also obtained at the beginning of crystallization. After the initial step, scalenohedral calcite particles were shown to be synthesized.
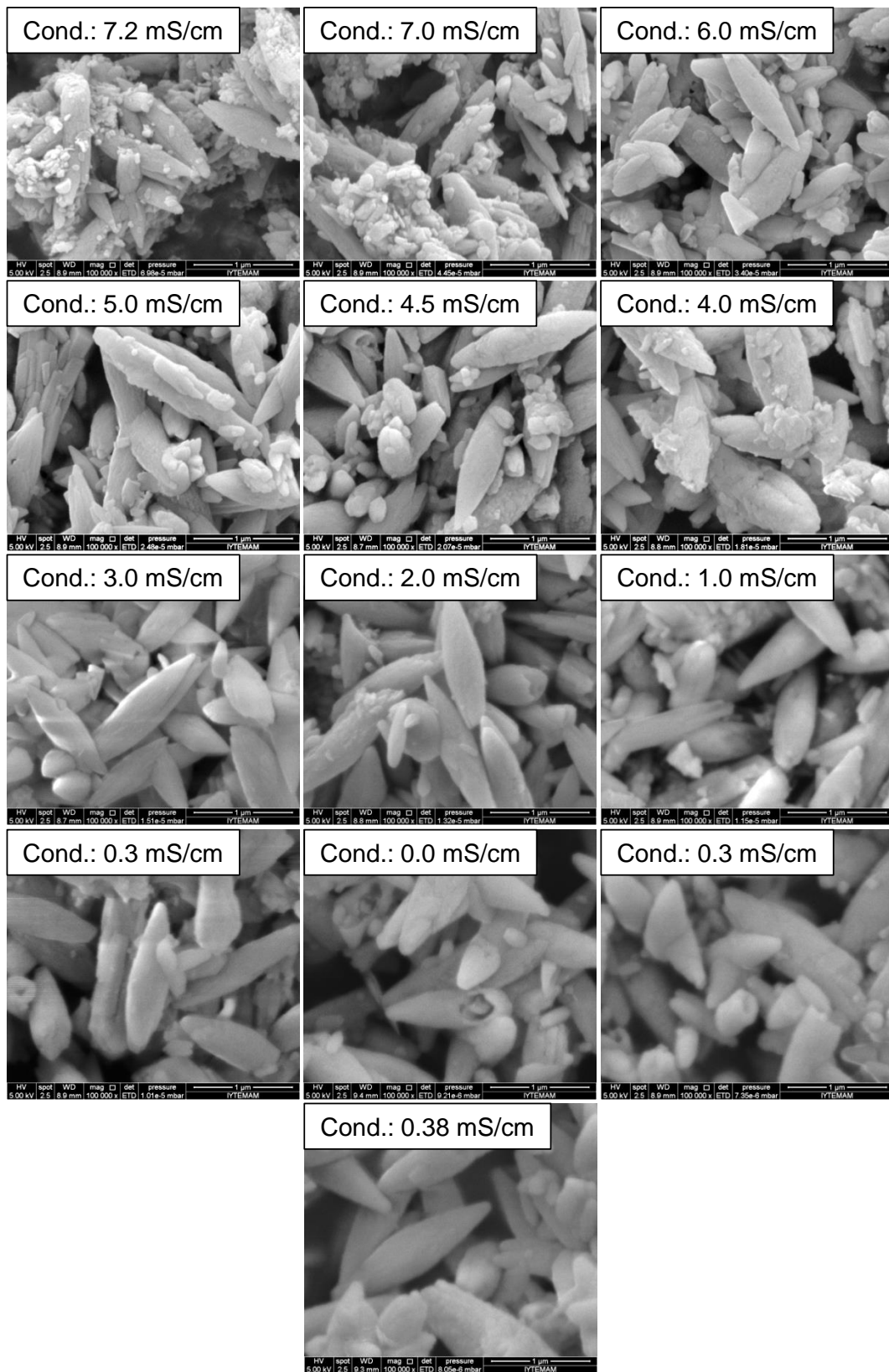
Figure 4.55. SEM images of CaCO$_3$ particles obtained for 100 mM of Ca(OH)$_2$ slurry (Scale: 1 μm).
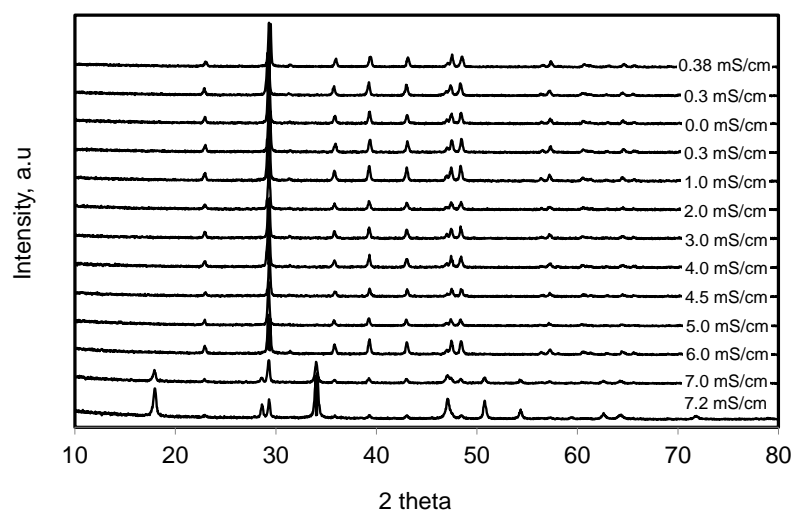
Figure 4.56. XRD patterns of $CaCO_3$ particles obtained from a 100 mM of $Ca(OH)_2$ slurry.

Figure 4.57 shows the SEM images of $CaCO_3$ particles produced from different $Ca(OH)_2$ concentrations. As shown in the figure, industrial and larger rhomboscalenohedral calcite particles were obtained in the 5 and 10 mM of $Ca(OH)_2$ solutions. Rhombohedral nano $CaCO_3$ particles were produced in the 15 mM of $Ca(OH)_2$ solution, which were the smallest $CaCO_3$ particles. Scalenohedral and rhombohedral $CaCO_3$ particles were obtained in the presence of 20 mM, and higher concentration of $Ca(OH)_2$, where the particles looks larger and also aggregated. All of these particles were found to be calcite as evidenced from their XRD patterns as shown in Figure 4.58.
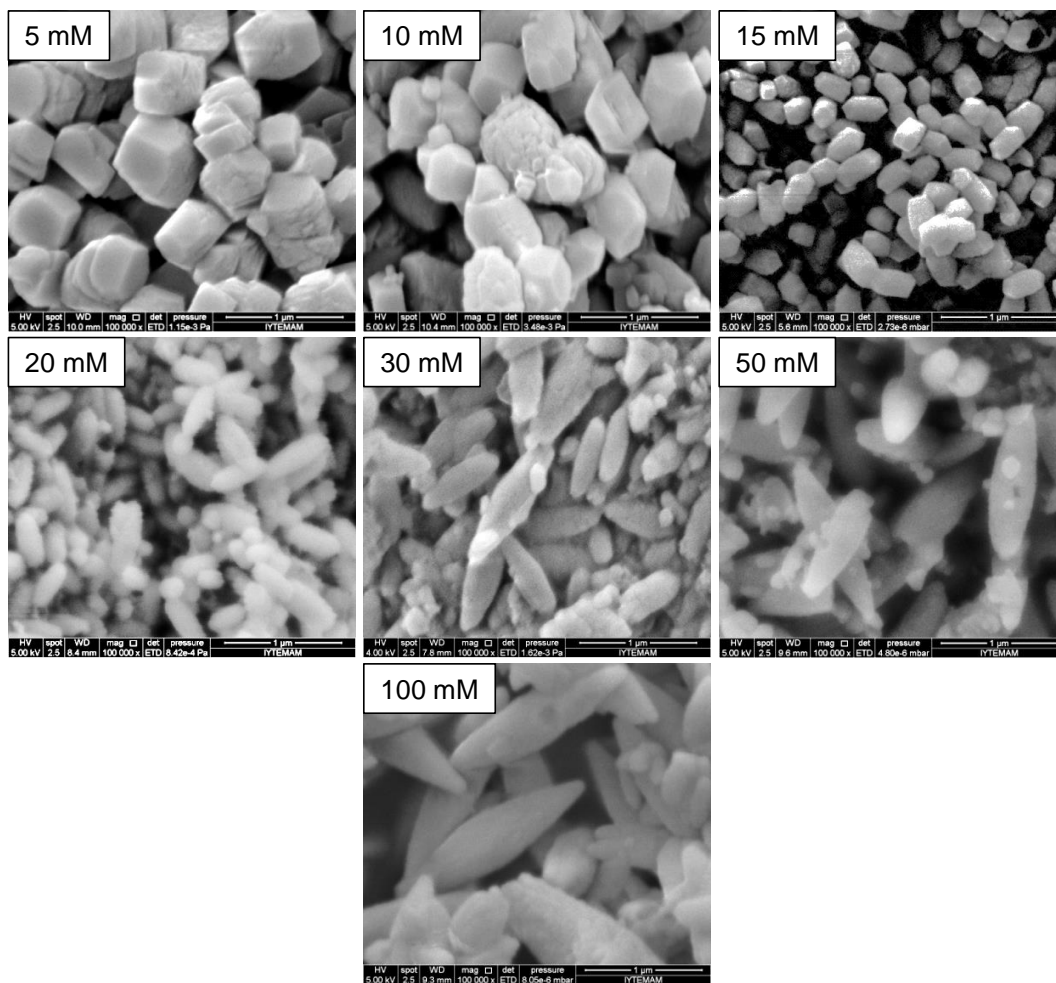
Figure 4.57. SEM images of the CaCO$_3$ particles obtained in different Ca(OH)$_2$ concentrations (Scale: 1 μm).
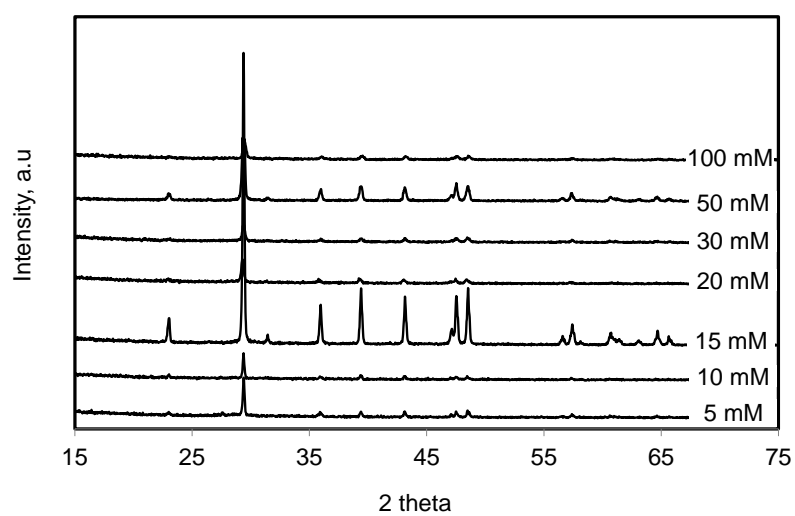
Figure 4.58. XRD patterns of CaCO$_3$ crystals obtained in different Ca(OH)$_2$ concentrations.

4.4.5. Effect of Stabilization Tank Volume

As proposed in Eq.(3.4), and Eq.(4.5), the consumption rate of [Ca^{++}] and [OH$^-$] is proportional to the stabilization tank volume. On the other hand, it was reported that the crystallization of aragonite particles was accelerated and the amount of agglomerated fine particles of calcite decrease with the increased of the solution volume (Kitamura et al., 2002).

A mass balance can be conducted around the stabilization tank and the reaction chamber as shown in Figure 4.59. Mass balance around stabilization tank can be expressed as:

$$QC_{Ao} - QC_{Ai} = \frac{\partial (V_T C_{Ai})}{\partial t} \tag{4.3}$$

where Q is the liquid phase flow rate, V_T is the stabilization tank volume, C_{Ao} and C_{Ai} are outlet and inlet concentrations at the stabilization tank, respectively. Since there is no gas phase CO_2 in the stabilization tank, crystallization does not occur in the stabilization tank. Then, mass balance around reaction chamber can be written as:

$$QC_{Ai} - QC_{Ao} - R = 0 \tag{4.4}$$

where R is the consumption rate of Ca^{++} and OH$^-$ ions in the reaction chamber in mole/min. Eq.(4.5) can be obtained by inserting Eq.(4.4) into Eq.(4.3). Therefore, the consumption rate of Ca^{++} or OH$^-$ ions in the reaction chamber can be expressed as:

$$R = -V_T \frac{\partial C_{Ai}}{\partial t} \tag{4.5}$$

As given in Eq.(4.5), the conversion rate of Ca^{++} and OH$^-$ ions in the reaction chamber is proportional to the stabilization tank volume and the change in concentration in the stabilization tank. On the other hand, CO_2 diffusion from the gas phase into the liquid phase in the reaction chamber may be thought as a slow step in the $CaCO_3$ crystallization. In this case, the conversion rates for Ca^{++} and OH$^-$ ions cannot be bigger

than the diffusion rate of CO_2 from the gas phase into the liquid phase. Therefore, CO_2 diffusion rate, as shown in Eq.(3.4), could be estimated from the conversion rates of Ca^{++} and OH^- ions.
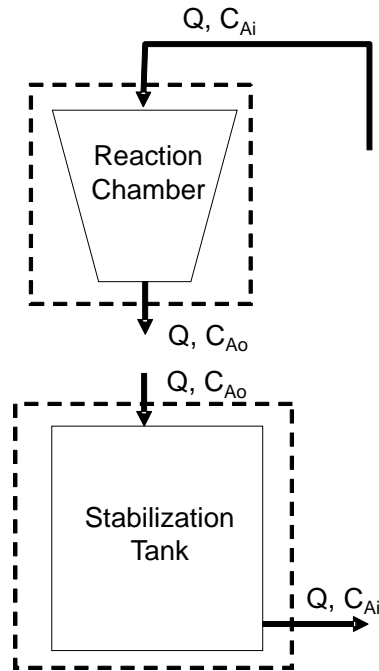
Figure 4.59. Mass balances around reaction chamber and stabilization tank.

Figure 4.60 shows pH and conductivity values for different tank volumes. The calculated Ca^{++} and OH^- ion concentrations were also depicted in the figure. As shown in the figure, the conductivity for each tank volume decreased almost linearly when CO_2 was injected into the reaction chamber. Moreover, the consumption time of ions increased with increasing the tank volume. As shown in the figure, the consumption time for the $[OH^-]$ and $[Ca^{++}]$ ion concentrations were increased when the tank volume was increased, indicating that CO_2 dissolution rate is constant but the consumption rate for Ca^{++} and OH^- ions were smaller for larger tank volumes whereas the consumption rate was higher for smaller tank volumes. Moreover, the linear decrease in $[OH^-]$ ions could be related to the constant CO_2 dissolution rate in the reaction chamber. The multiplication of the consumption rates with the tank volume should result in the same value, which indicates the constant CO_2 dissolution rate in the reaction chamber. As shown in Figure 4.61, really there is a linear relationship between the tank volume and the Ca^{++} and OH^- consumption rates.
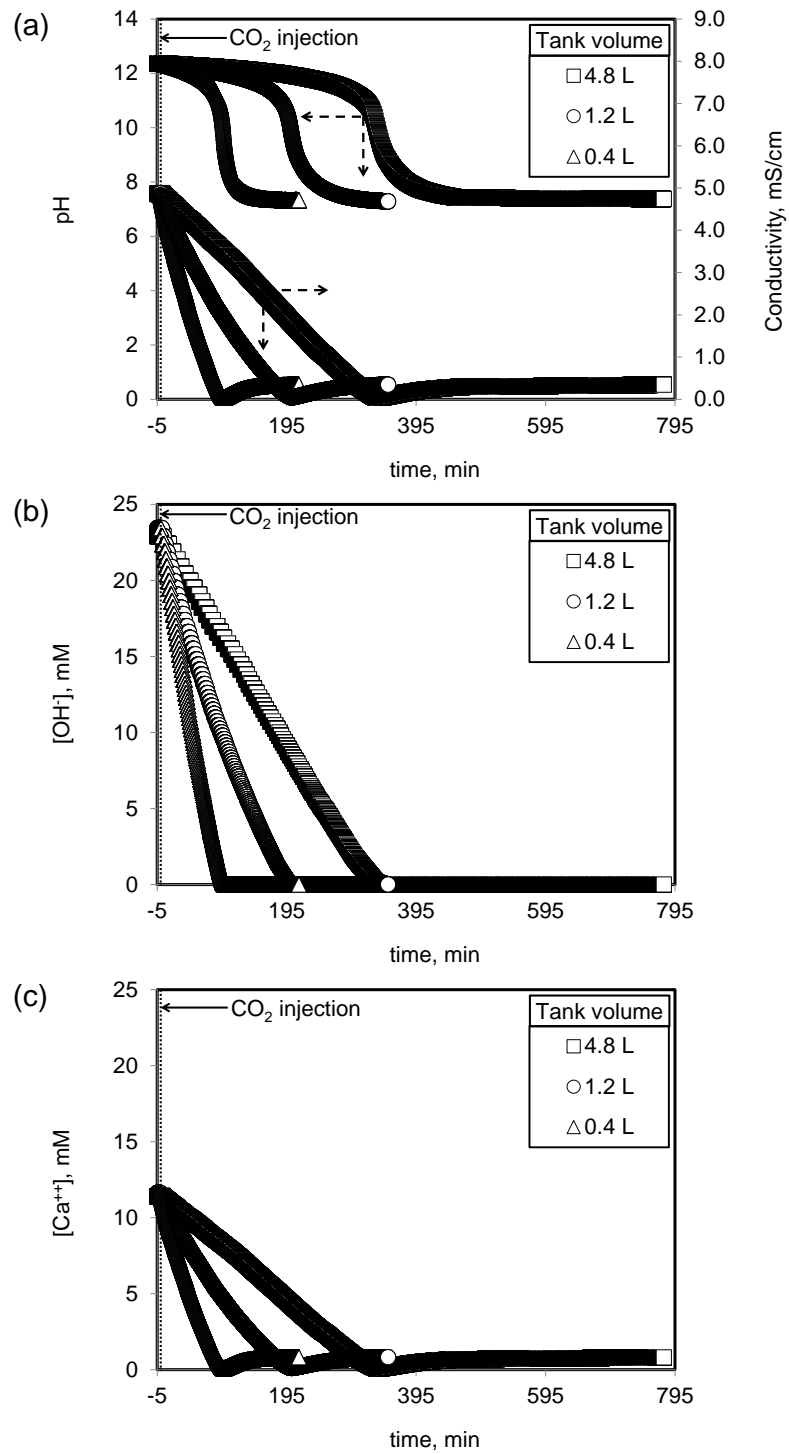
Figure 4.60. (a) pH and conductivity values, and (b) calculated OH⁻ and (c) Ca⁺⁺ concentrations for stabilization tank volume.
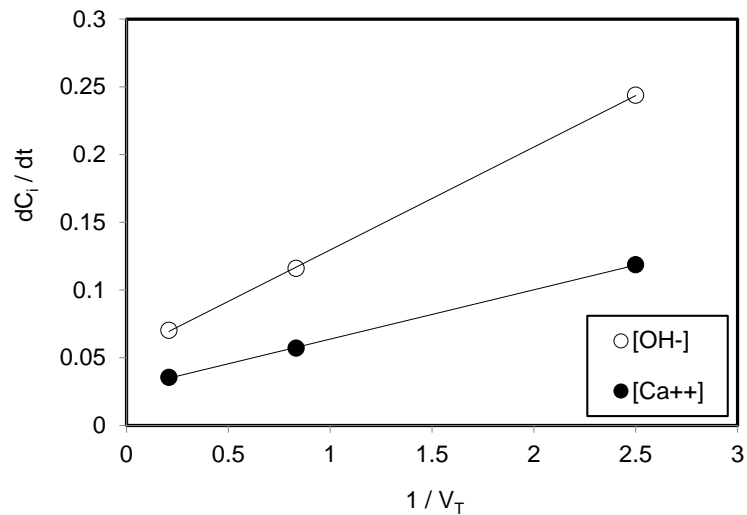
Figure 4.61. Consumption rate of Ca^{++} and OH^- ion concentrations.

The calculated $[OH^-]$ and $[Ca^{++}]$ concentrations and their consumption rates for a 4.8 L tank volume were shown in Figure 4.62. As shown in the figure, a linear decrease in both $[OH^-]$ and $[Ca^{++}]$ concentrations were obtained. The consumption rate for both ion concentrations increased sharply when the CO_2 was fed into the reaction chamber. Then, the consumption rates stayed high for a long time, and oscillated especially for the OH^- ions. The oscillation in the consumption rates may indicate that the crystallization may be a dynamic process.

Figure 4.63 shows the zeta potential and average particle size during the $CaCO_3$ crystallization for different tank volumes. As shown in the figure, the zeta potential values over the reaction increased when the tank volume increased, since the CO_2 was dissolved within 15 mM $Ca(OH)_2$ solution in a controllable fashion. Moreover, the change in the average particle size was smaller for the biggest tank volume.
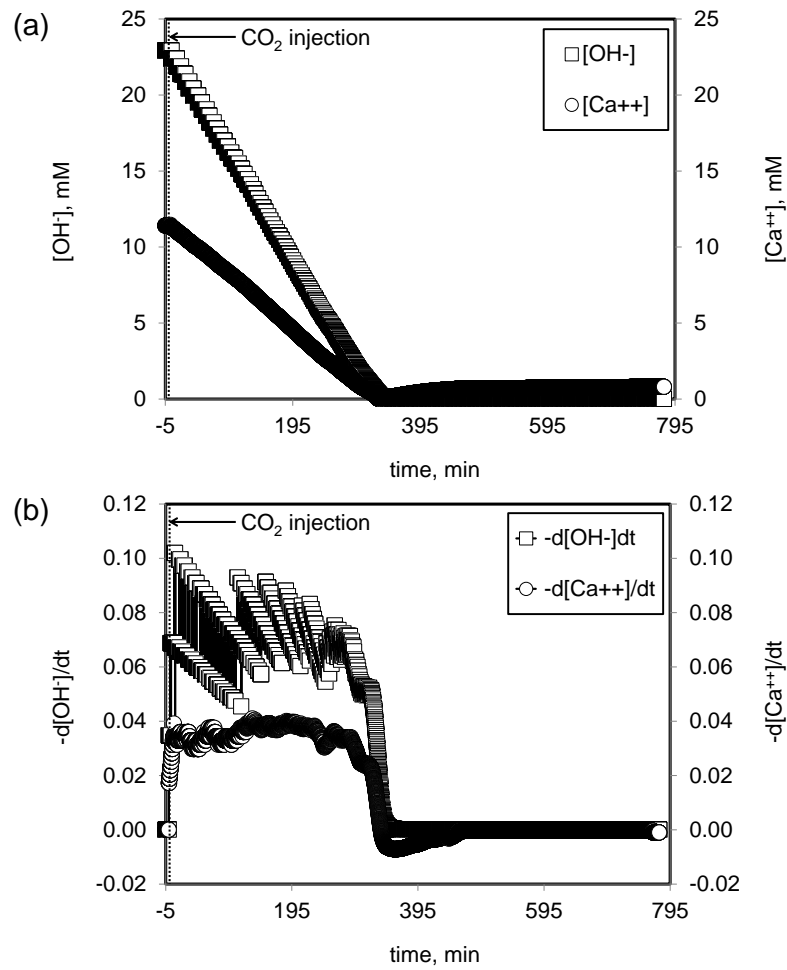
Figure 4.62. (a) [OH⁻], and [Ca⁺⁺] concentrations, and (b) their consumption rates obtained for a 4.8 L tank volume.
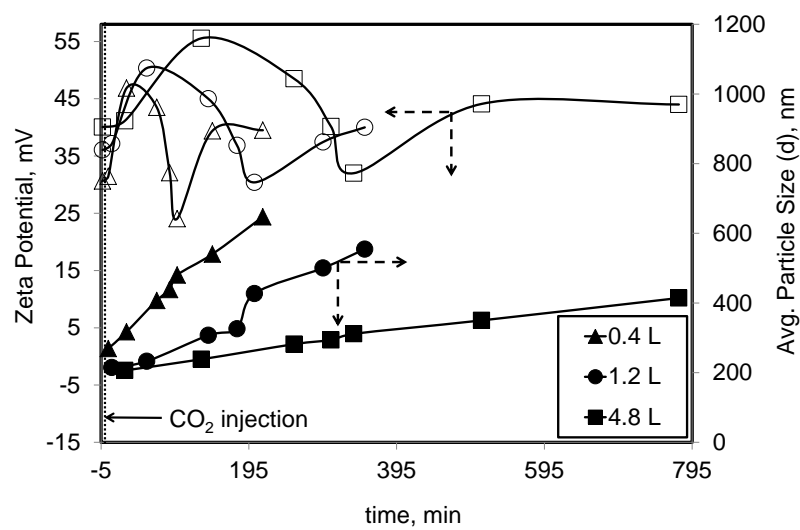
Figure 4.63. The zeta potential and average particle size for different tank volumes over the reaction.

93

The SEM images of CaCO$_3$ particles obtained from a larger stabilization tank volume of 4.8 L were given in Figure 4.64. Rice-like submicron particles and rhombohedral crystals were obtained at the beginning of the reaction. Then, the length of rice-like particles started to decrease when the conductivity reached to 3.0 mS/cm. The homogenization of average particle sizes was begun at about 0.3 mS/cm. It was expected that the formation of hollow particles started when the conductivity of the solution reached to 0.3 mS/cm as depicted in small penetration method. However, hollow particles were partially obtained at about zero conductivity. Since the crystallization time was shorter for the 4.8 L tank volume, hollow particles were produced partially At the end of the crystallization, monodisperse CaCO$_3$ crystals were obtained with a size of about 200 nm.
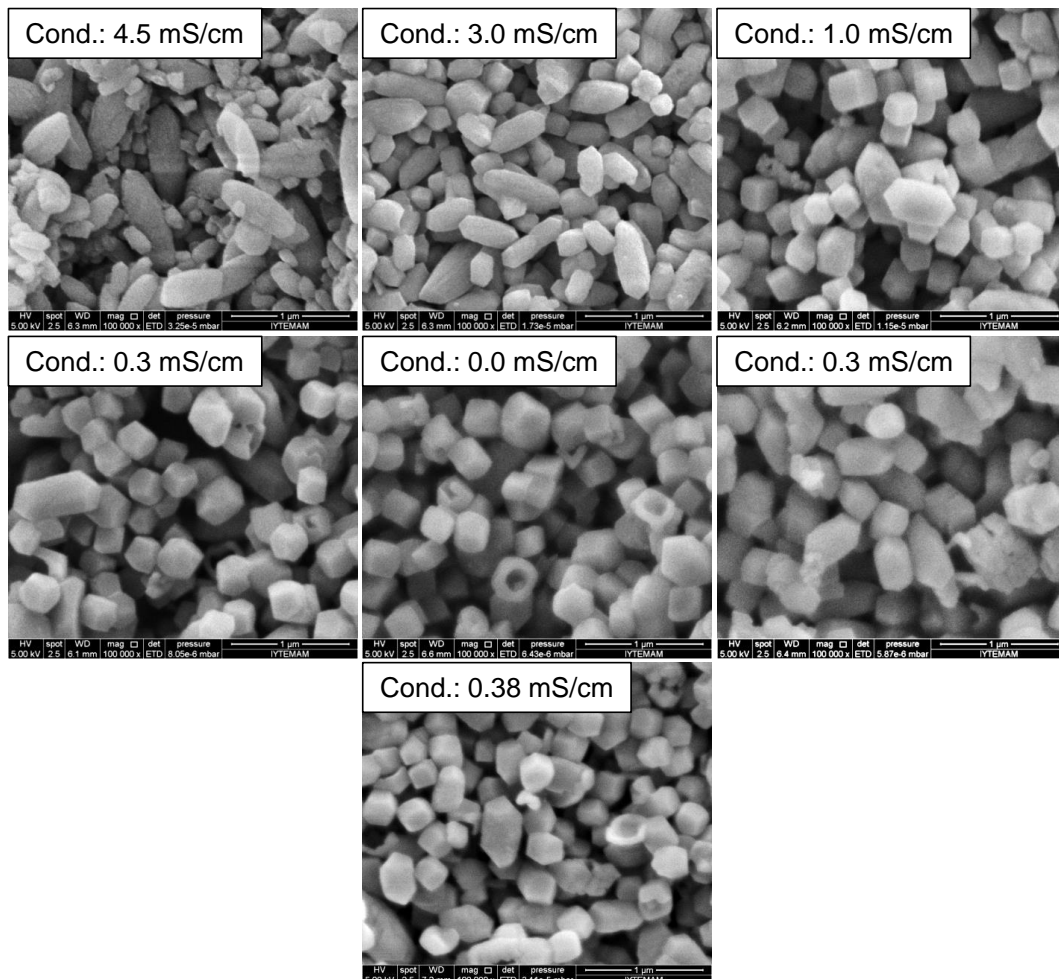
Figure 4.64. SEM images of CaCO$_3$ particles obtained for a larger stabilization tank volume (Scale: 1 μm).

Figure 4.65 shows the SEM images of $CaCO_3$ particles produced in different tank volumes. As shown in the figure, the more homogeneous and small crystal particles were obtained when the tank volume was larger. The change in stabilization tank volume did not affect the morphology of $CaCO_3$ crystals, and as shown in the figure, rhombohedral calcite particles were obtained for each tank volume. All the $CaCO_3$ particles obtained were calcite as evidenced from the XRD patterns as shown in Figure 4.66.
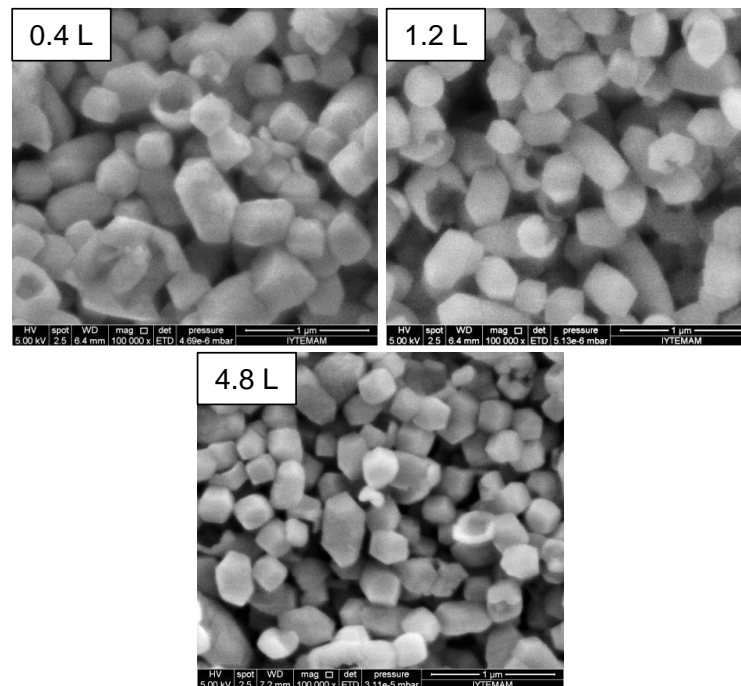
Figure 4.65. SEM images of $CaCO_3$ crystals obtained in different tank volumes (Scale: 1 μm).
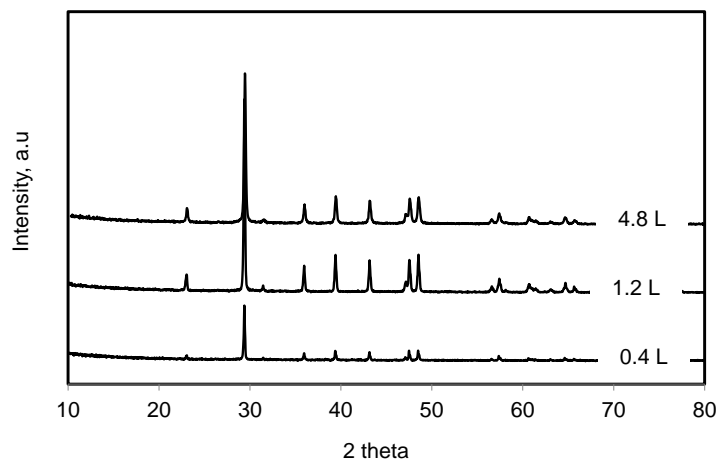
Figure 4.66. XRD patterns of particles obtained in different tank volumes.

4.4.6. Effect of Pipe Diameter

The surface area and maximum velocity of $Ca(OH)_2$ solution, which are two important factors in the determination of CO_2 dissolution rate. The maximum velocity for the liquid phase can vary with time at different pipe diameter for the $Ca(OH)_2$ solution. Figure 4.67 shows pH and conductivity values for the different pipe diameters. The calculated Ca^{++} and OH^- concentrations were also shown in the figure. As shown in the figure, the consumption of ions took shorter time when the smaller pipe diameter was used. Two different factors, the surface area of liquid phase and maximum velocity of liquid phase, may determine the CO_2 dissolution rate in the pipe diameter experiments. When the pipe diameter was decreased, the liquid velocity was increased at constant $Ca(OH)_2$ flow rate, but on the other hand, the surface area of $Ca(OH)_2$ solution was decreased. The increase in maximum velocity of the liquid phase resulted in an increase in CO_2 dissolution rate. As depicted in $Ca(OH)_2$ flow rate experiment, the time is significantly important to transport the $CaCO_3$ particles from reaction chamber into the stabilization tank for the stabilization of crystals with the Ca^{++} ions.

The zeta potential and average particle size obtained for different pipe diameter experiments were shown in Figure 4.68. As shown in the figure, the CO_2 dissolution rate was higher for the smallest pipe diameter. When $Ca(OH)_2$ velocity increased with the decrease in pipe diameter, stabilization time decreased significantly. As shown in the figure, zeta potential values showed a similar trend but this value was slightly lower when pipe diameter was decreased. The average particle size also showed similar trend for each pipe diameter.
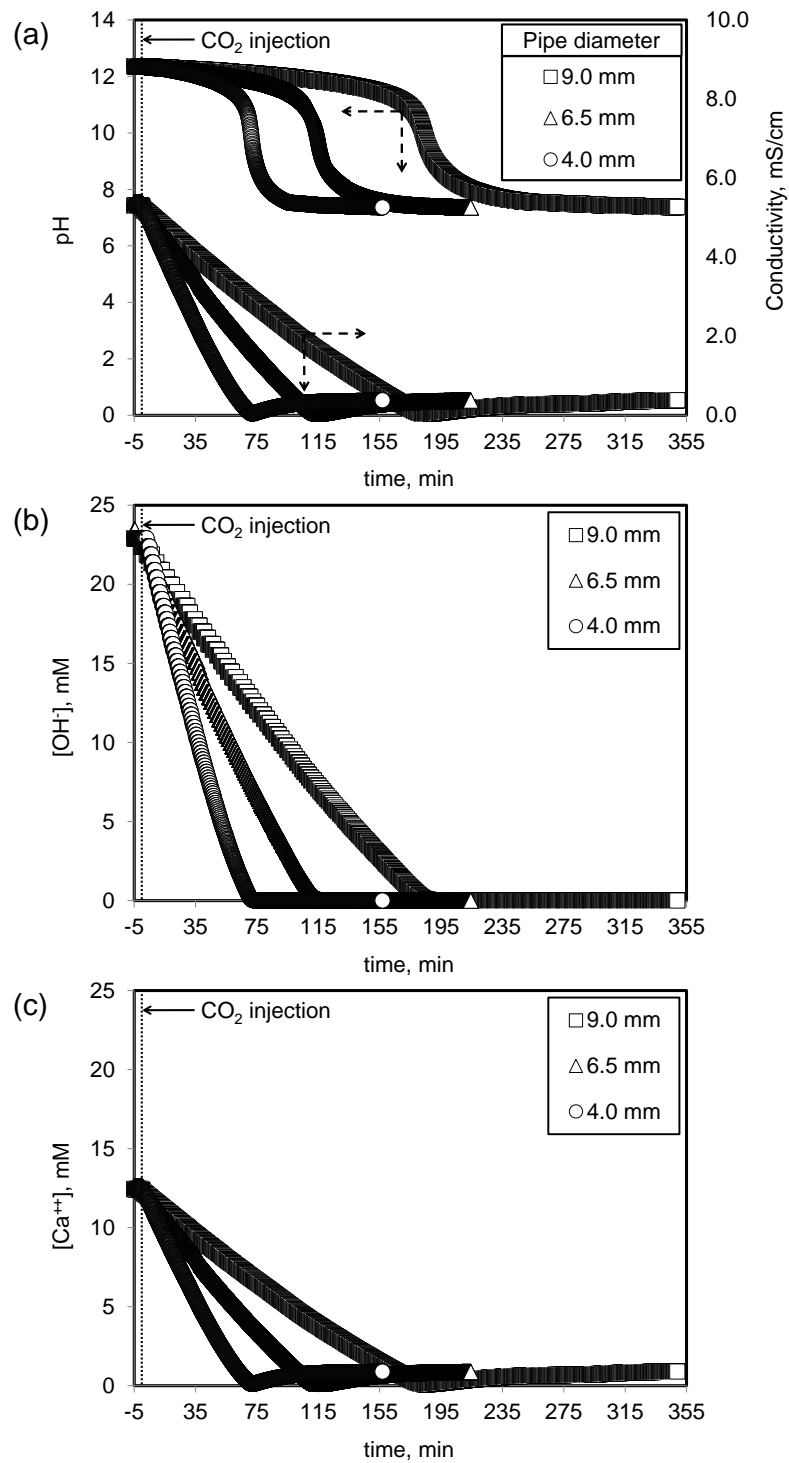
Figure 4.67. (a) pH and conductivity values and (c) calculated OH⁻ and (c) Ca⁺⁺ concentrations for different pipe diameters.
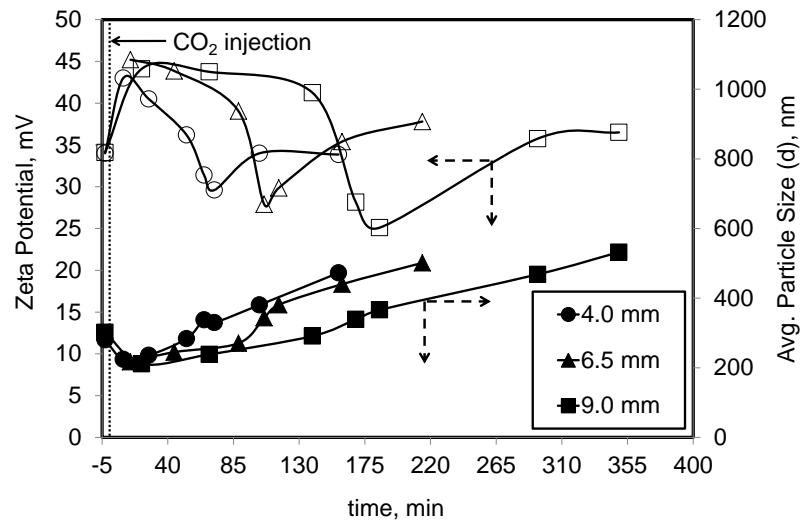
Figure 4.68. Zeta potential and average particle size for pipe diameters.

SEM images of $CaCO_3$ particle obtained for a 4.0 mm pipe diameter were shown in Figure 4.69. As shown in the figure, rice-like particles were obtained in sizes about 200 nm at the beginning of crystallization. Decrease in length and increase in the diameter of the $CaCO_3$ particles were observed, resulting in a decrease in particle size to about 100 – 150 nm. At about zero conductivity, hollow particles cannot be produced by using smallest pipe diameter. The average size of the particles was about 150 nm at the end of the crystallization. Monodisperse and homogeneous crystals were obtained when the small pipe diameter was used.
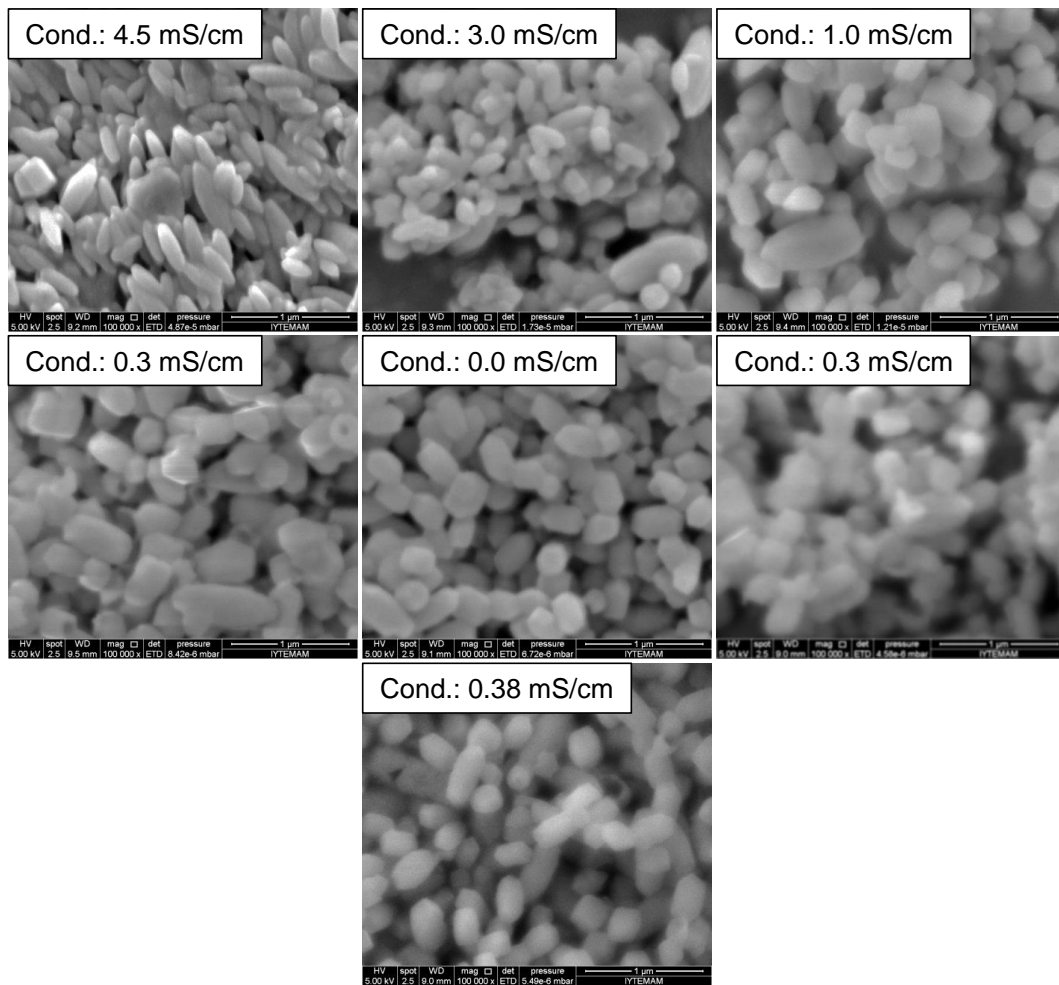
Figure 4.69. SEM images of the CaCO$_3$ particles obtained for 4.0 mm of pipe diameter
(Scale: 1 μm).

Figure 4.70 shows the SEM images of crystals obtained by using different pipe diameters. As shown in the figure, the particle size was smaller for the smaller pipe diameter. The morphology of the particles did not change with the change in the pipe diameter, and as shown in the figure, rhombohedral calcite was produced for each pipe diameter experiments at the end of crystallization. These particles were calcite as evidenced from the XRD patterns as shown in Figure 4.71.
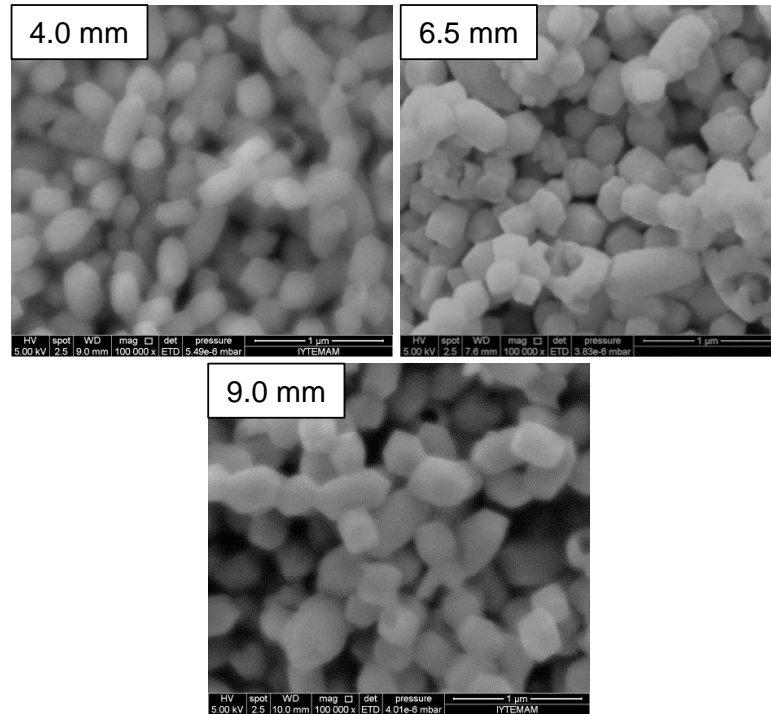
Figure 4.70. SEM images of the particles obtained by using different feeding pipe diameters (Scale: 1 μm).
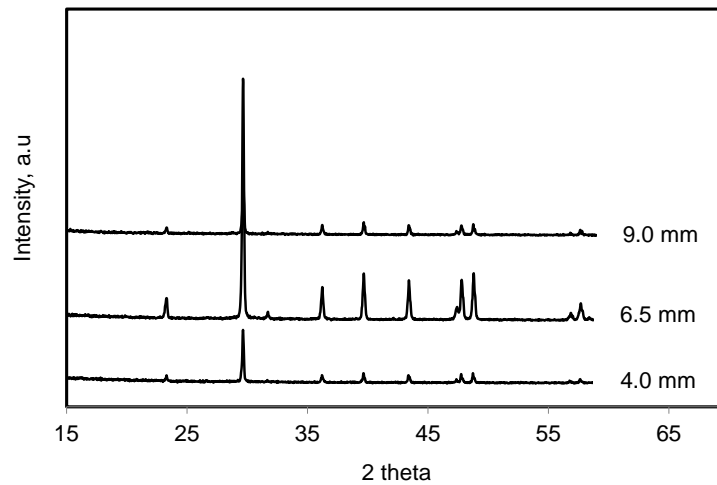
Figure 4.71. XRD patterns of $CaCO_3$ particles obtained by using different pipe diameters.

4.4.7. Effect of Length in Reaction Chamber

CO_2 dissolution rate may be controlled by varying the contact length between the liquid and gas phases. Therefore, effect of length in the reaction chamber on the $CaCO_3$ particle formation was studies. Figure 4.72 shows pH and conductivity values

for different contact lengths. The OH⁻ and Ca^{++} ion concentrations were also shown in the figure. As shown in the figure, the consumption rate was higher at higher contact lengths. As the length becomes smaller, the time to complete the crystallization was increased indicating that the CO_2 diffusion rate is proportional to the total contact area between the gas and liquid phases.
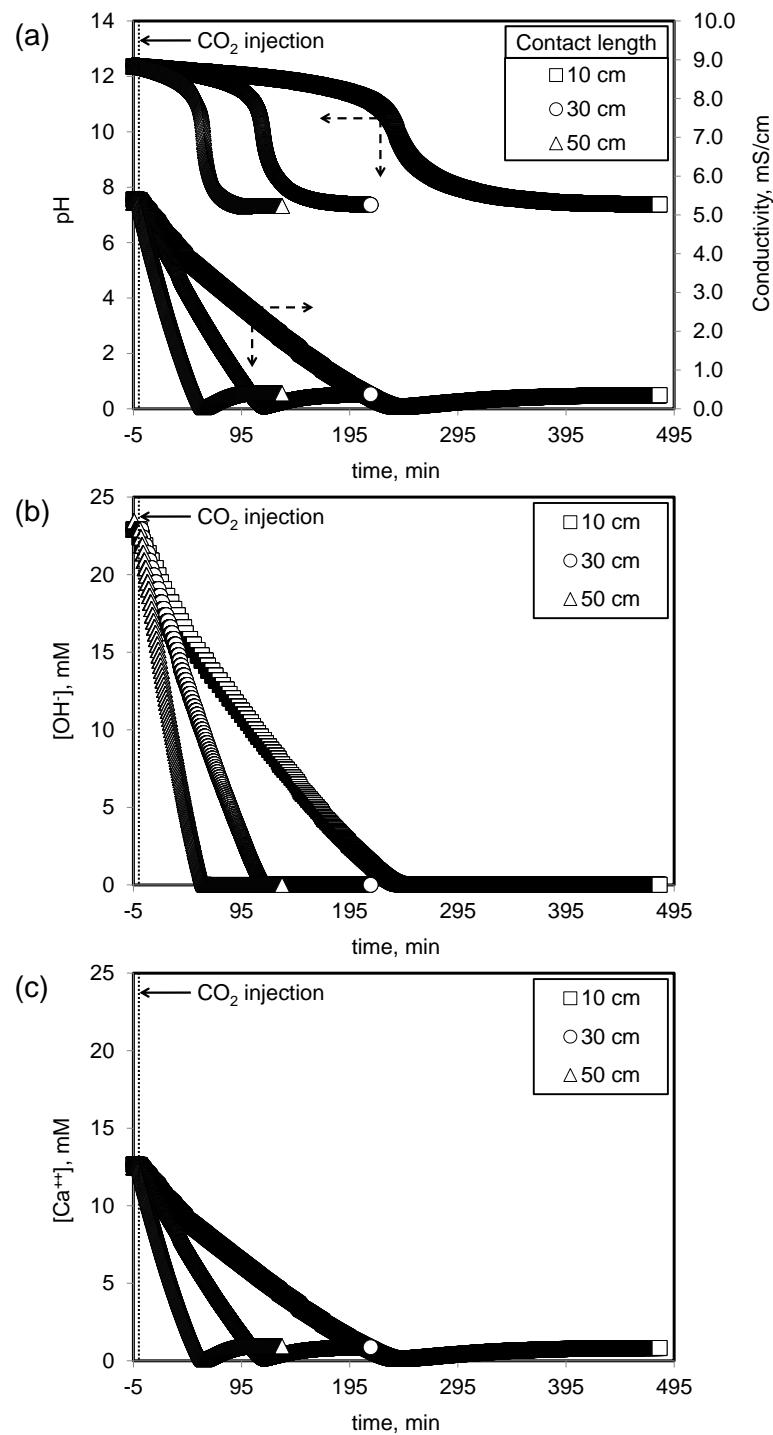
Figure 4.72. (a) pH and conductivity, and (b) calculated OH⁻ and (c) Ca^{++} ion concentrations obtained for different contact lengths.

Figure 4.73 shows the zeta potential and average particle size for different length experiments. As shown in the figure, the zeta potential and average particle size for each length showed similar trend. However, the particle size was slightly smaller for the shorter lengths than that for the longer lengths.
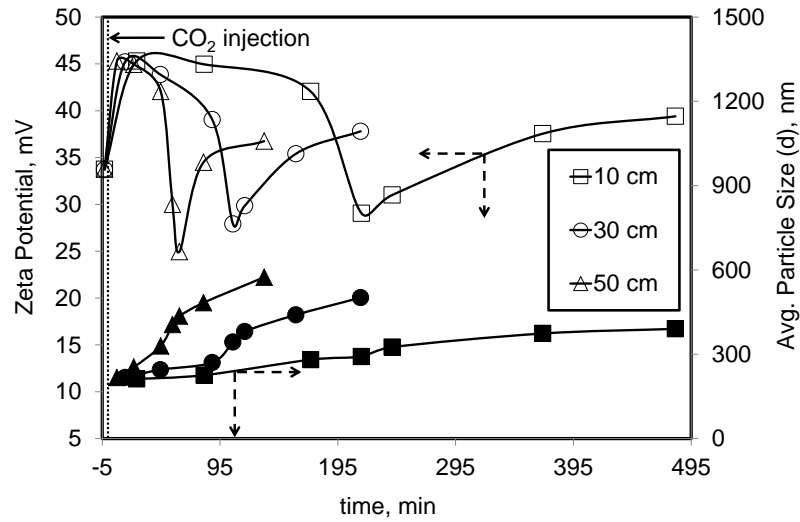
Figure 4.73. Zeta potential and average $CaCO_3$ size for different contact lengths.

SEM images of $CaCO_3$ particles obtained for a 30 cm of contact length were shown in Figure 4.74. As shown in the figure, rice-like and rhombohedral particles were produced at the beginning of the $CaCO_3$ crystallization. Hollow $CaCO_3$ particles were obtained at about zero conductivity. Solid $CaCO_3$ particles of about 200 nm were obtained at the end of the crystallization.
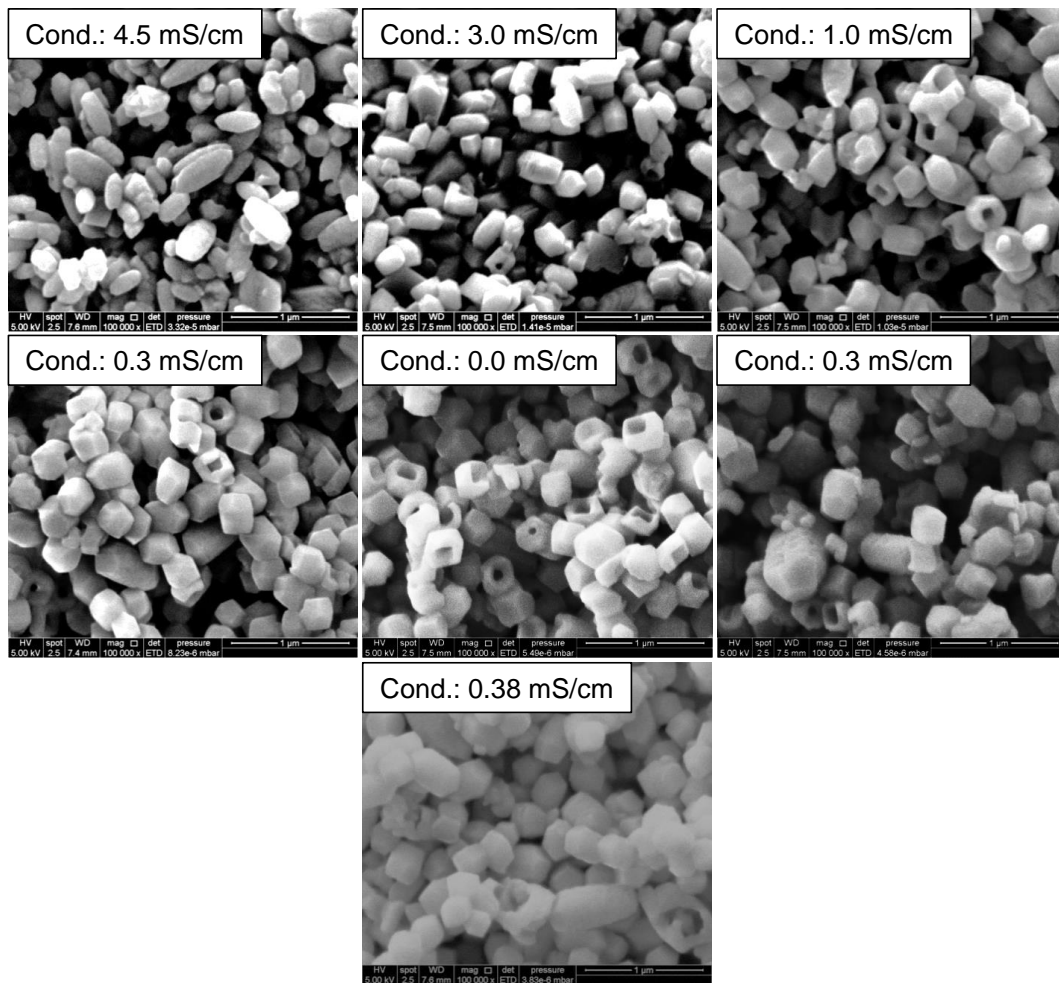
Figure 4.74. SEM images of CaCO$_3$ precipitates obtained at various conductivity for 30 cm contact length (Scale: 1 μm).

Figure 4.75 shows the SEM images of CaCO$_3$ particles obtained by using different length in the crystallization chamber. As shown in the figure, the particle size increased when the length was increased indicating that particle size increases with the increase in CO$_2$ dissolution rate and particles produced at shorter contact lengths were from 75 to 300 nm, and for longer contact lengths, they were about 600 nm. All the diffraction peaks belonging to particles were indexed to the calcite polymorph of CaCO$_3$ as shown in Figure 4.76.
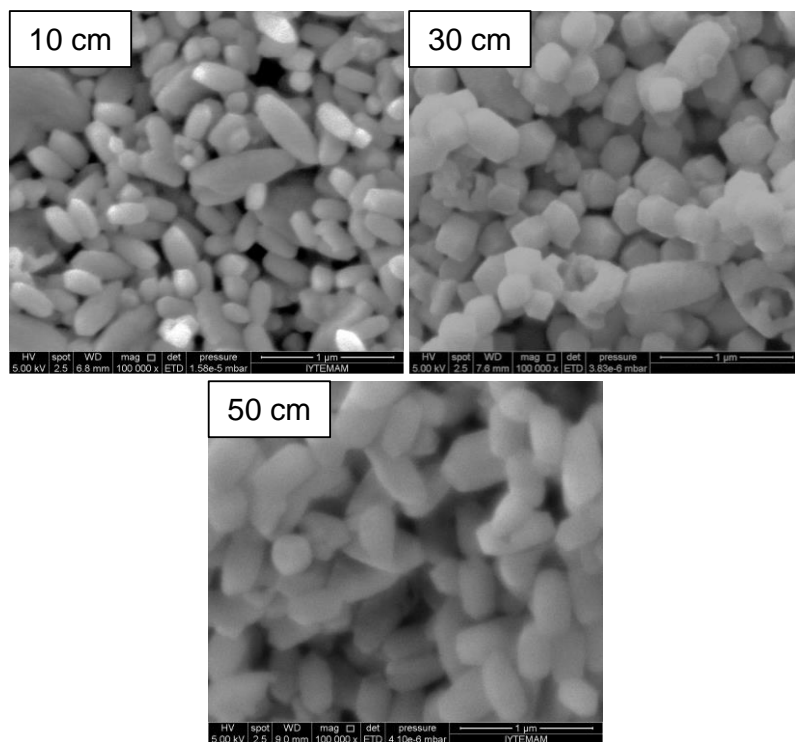
Figure 4.75. SEM images of the particles obtained during the crystallization for different contact lengths in the reaction chamber (Scale: 1 μm).
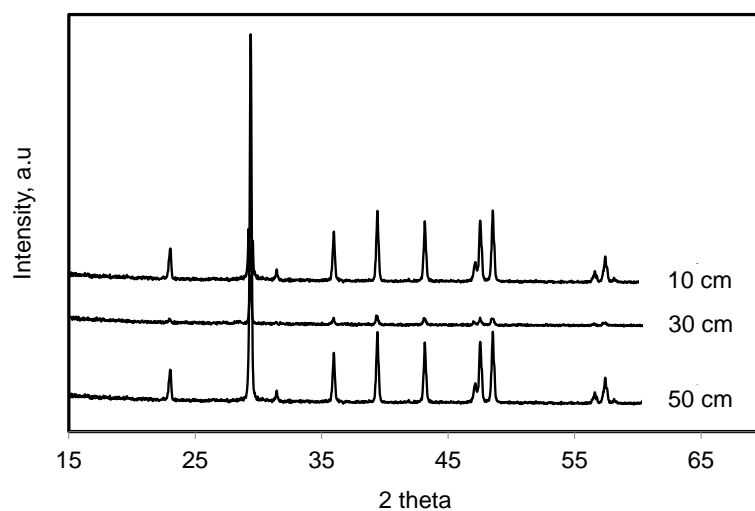
Figure 4.76. XRD patterns of the $CaCO_3$ crystals obtained at the end of each contact length experiment.

4.4.8. Effect of CO_2 Percentage

CO_2 dissolution rate may vary with the different CO_2 compositions in the gas phase. It was expected that the more CO_2 introduction into the liquid phases, the larger

the particle size to get. Therefore, different CO_2 composition could be used to reduce the CO_2 dissolution rate.

Figure 4.77 shows the pH and conductivity values for different CO_2 composition during $CaCO_3$ crystallization. The calculated Ca^{++} and OH^- concentration were also shown in the figure. As shown in the figure, the dissolution rate of CO_2 is slower at lower percentages of CO_2. The consumption time increased when the lower CO_2 percentage was used in the developed small penetration method.
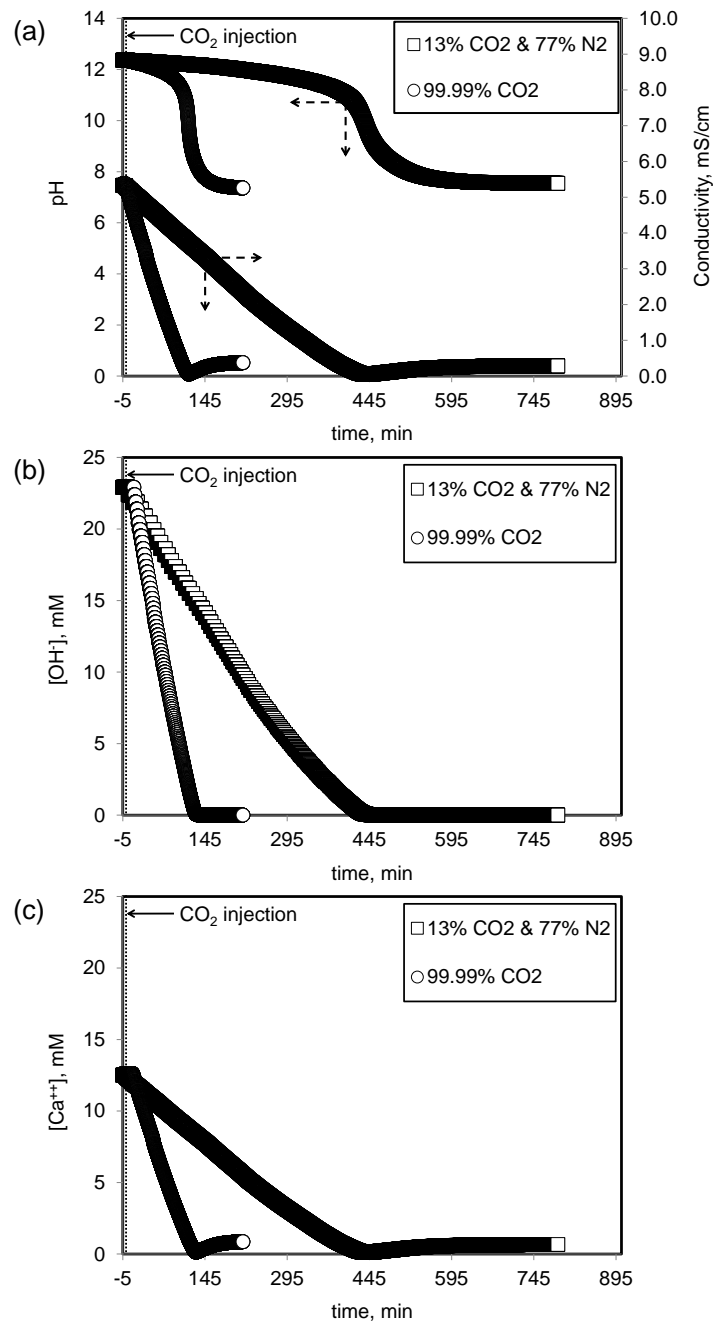
Figure 4.77. (a) pH and conductivity values, and (b) OH^- and (c) Ca^{++} ion concentrations obtained for different CO_2 composition.

Figure 4.78 shows the zeta potential and average particle size values for the CO_2 percentage experiments. As shown in the figure, the average particle sizes were smaller when lower percentage of CO_2 was used in crystallization.
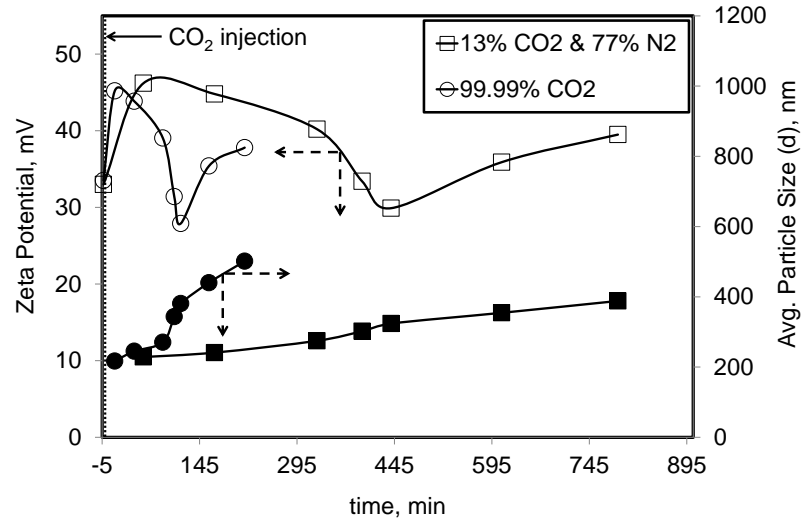
Figure 4.78. Zeta potential and average particle size values obtained for different CO_2 percentage experiments during crystallization.

SEM images of the $CaCO_3$ particles produced with a 13% of CO_2 were shown in Figure 4.79. At the beginning of the crystallization, small rice-like particles from 100 to 450 nm were obtained. Then, the particle size distribution narrowed, however, the average particle size slightly increased. At the same time, the lengths of $CaCO_3$ particles were decreased. The cubical and hollow particles were produced under the size of 300 nm at about zero conductivity value. After zero conductivity, monodisperse and homogeneous cubical $CaCO_3$ crystals were produced under the size of 250 – 300 nm.

The comparison of SEM images obtained at the end of each CO_2 percentage experiment was shown in Figure 4.80. As shown in the figure, narrowed size distribution was obtained for 13% CO_2 experiment comparing to the crystals obtained for a 99.99% CO_2. Moreover, rhombohedral $CaCO_3$ crystals were obtained at 99.99% CO_2, while cubical $CaCO_3$ particles were produced at 13% CO_2. All $CaCO_3$ particles produced at the end of each CO_2 percentage experiment were calcite crystals as indicated from the XRD patterns as shown in Figure 4.81.
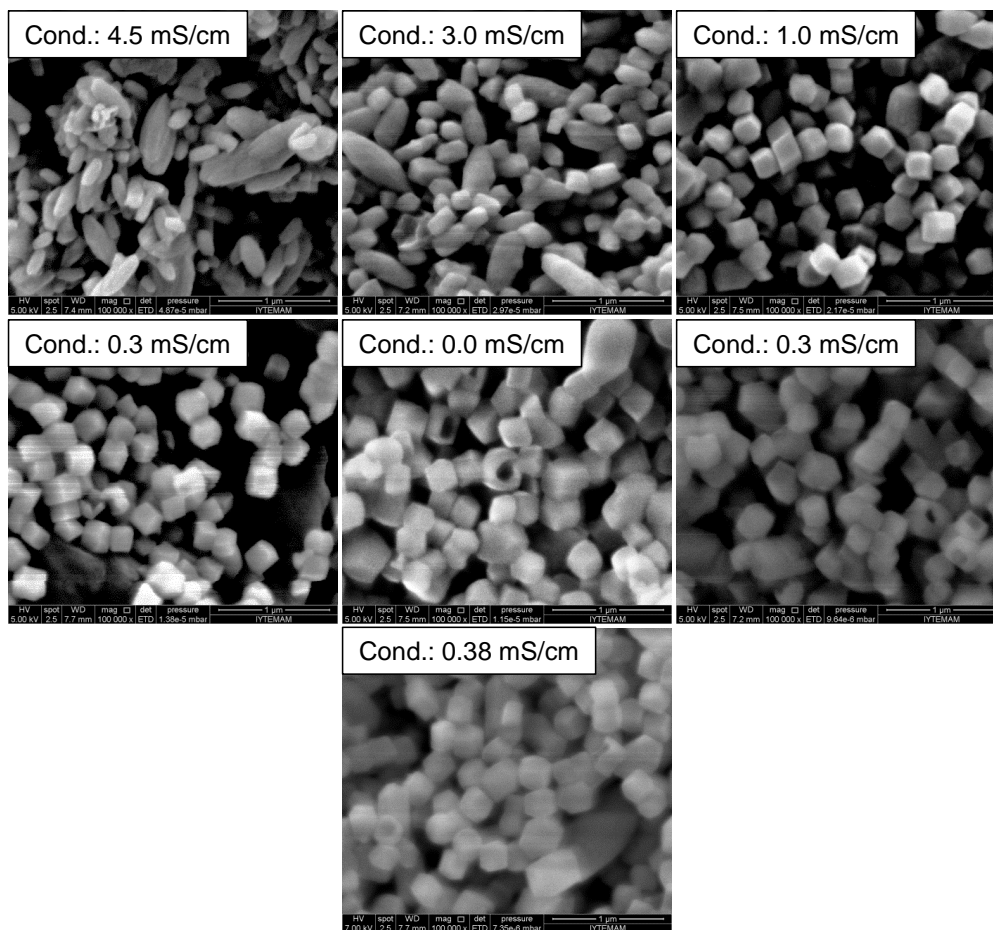
Figure 4.79. SEM images of the CaCO$_3$ particles obtained at lower CO$_2$ percentage of 13% (Scale: 1 μm).
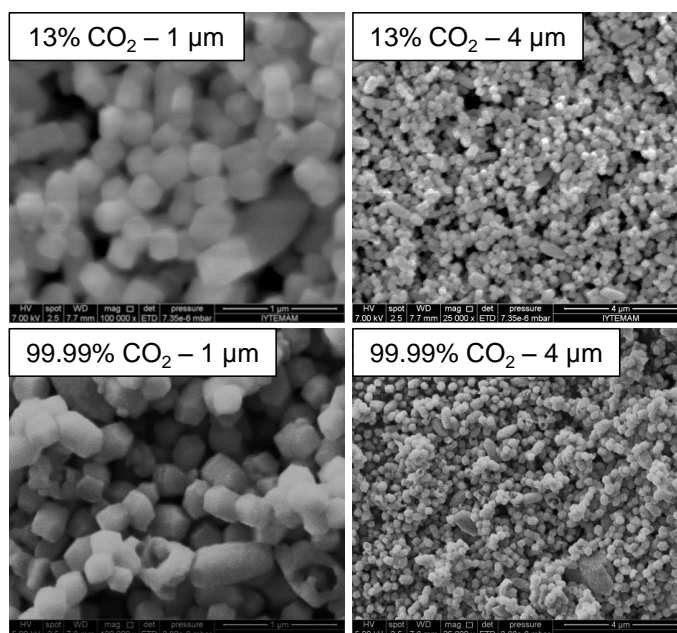
Figure 4.80. SEM images of the CaCO$_3$ obtained for different CO$_2$ percentage experiments at the end of the reaction (Scale: 1 μm).
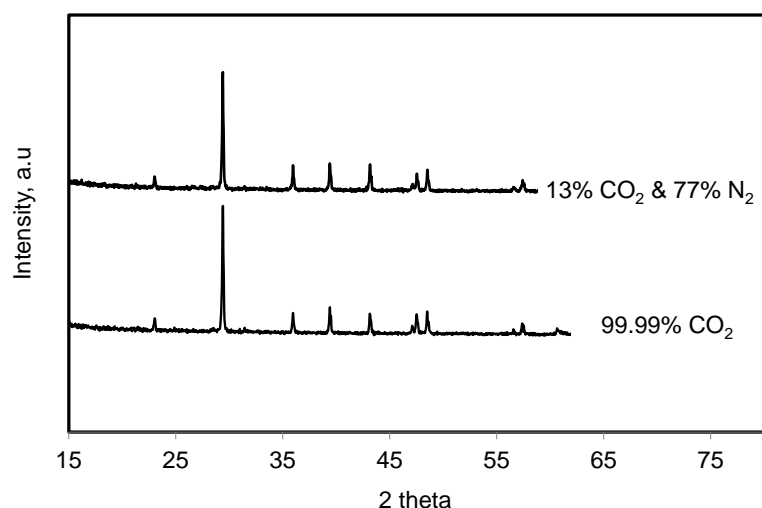
Figure 4.81. XRD patterns of crystals obtained for each CO_2 percentage.

4.4.9. Effect of Ca(OH)$_2$ Purity

The homogeneous and heterogeneous nucleation can be obtained during the CaCO$_3$ crystallization depending on the Ca(OH)$_2$ purity. In order to investigate the homogeneous and heterogeneous nucleation during CaCO$_3$ precipitation, Ca(OH)$_2$ purity experiment was performed in a 15 mM Ca(OH)$_2$ solution. Figure 4.82 shows pH, and conductivity values, and the calculated [OH$^-$] and [Ca^{++}] concentrations during CaCO$_3$ synthesis in the presence of both filtrated and unfiltrated Ca(OH)$_2$ solution. As shown in the figure, the consumption time for unfiltrated Ca(OH)$_2$ solution was shorter than that found for the filtrated Ca(OH)$_2$ solution.

Figure 4.83 shows the zeta potential obtained at different Ca(OH)$_2$ purity. As shown in the figure, the zeta potential obtained for unfiltered Ca(OH)$_2$ solution was higher than zeta potential obtained for filtrated Ca(OH)$_2$.
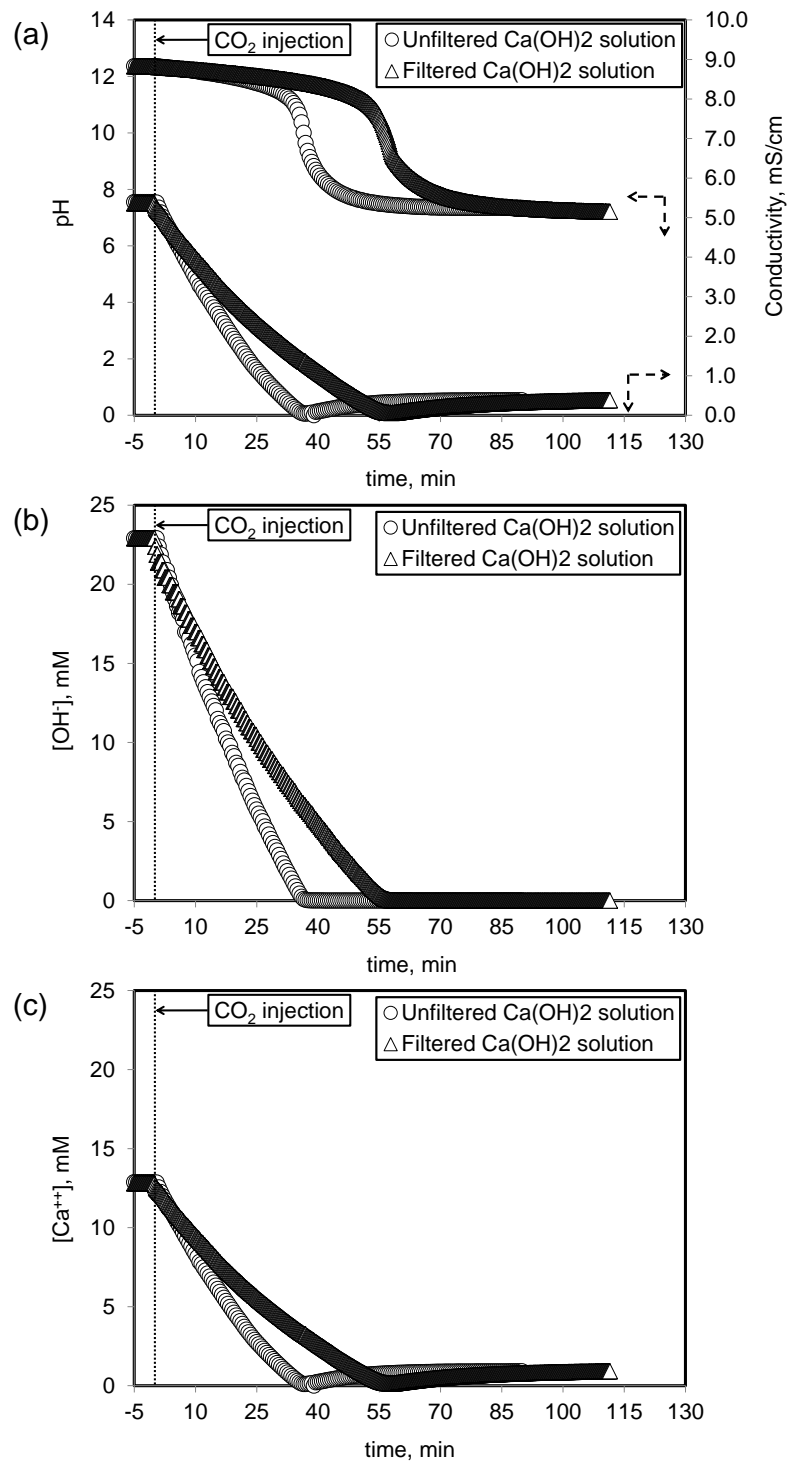
Figure 4.82. (a) pH and conductivity values and (b) calculated OH^- and (c) Ca^{++} concentrations for unfiltered and filtered $Ca(OH)_2$ solutions.
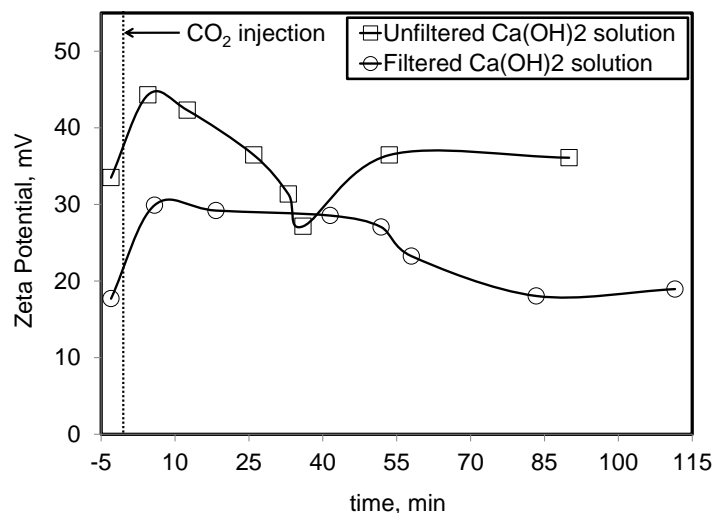
Figure 4.83. Change in the zeta potential and average $CaCO_3$ size in the presence of filtered and unfiltered $Ca(OH)_2$ solutions.

The SEM images of $CaCO_3$ crystals obtained from filtered and unfiltered $Ca(OH)_2$ solutions were shown in Figure 4.84. As shown in the figure, almost monodisperse rhombohedral $CaCO_3$ particles with average particle sizes of about 200 nm were obtained for the unfiltered $Ca(OH)_2$ by the heterogeneous nucleation. On the other hand, aggregated cubical $CaCO_3$ particles were obtained for the filtered $Ca(OH)_2$ solution in micron sizes by the homogeneous nucleation. As shown in the figure, aggregated crystals obtained by homogeneous nucleation could be related to the smaller zeta potential values of filtrated $Ca(OH)_2$ solution. In addition, average particle size for filtered $Ca(OH)_2$ solution could not be obtained since aggregated particle size were larger than 10 μm as shown in the figure. It was anticipated that the presence of impurities in the $Ca(OH)_2$ solution is favorable in nano calcite production. As shown in Figure 4.85, both $CaCO_3$ particles obtained for both filtered and unfiltered $Ca(OH)_2$ was calcite.
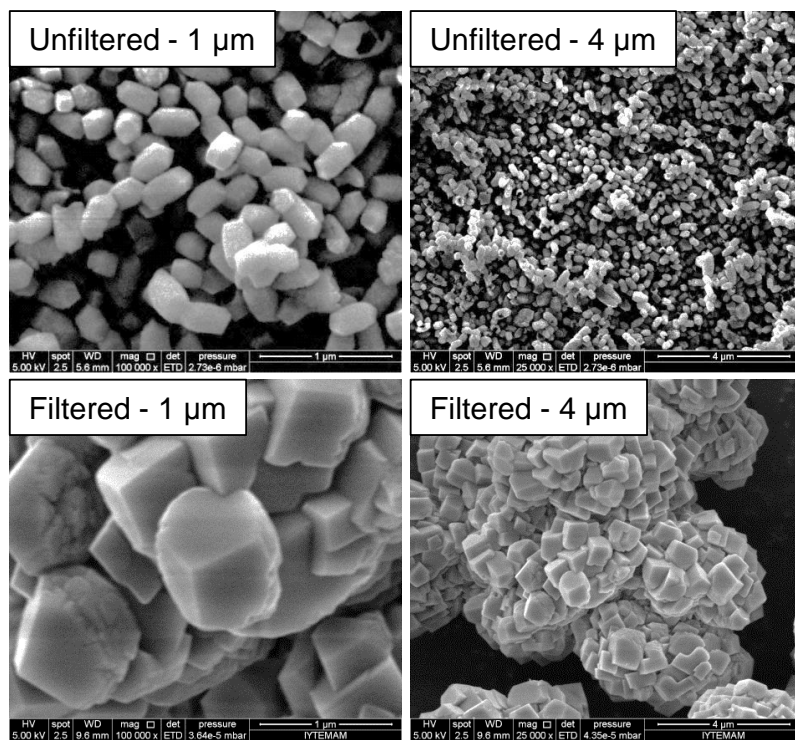
Figure 4.84. SEM images of the CaCO₃ crystals obtained for both filtered and unfiltered Ca(OH)₂ solution.
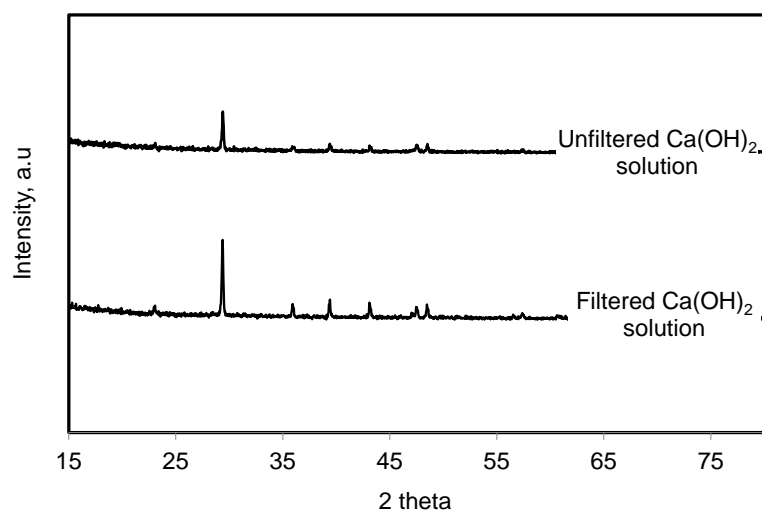
Figure 4.85. XRD patterns of precipitates obtained for unfiltered and filtered Ca(OH)₂.

CHAPTER 5

CONCLUSIONS

The dissolution rate of CO_2 was proposed as the limiting step in $CaCO_3$ crystallization. The adjustment of CO_2 dissolution within $Ca(OH)_2$ solution could be achieved by a newly developed small penetration method, for which the CO_2 could penetrate only to a certain depth in the flowing $Ca(OH)_2$ solution. Stability of $CaCO_3$ in $Ca(OH)_2$ was investigated. Zeta potential of 10 mM $CaCO_3$ was found to be negative value. Zeta potential of $CaCO_3$ particles was increased from -2 to 39 mV when $Ca(OH)_2$ was added in $CaCO_3$ slurry. This indicated that stability of $CaCO_3$ particles could be possible in $Ca(OH)_2$ solution. The average particle size obtained by the SEM images and the DLS technique were different due mainly to the settling of larger $CaCO_3$ particles. The measured conductivity values of $Ca(OH)_2$ with concentration were in good agreement with the literature. A linear relationship was found up to the saturation limit of $Ca(OH)_2$. However, the conductivity of $Ca(OH)_2$ solution was smaller than their theoretical values. The calculated OH^- ion concentration was lower than 2 times of the theoretical Ca^{++} ion concentration indicating that clustering of Ca^{++} and OH^- ions would occur in solution.

A new method called small penetration method was developed for the production of $CaCO_3$ in nano sizes, homogeneous size distribution, and different morphologies. It was found that the pH and conductivity values at the reaction chamber outlet was slightly smaller than those from the stabilization tank indicating that the penetration of CO_2 into $Ca(OH)_2$ solution could only be a small penetration depth rather than neutralizing the whole bulk liquid. Therefore, the CO_2 transfer rate could well be controlled by the small penetration method for the production of nano calcite. A possible mechanism for nano calcite production with the proposed small penetration method was determined. Rice-like $CaCO_3$ particles were obtained at the very early stages of crystallization. When $CaCO_3$ crystallization progressed, the high energetic end sites started to dissolve. Finally, rhombohedral calcite particles were produced. The dissolution was further progressed through the inside of the particles, and interestingly hollow calcite particles were synthesized. At the late stage of crystallization, hollow

particles were filled, and rhombohedral calcite particles were produced. At the early stage of the $CaCO_3$ crystallization, the surface area of $CaCO_3$ particles was found to be 11.26 m^2/g. Then, the specific surface area increased and reached to the highest value of 14.75 m^2/g due to hollow calcite production. At the late stage of crystallization, the surface area decreased due to filling of hollow calcite particles. A 88.04% of conversion was detected during crystallization up to near zero conductivity and stayed unchanged up to the end of crystallization. $CaCO_3$ particles at different morphologies could be produced by the CO_2 pulsation method. Rice-like particles were obtained at the beginning of crystallization and round shape almost hollow nano calcite particles were produced at the late stage of crystallization.

The effects of different parameters on $CaCO_3$ particles and morphologies were investigated in the developed small penetration method. The effect of stirring rate on the size and morphology of $CaCO_3$ particle was investigated. It was found that pH and conductivity values seemed to be the same for different stirring rate experiments. Therefore, repeatable and reproducible results were shown to be obtained in the newly developed small penetration method. The effect of $Ca(OH)_2$ flow rate on the size and morphology of $CaCO_3$ crystals was investigated. The CO_2 dissolution rate in liquid phase increased when maximum velocity of liquid phase was increased. Similar particles were produced but some aggregated particles were discerned at lower $Ca(OH)_2$ flow rates. The effect of CO_2 flow rate on $CaCO_3$ particle size and morphology was investigated. The consumption time of ions decreased significantly with increasing CO_2 injection rate into the reaction chamber. The average particle size was smaller at lower CO_2 flow rates. On the other hand, when CO_2 flow rate was increased, the particles were aggregated to form larger particles. The effect of $Ca(OH)_2$ concentrations on the size and morphology of $CaCO_3$ was investigated. At higher $Ca(OH)_2$ concentrations, two crystallization rates were seen. While the Ca^{++} and OH^- ions were consumed, the additional ions were supplied from the undissolved $Ca(OH)_2$ slurries. A U-type curve was obtained for average particle size for the different $Ca(OH)_2$ concentrations. The smallest average particle size could be obtained when the $Ca(OH)_2$ concentration was 15 mM, which was slightly below the solubility limit. Larger rhomboscalenohedral calcite particles were obtained below 15 mM of $Ca(OH)_2$ concentration, rhombohedral nano $CaCO_3$ particles were synthesized at 15 mM, and scalenohedral and rhombohedral $CaCO_3$ particles were produced at higher concentrations than the solubility limit, where the particles were larger and aggregated. The effect of tank volume on $CaCO_3$ size and

morphology was investigated. There were a linear relationship between the tank volume and the Ca^{++} and OH^- consumption rates. When the tank volume was larger, the more homogeneous and small crystal particles were obtained. The change in tank volumes did not affect the morphology, and rhombohedral calcite particles were synthesized for different tank volumes. The effect of pipe diameter was investigated. The particle size was smaller when the pipe diameter was smaller. The morphology of the particles did not change with the change in the pipe diameter. Rhombohedral calcite was produced for different pipe diameter experiments. The effect of contact length on the size and morphology of $CaCO_3$ was investigated. The particle size was slightly smaller when the contact length was shorter. CO_2 dissolution rate increased with increasing contact length. The effect of CO_2 percentage on $CaCO_3$ size and morphology was also investigated. The dissolution rate of CO_2 is decreased when the percentages of CO_2 was lower. The average particle size was smaller for lower CO_2 percentage. Rhombohedral $CaCO_3$ crystals were synthesized at 99.99% CO_2. On the other hand, cubical $CaCO_3$ particles were obtained at 13% CO_2. The effect of $Ca(OH)_2$ purity on the size and morphology was investigated. Monodisperse rhombohedral $CaCO_3$ particles were produced for the unfiltered $Ca(OH)_2$ by the heterogeneous nucleation, and aggregated cubical $CaCO_3$ particles were obtained in micron sizes for the filtered $Ca(OH)_2$ solution by the homogeneous nucleation.

All in all, a new method called small penetration method was developed and production of hollow nano calcite particles in homogeneous size distribution was achieved.

REFERENCES

Bartczak, Z., Argon, A. S., Cohen, R. E., & Kowalewski, T. (1999). The morphology and orientation of polyethylene in films of sub-micron thickness crystallized in contact with calcite and rubber substrates. *Polymer, 40*(9), 2367-2380.

Bolze, J., Peng, B., Dingenouts, N., Panine, P., Narayanan, T., & Ballauff, M. (2002). Formation and growth of amorphous colloidal CaCO3 precursor particles as detected by time-resolved SAXS. *Langmuir, 18*(22), 8364-8369. doi: 10.1021/la025918d

Burns, J. R., & Jachuck, J. J. (2005). Monitoring of CaCO3 production on a spinning disc reactor using conductivity measurements. *Aiche Journal, 51*(5), 1497-1507.

Campos, J. S. D., Ribeiro, A. A., & Cardoso, C. X. (2007). Preparation and characterization of PVDF/CaCO3 composites. *Materials Science and Engineering B-Solid State Materials for Advanced Technology, 136*(2-3), 123-128. doi: DOI 10.1016/j.mseb.2006.09.017

Carmona, J. G., Morales, J. G., & Clemente, R. R. (2003a). Rhombohedral-scalenohedral calcite transition produced by adjusting the solution electrical conductivity in the system Ca(OH)2-CO2-H2O. *J Colloid Interface Sci, 261*(2), 434-440. doi: 10.1016/S0021-9797(03)00149-8

Carmona, J. G., Morales, J. G., & Clemente, R. R. (2003b). Morphological control of precipitated calcite obtained by adjusting the electrical conductivity in the Ca(OH)(2)-H2O-CO2 system. *Journal of crystal growth, 249*(3-4), 561-571. doi: Doi 10.1016/S0022-0248(02)02173-5

Carmona, J. G., Morales, J. G., Sainz, J. F., & Clemente, R. R. (2003c). Morphological characteristics and aggregation of calcite crystals obtained by bubbling CO2 through a Ca(OH)2 suspension in the presence of additives. *Powder technology, 130*(1-3), 307-315.

Carmona, J. G., Morales, J. G., Sainz, J. F., Loste, E., & Clemente, R. R. (2004). The mechanism of precipitation of chain-like calcite. *Journal of crystal growth, 262*(1-4), 479-489. doi: DOI 10.1016/j.jcrysgro.2003.10.003

Chan, C.M., Wu, J., Li, J.X., & Cheung, Y.K. (2002). Polypropylene/calcium carbonate nanocomposites. *Polymer, 43*(10), 2981-2992.

Chen, GG, Luo, GS, Xu, JH, & Wang, JD. (2004). Membrane dispersion precipitation method to prepare nanopartials. *Powder technology, 139*(2), 180-185.

Chen, J. F., Wang, Y. H., Guo, F., Wang, X. M., & Zheng, C. (2000). Synthesis of nanoparticles with novel technology: High-gravity reactive precipitation. *Industrial & engineering chemistry research, 39*(4), 948-954.

Cheng, B., Lei, M., Yu, J., & Zhao, X. (2004). Preparation of monodispersed cubic calcium carbonate particles via precipitation reaction. *Materials Letters, 58*(10), 1565-1570.

Chibowski, E, Hotysz, L, & Szcześ, A. (2003a). Time dependent changes in zeta potential of freshly precipitated calcium carbonate. *Colloids and Surfaces A: Physicochemical and Engineering Aspects, 222*(1), 41-54.

Chibowski, E., Hołysz, L., Szcześ, A., & Chibowski, M. (2003b). Precipitation of calcium carbonate from magnetically treated sodium carbonate solution. *Colloids and Surfaces A: Physicochemical and Engineering Aspects, 225*(1), 63-73.

Cölfen, H. (2003). Precipitation of carbonates: recent progress in controlled production of complex shapes. *Current opinion in colloid & interface science, 8*(1), 23-31.

Cölfen, H., & Qi, L. (2001). A Systematic Examination of the Morphogenesis of Calcium Carbonate in the Presence of a Double-Hydrophilic Block Copolymer. *Chemistry-A European Journal, 7*(1), 106-116.

Dalas, E., & Koutsoukos, P.G. (1990). Calcium carbonate scale formation and prevention in a flow-through system at various temperatures. *Desalination, 78*(3), 403-416.

Dickinson, S. R., & McGrath, K. M. (2004). Aqueous precipitation of calcium carbonate modified by hydroxyl-containing compounds. *Crystal Growth & Design, 4*(6), 1411-1418. doi: Doi 10.1021/Cg049843i

Domingo, C., Loste, E., Gómez-Morales, J., García-Carmona, J., & Fraile, J. (2006). Calcite precipitation by a high-pressure CO2 carbonation route. *The Journal of supercritical fluids, 36*(3), 202-215. doi: 10.1016/j.supflu.2005.06.006

Fenter, P., Geissbuhler, P., DiMasi, E., Srajer, G., Sorensen, L. B., & Sturchio, N. C. (2000). Surface speciation of calcite observed in situ by high-resolution X-ray reflectivity. *Geochimica et Cosmochimica Acta, 64*(7), 1221-1228.

Ford, IJ. (2004). Statistical mechanics of nucleation: a review. *Proceedings of the Institution of Mechanical Engineers, Part C: Journal of Mechanical Engineering Science, 218*(8), 883-899.

Fu, S. Y., Feng, X. Q., Lauke, B., & Mai, Y. W. (2008). Effects of particle size, particle/matrix interface adhesion and particle loading on mechanical properties of particulate-polymer composites. *Composites Part B-Engineering, 39*(6), 933-961. doi: DOI 10.1016/j.compositesb.2008.01.002

Gebauer, D., Volkel, A., & Colfen, H. (2008). Stable prenucleation calcium carbonate clusters. *Science, 322*(5909), 1819-1822. doi: 10.1126/science.1164271

Giannimaras, E.K., & Koutsoukos, P.G. (1987). The crystallization of calcite in the presence of orthophosphate. *Journal of colloid and interface science, 116*(2), 423-430.

Gomez-Morales, J., Torrent-Burgues, J., & Rodriguez-Clemente, R. (1996). Nucleation of calcium carbonate at different initial pH conditions. *Journal of crystal growth, 169*(2), 331-338.

Gunasekaran, S., & Anbalagan, G. (2008). Spectroscopic study of phase transitions in natural calcite mineral. *Spectrochimica Acta Part a-Molecular and Biomolecular Spectroscopy, 69*(4), 1246-1251. doi: DOI 10.1016/j.saa.2007.06.036

Guo, H., Yu, J. G., & Cheng, B. (2006). Preparation and formation mechanism of wood-block-like calcite particles. *Journal of Solid State Chemistry, 179*(8), 2547-2553. doi: DOI 10.1016/j.jssc.2006.05.005

Han, Y. S., Hadiko, G., Fuji, M., & Takahashi, M. (2006a). Factors affecting the phase and morphology of CaCO3 prepared by a bubbling method. *Journal of the European Ceramic Society, 26*(4-5), 843-847. doi: 10.1016/j.jeurceramsoc.2005.07.050

Han, Y.S., Hadiko, G., Fuji, M., & Takahashi, M. (2006b). Influence of initial CaCl 2 concentration on the phase and morphology of CaCO 3 prepared by carbonation. *Journal of materials science, 41*(14), 4663-4667.

Hari, Bala, Ding, Xuefeng, Guo, Yiming, Deng, Yanhui, Wang, Chengyu, Li, Minggang, & Wang, Zichen. (2006). Multigram scale synthesis and characterization of monodispersed cubic calcium carbonate nanoparticles. *Materials Letters, 60*(12), 1515-1518. doi: DOI: 10.1016/j.matlet.2005.11.062

Hu, L., Dong, P., & Zhen, G. (2009). Preparation of active CaCO3 nanoparticles and mechanical properties of the composite materials. *Materials Letters, 63*(3-4), 373-375.

Isopescu, R, Mocioi, M, Zahanagiu, F, & Filipescu, L. (1996). Growth rate models and kinetics estimation for CaCO3 precipitated in continuous crystallizers. *Journal of crystal growth, 167*(1), 260-264.

Jung, W. M., Kang, S. H., Kim, W. S., & Choi, C. K. (2000). Particle morphology of calcium carbonate precipitated by gas-liquid reaction in a Couette-Taylor reactor. *Chemical engineering science, 55*(4), 733-747.

Juvekar, V. A., & Sharma, M. M. (1973). Absorption of Co2 in a Suspension of Lime. *Chemical Engineering Science, 28*(3), 825-837.

Kabasci, S., Althaus, W., & Weinspach, PM. (1996). Batch-Precipitation of Calcium-Carbonate from Highly Supersaturated Solutions. *Chemical engineering research & design, 74*(7), 765-772.

Kashchiev, D, & Van Rosmalen, GM. (2003). Review: Nucleation in solutions revisited. *Crystal Research and Technology, 38*(7-8), 555-574.

Kiss, A., Fekete, E., & Pukanszky, B. (2007). Aggregation of CaCO3 particles in PP composites: Effect of surface coating. *Composites science and technology, 67*(7-8), 1574-1583. doi: DOI 10.1016/j.compscitech.2006.07.010

Kitamura, M., Konno, H., Yasui, A., & Masuoka, H. (2002). Controlling factors and mechanism of reactive crystallization of calcium carbonate polymorphs from calcium hydroxide suspensions. *Journal of crystal growth, 236*(1), 323-332.

Kitamura, M., & Yasui, A. (2000). Crystallization behavior of calcium carbonate polymorphs and the effect of magnesium ion. *8th World Salt Symposium, Vols 1 and 2*, 1191-1192.

Konno, H., Nanri, Y., & Kitamura, M. (2003). Effect of NaOH on aragonite precipitation in batch and continuous crystallization in causticizing reaction. *Powder technology, 129*(1-3), 15-21.

Kralj, D., Brečević, L., & Kontrec, J. (1997). Vaterite growth and dissolution in aqueous solution III. Kinetics of transformation. *Journal of crystal growth, 177*(3), 248-257.

Lam, T. D., Hoang, T. V., Quang, D. T., & Kim, J. S. (2009). Effect of nanosized and surface-modified precipitated calcium carbonate on properties of CaCO3/polypropylene nanocomposites. *Materials Science and Engineering a-Structural Materials Properties Microstructure and Processing, 501*(1-2), 87-93. doi: DOI 10.1016/j.msea.2008.09.060

Lerner, E., Azoury, R., & Sarig, S. (1989). Rapid precipitation of apatite from ethanol-water solution. *Journal of crystal growth, 97*(3), 725-730.

Liang, JZ. (2007). Evaluation of dispersion of nano-CaCO3 particles in polypropylene matrix based on fractal method. *Composites Part A: Applied Science and Manufacturing, 38*(6), 1502-1506.

Lin, Y., Chen, H., Chan, C.M., & Wu, J. (2008). High impact toughness polypropylene/CaCO3 nanocomposites and the toughening mechanism. *Macromolecules, 41*(23), 9204-9213.

Liu, X. B., Zou, Y. B., Cao, G. P., & Luo, D. W. (2007). The preparation and properties of biodegradable polyesteramide composites reinforced with nano-CaCO3 and nano-SiO2. *Materials Letters, 61*(19-20), 4216-4221. doi: DOI 10.1016/j.matlet.2007.01.065

Lopez-Macipe, A., Gomez-Morales, J., & Rodriguez-Clemente, R. (1996). Calcium carbonate precipitation from aqueous solutions containing Aerosol OT. *Journal of crystal growth, 166*(1), 1015-1019.

Lopez, O., Zuddas, P., & Faivre, D. (2009). The influence of temperature and seawater composition on calcite crystal growth mechanisms and kinetics: Implications for Mg incorporation in calcite lattice. *Geochimica et Cosmochimica Acta, 73*(2), 337-347.

Mann, S. (1988). Molecular recognition in biomineralization. *Nature, 332*(6160), 119-124.

Matahwa, H., Ramiah, V., & Sanderson, R. D. (2008). Calcium carbonate crystallization in the presence of modified polysaccharides and linear polymeric additives. *Journal of Crystal Growth, 310*(21), 4561-4569. doi: DOI 10.1016/j.jcrysgro.2008.07.089

Mathur, V.K. (2001). High speed manufacturing process for precipitated calcium carbonate employing sequential perssure carbonation: Google Patents.

Merris, C. (1998). *Innovative advances in the forest products industries.* Paper presented at the AIChE Symposium Series.

Molva, M. (2011). Production of Nano CaCO3 by Carbonization Route. *Master of Science thesis, İzmir Institude of Technology*.

Montes-Hernandez, G., Fernández-Martínez, A., Charlet, L., Tisserand, D., & Renard, F. (2008). Textural properties of synthetic nano-calcite produced by hydrothermal carbonation of calcium hydroxide. *Journal of Crystal Growth, 310*(11), 2946-2953. doi: DOI: 10.1016/j.jcrysgro.2008.02.012

Nebel, H., Neumann, M., Mayer, C., & Epple, M. (2008). On the structure of amorphous calcium carbonate - A detailed study by solid-state NMR spectroscopy. *Inorganic Chemistry, 47*(17), 7874-7879. doi: Doi 10.1021/Ic8007409

Nehrke, G., Reichart, G. J., Van Cappellen, P., Meile, C., & Bijma, J. (2007). Dependence of calcite growth rate and Sr partitioning on solution stoichiometry: Non-Kossel crystal growth. *Geochimica et Cosmochimica Acta, 71*(9), 2240-2249. doi: DOI 10.1016/j.gca.2007.02.002

Ogino, T., Suzuki, T., & Sawada, K. (1987). The formation and transformation mechanism of calcium carbonate in water. *Geochimica et Cosmochimica Acta, 51*(10), 2757-2767.

Ogino, T., Suzuki, T., & Sawada, K. (1990). The rate and mechanism of polymorphic transformation of calcium carbonate in water. *Journal of crystal growth, 100*(1), 159-167.

Osman, M.A., Atallah, A., & Suter, U.W. (2004). Influence of excessive filler coating on the tensile properties of LDPE–calcium carbonate composites. *Polymer, 45*(4), 1177-1183.

Perić, J., Vučak, M., & Krstulović, R. (1995). Precipitation of calcium carbonate by carbon dioxide method. *Adv. Sci. Technol. , 3B*, 1245.

Perry, RH, Green, DW, & Maloney, JO. (1984). Perry's chemical engineers' handbook, 6th editionMcGraw-Hill. *New York*.

Pontoni, D., Bolze, J., Dingenouts, N., Narayanan, T., & Ballauff, M. (2003). Crystallization of calcium carbonate observed in-situ by combined small-and wide-angle X-ray scattering. *The Journal of Physical Chemistry B, 107*(22), 5123-5125.

Pouget, E. M., Bomans, P. H., Goos, J. A., Frederik, P. M., de With, G., & Sommerdijk, N. A. (2009). The initial stages of template-controlled CaCO3 formation revealed by cryo-TEM. *Science, 323*(5920), 1455-1458. doi: 10.1126/science.1169434

Pukanszky, B., & Fekete, E. (1998). Aggregation tendency of particulate fillers: Determination and consequences. *Polymers & Polymer Composites, 6*(5), 313-322.

Rieger, J., Thieme, J., & Schmidt, C. (2000). Study of precipitation reactions by X-ray microscopy: CaCO3 precipitation and the effect of polycarboxylates. *Langmuir, 16*(22), 8300-8305.

Rodriguez-Clemente, R., & Gomez-Morales, J. (1996). Microwave precipitation of CaCO3 from homogeneous solutions. *Journal of crystal growth, 169*(2), 339-346.

Roskill Information Services, Ltd. (2008). The Economics of Ground Calcium Carbonate. *Global Information, 3rd edition*.

Sahebian, S., Zebarjad, S. M., Khaki, J. V., & Sajjadi, S. A. (2009). The effect of nano-sized calcium carbonate on thermodynamic parameters of HDPE. *Journal of Materials Processing Technology, 209*(3), 1310-1317. doi: DOI 10.1016/j.jmatprotec.2008.03.066

Sant'Anna, S. S. E., de Souza, D. A., de Araujo, D. M., Carvalho, C. D., & Yoshida, M. I. (2008). Physico-chemical Analysis of Flexible Polyurethane Foams Containing Commercial Calcium Carbonate. *Materials Research-Ibero-American Journal of Materials, 11*(4), 433-438.

Sheng, Y., Zhao, J. Z., Zhou, B., Ding, X. F., Deng, Y. H., & Wang, Z. C. (2006a). In situ preparation of CaCO3/polystyrene composite nanoparticles. *Materials Letters, 60*(27), 3248-3250. doi: DOI 10.1016/j.matlet.2006.02.090

Silva, R., Pereira, G. M., Muniz, E. C., & Rubira, A. F. (2009). Calcium Carbonate Crystallization on a Polyethylene Surface Containing Ultrathin Layers of Hydrophilic Polymers. *Crystal Growth & Design, 9*(7), 3307-3312. doi: Doi 10.1021/Cg900106s

Sondi, Ivan, Škapin, Srečo D., & Salopek-Sondi, Branka. (2008). Biomimetic Precipitation of Nanostructured Colloidal Calcite Particles by Enzyme-Catalyzed Reaction in the Presence of Magnesium Ions. *Crystal Growth & Design, 8*(2), 435-441. doi: 10.1021/cg070195n

Song, Y. H., Chu, G. W., M., Chen J., & Chen, J. F. (2003). Research progress on mass transfer and reaction equipments. *Chemical Industry and Engineering Progress (in Chinese), 22*(8), 841-844.

Spanos, N., & Koutsoukos, P. G. (1998). Kinetics of precipitation of calcium carbonate in alkaline pH at constant supersaturation. Spontaneous and seeded growth. *Journal of Physical Chemistry B, 102*(34), 6679-6684.

Stepkowska, E.T., Perez-Rodriguez, JL, Sayagues, MJ, & Martinez-Blanes, JM. (2003). Calcite, vaterite and aragonite forming on cement hydration from liquid and gaseous phase. *Journal of thermal analysis and calorimetry, 73*(1), 247-269.

Tang, C. Y., & Liang, J. Z. (2003). A study of the melt flow behaviour of ABS/CaCO3 composites. *Journal of materials processing technology, 138*(1-3), 408-410. doi: Doi 10.1016/S0924-0136(03)00108-0

Uebo, K., Yamazaki, R., & Yoshida, K. (1992). Precipitation mechanism of calcium carbonate fine particles in a three-phase reactor. *Advanced Powder Technology, 3*(1), 71-79.

Ukrainczyk, M., Kontrec, J., Babic-Ivancic, V., Brecevic, L., & Kralj, D. (2007). Experimental design approach to calcium carbonate precipitation in a semicontinuous process. *Powder Technology, 171*(3), 192-199. doi: DOI 10.1016/j.powtec.2006.10.046

Ukrainczyk, M., Kontrec, J., & Kralj, D. (2009). Precipitation of different calcite crystal morphologies in the presence of sodium stearate. *J Colloid Interface Sci, 329*(1), 89-96. doi: 10.1016/j.jcis.2008.09.045

Uyanık, T. (2010). Mining Industry in Turkey. *Export Promotion Center of Turkey*.

Van Cappellen, Philippe, Charlet, Laurent, Stumm, Werner, & Wersin, Paul. (1993). A surface complexation model of the carbonate mineral-aqueous solution interface. *Geochimica et Cosmochimica Acta, 57*(15), 3505-3518.

Vucak, M., Peric, J., Zmikic, A., & Pons, M. N. (2002). A study of carbon dioxide absorption into aqueous monoethanolamine solution containing calcium nitrate in the gas-liquid reactive precipitation of calcium carbonate. *Chemical Engineering Journal, 87*(2), 171-179.

Wang, C. Y., Xiao, P., Zhao, J. Z., Zhao, X., Liu, Y. H., & Wang, Z. C. (2006). Biomimetic synthesis of hydrophobic calcium carbonate nanoparticles via a carbonation route. *Powder Technology, 170*(1), 31-35. doi: DOI 10.1016/j.powtec.2006.08.016

Wang, J., Kenner, T. C., Li, G., & Khang, S. J. (1998). The dissolution rate of Ca(OH)2 in aqueous solutions. *Chemical Engineering Communications, 169*, 167-184.

Wang, K., Wang, Y. J., Chen, G. G., Luo, G. S., & Wang, J. D. (2007). Enhancement of mixing and mass transfer performance with a microstructure minireactor for controllable preparation of CaCO3 nanoparticles. *Industrial & Engineering Chemistry Research, 46*(19), 6092-6098. doi: Doi 10.1021/Ie061502+

Windholz, M., Budavari, S., Stroumtsos, L.Y., & Fretig, M.N. (1976). The Merck Index, 9th Edition. 212.

Wray, J.L., & Daniels, F. (1957). Precipitation of calcite and aragonite. *Journal of the american chemical society, 79*(9), 2031-2034.

Wu, G. H., Wang, Y. J., Zhu, S. L., & Wang, J. D. (2007). Preparation of ultrafine calcium carbonate particles with micropore dispersion method. *Powder technology, 172*(2), 82-88. doi: DOI 10.1016/j.powtec.2006.10.031

Xu, A. W., Ma, Y. R., & Colfen, H. (2007). Biomimetic mineralization. *Journal of Materials Chemistry, 17*(5), 415-449. doi: Doi 10.1039/B611918m

Zebarjad, S. M., & Sajjadi, S. A. (2008). On the strain rate sensitivity of HDPE/CaCO3 nanocomposites. *Materials Science and Engineering a-Structural Materials Properties Microstructure and Processing, 475*(1-2), 365-367. doi: DOI 10.1016/j.msea.2007.05.008